The Philosophical Magazine

FIRST PUBLISHED IN 1798

A Journal of Theoretical Experimental and Applied Physics

Vol. 3 March 1958 No. 27
Eighth Series

£1 5s. 0d., plus postage
Annual Subscription £13 10s. 0d., payable in advance

Printed and Published by
TAYLOR & FRANCIS LTD
RED LION COURT, FLEET STREET, LONDON, E.C.4

THE PHILOSOPHICAL MAGAZINE

Authors wishing to submit papers for publication in the Journal should send manuscripts directly to the Publishers.

Manuscripts should be typed in *double* spacing on one side of quarto (8×10 in.) paper, and authors are urged to aim at absolute clarity of meaning and an attractive presentation of their texts.

References should be listed at the end in alphabetical order of authors and should be cited in the text in terms of author's name and date. Diagrams should normally be in Indian ink on white card, with lettering in soft pencil, the captions being typed on a separate sheet.

A leaflet giving detailed instructions to authors on the preparation of papers is available on request from the Publishers.

Authors are entitled to receive 25 offprints of a paper in the Journal free of charge, and additional offprints can be obtained from the Publishers.

The *Philosophical Magazine* and its companion journal, *Advances in Physics*, will accept papers for publication in experimental and theoretical physics. The *Philosophical Magazine* publishes contributions describing new results, letters to the editor and book reviews. *Advances in Physics* publishes articles surveying the present state of knowledge in any branch of the science in which recent progress has been made. The editors welcome contributions from overseas as well as from the United Kingdom, and papers may be published in English, French and German.

The Theory of Small Angle Scattering from Dislocations†

By H. H. Atkinson and P. B. Hirsch
Crystallographic Laboratory, Cavendish Laboratory, Cambridge, England

[Received December 5, 1957]

Abstract

The small angle scattering of x-rays or neutrons from crystals containing a random network of dislocations is calculated. Three causes of density changes associated with dislocations are considered: that due to the elastic strain field from edge dislocations, that due to second-order elasticity effects and that due to the dislocation cores. It is found that in the range of angles for which experimental evidence is available, the effect due to the elastic strain field from edge dislocations predominates. The magnitude of the scattering expected from the theory for a dislocation density of about 10^{11} cm^{-2} is of the same order as that found recently from small angle neutron scattering experiments on heavily cold-worked copper.

§ 1. Introduction

Since the original x-ray experiments of Blin and Guinier (1951, 1953), Blin (1954, 1955) and Hayes and Smoluchowski (1954), small angle scattering from cold-worked metals has been a subject of considerable interest. This scattering has been interpreted variously as being due to small holes (Blin and Guinier 1951), due to non-linear distortions caused by dislocations (Seeger 1957) or due to the linear elastic strain field around edge dislocations (Blin 1957). On the other hand an earlier calculation by Dexter (1953) shows that the intensity resulting from this last effect is much smaller than that observed.

However, recent small angle scattering experiments with x-rays (Beeman *et al.* 1957) and neutrons (Atkinson and Lowde 1957), and neutron transmission experiments (Weiss *et al.* 1952) have shown that the magnitude of the true small angle scattering due to density changes in the cold-worked crystals is much less than that reported by Blin and Guinier. The large intensities reported in the original work are now thought to be due to a double Bragg-scattering mechanism (Beeman *et al.*) and to surface effects (Robinson and Smoluchowski 1956, Zhurkov and Slutsker 1957). Some recent small angle scattering experiments with long wavelength neutrons (reported in a preliminary communication by Atkinson and Lowde 1957), which have indicated the order of magnitude of the true small angle scattering, will form the subject of another paper. The purpose of the present paper is to investigate theoretically and to

† Communicated by the Authors.

compare the importance of the different mechanisms for small angle scattering from a random assembly of dislocations. In the case of a polycrystalline material the results are calculated explicitly for direct comparison with experiment.

§ 2. Density Changes due to Dislocations

True small angle scattering of x-rays or neutrons is due to variations in the density of electrons or of nuclei respectively, extending over several atomic dimensions. Dislocations give rise to density changes

Fig. 1

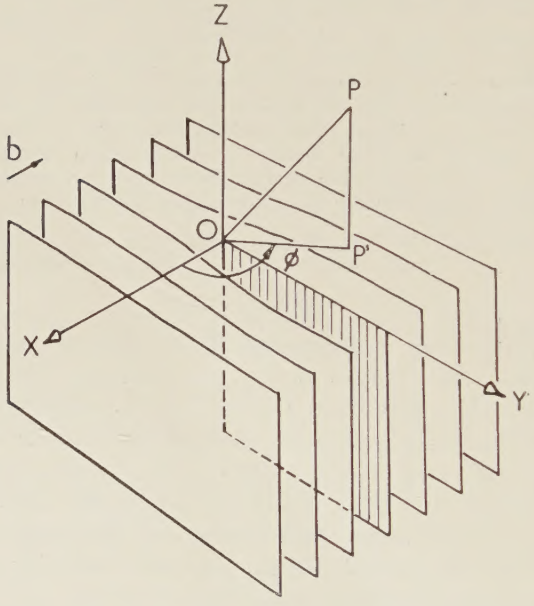

An edge dislocation in a simple cubic lattice. The dislocation core lies along the z-axis. The extra half plane of atoms is indicated by shading. The x-axis is parallel to the Burgers vector **b**. P is any point in the crystal and P' is its projection on to the plane XOY. It is clear that there is an increase of density for points with y positive and a decrease for y negative. The slip plane is XOZ.

of this type. There are three ways in which dislocations cause changes in density:

(*a*) The elastic stress field of an edge dislocation (of finite length $2H$) in an infinite isotropic medium gives rise to a dilatation $\Delta(=dV/V)$ given by Blin (1957)

$$\Delta=-\frac{b}{2\pi}\left(\frac{1-2\nu}{1-\nu}\right)\frac{\sin\phi}{r}\frac{1}{2}(\cos\alpha_1-\cos\alpha_2) \quad . \quad . \quad . \quad (1)$$

where r, ϕ, α_1 and α_2 are defined in figs. 1 and 2, b is the magnitude of the Burgers vector and ν is Poisson's ratio. This equation shows that a dislocation of finite length behaves rather like a dipole, so that little dilatation results at distances much greater than $2H$ from the dislocation line. For points close to the dislocation line the equation reduces to the more familiar form

$$\Delta = -\frac{b}{2\pi}\left(\frac{1-2\nu}{1-\nu}\right)\frac{\sin\phi}{r} \equiv F\frac{\sin\phi}{r} \quad . \quad . \quad . \quad . \quad (2)$$

where values of F are given in table 1.

Fig. 2

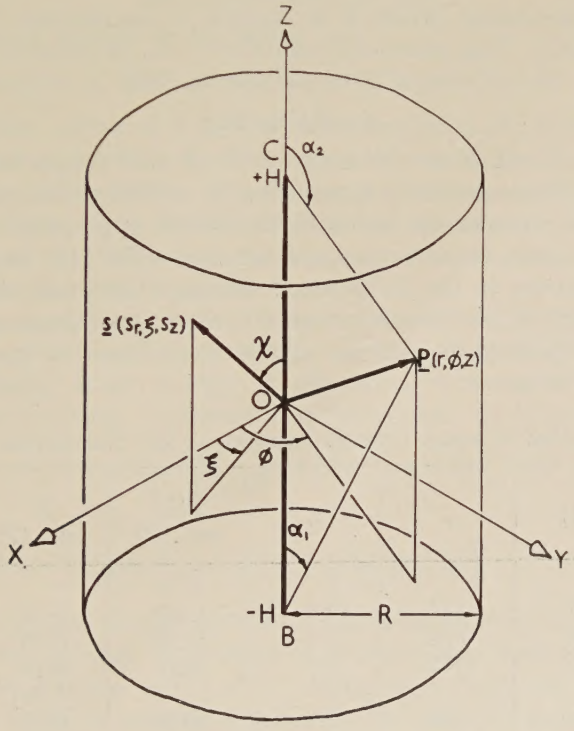

The straight dislocation line BC, of length $2H$, lies on the axis of a cylindrical crystal of height $2H$ and radius R. P is any point in the crystal and **s** is the reciprocal space vector. The x-axis is in the direction of the Burgers vector **b**.

For a random array of dislocations, independent arguments given later suggest that appreciable dilatation occurs only within a cylindrical region about the dislocation line, of length and diameter $2H$. Within this region eqn. (2) applies with sufficient accuracy. (Similar approximations have been made in the calculations of the second-order elastic effects given later.) A model of this type was used by Dexter (1953) in his calculation of small angle scattering. Blin has also calculated the scattering from this effect, assuming that the dislocation lines are

randomly distributed and that their length is either about 10^6 Å (1954) or about 3000 Å (1957). In the latter case it was further assumed that the dislocations are all parallel to certain directions in the crystal. Some aspects of Blin's results will be discussed in §§ 4 and 7.

For screw dislocations the elastic stress field contains only shear components and the dilatation is therefore zero.

(*b*) Second-order elastic effects associated with dislocations of any type give rise to small decreases in density. This effect was first proposed by Stehle and Seeger (1956) who calculated the dilatation analytically to be

$$\Delta = Kb^2/4\pi^2 r^2 \quad . \quad . \quad . \quad . \quad . \quad . \quad . \quad (3)$$

for a screw dislocation, where K is thought to lie between 0·6 and 1 for the noble metals. This relation is valid for $r > R_0$, the effective core radius, within which the dilatation is considered uniform and equal to

$$\Delta = Kb^2/4\pi^2 R_0^2. \quad . \quad . \quad . \quad . \quad . \quad . \quad . \quad (4)$$

R_0 is uncertain and of the order of b ; Stehle and Seeger favour $R_0 = \frac{1}{3}b$. Seeger (1957) has used these dilatations to calculate the scattering from isolated screw dislocations, but his calculations apply only at zero angle for single dislocations or in the special case when the reciprocal space vector **s** is normal to the dislocation. Seeger (1956) has also calculated the scattering, under the same special conditions, from a dissociated dislocation. As they stand these calculations cannot be applied directly to the experiments.

Table 1. Values of some Constants used in the Numerical Calculations

Metal	b(Å)	ν	γ	F(Å) eqn. (2)	K eqn. (7)	D(Å^2) eqn. (6)
Al	2·86	0·34	2·2	0·22	0·79	0·16
Fe	2·48	0·29	1·6	0·23	0·78	0·12
Ni	2·49	0·32	1·9	0·21	0·78 (1·09)	0·12
Cu	2·56	0·35	2·0	0·19	0·67 (0·63)	0·11
Pb	3·50	0·44	2·7	0·12	0·34	0·10

Lomer (1957) has pointed out that the density change due to the inelastic effect of dislocations can be calculated very simply in terms of the elastic energy, using Grüneisen's relation between thermal energy content and volume expansion. He obtains the relation

$$\Delta = 2\gamma\kappa w \quad . \quad . \quad . \quad . \quad . \quad . \quad . \quad . \quad (5)$$

where γ is Grüneisen's constant, κ is the compressibility and w is the elastic energy per unit volume. This expression is in agreement with that due to Stehle and Seeger in that Δ is proportional to the elastic strain

energy ; further, as Lomer has shown, the proportionality constant is nearly the same as that obtained by Stehle and Seeger. It seems reasonable then to use (5) to calculate Δ as a function of position relative to the dislocation line ; in general

$$w=\sum_{ij}\int \sigma_{ij}\, d\epsilon_{ij}$$

where σ_{ij} and ϵ_{ij} are the i,j components of the stress and strain tensors respectively.

Hence for a screw dislocation $w=Gb^2/8\pi^2r^2$ where G is the shear modulus. This gives

$$\Delta=2\gamma\kappa Gb^2/8\pi^2r^2\equiv D/r^2. \qquad . \ . \ . \ . \ . \ . \quad (6)$$

This equation is similar to (3) where now

$$K=\gamma\kappa G=\gamma 3(1-2\nu)/2(1+\nu). \qquad . \ . \ . \ . \ . \ . \quad (7)$$

Some numerical values of K and D calculated from (7) and (6) for a few metals are shown in table 1. The values of γ used are those calculated by Grüneisen (Slater 1939). The figures in brackets are the values of K obtained by Seeger and Stehle (1956) using the experimental values of Clarebrough *et al.* (1955) for the change in density and stored energy when a deformed metal is annealed.

It seems reasonable to extend these considerations to the case of edge dislocations. For simplicity it will be assumed that the proportionality constant relating strain energy to dilatation is the same whether the energy is due to shear, compression or extension. It is then found that

$$w=\frac{Gb^2}{(1-\nu)8\pi^2r^2}\left(1+\frac{\nu}{1-\nu}\cos 2\phi\right). \qquad . \ . \ . \ . \quad (8)$$

Hence

$$\Delta=\frac{D}{r^2}\frac{1}{(1-\nu)}\left(1+\frac{\nu}{1-\nu}\cos 2\phi\right). \qquad . \ . \ . \ . \quad (9)$$

The average Δ over all ϕ is $D/r^2(1-\nu)$ which shows that the total density change due to an edge dislocation is greater than that due to a screw dislocation by a factor of $(1-\nu)^{-1}$. Again (8) and (9) are valid only for $r>R_0$; for $r<R_0$ a relation similar to (4) may be assumed to hold.

(*c*) There may be an additional dilatation due to the core of the dislocation. For simplicity this region will be assumed to be cylindrical, and its effect can be taken into account by a term similar to (4). On the Stehle and Seeger model the total volume change in a length b of the core is $Kb^3/4\pi=K\sqrt{2}\Omega/4\pi$ for a face-centred cubic lattice, where Ω=atomic volume$=b^3/\sqrt{2}$. If $K\sim 1$ the total volume change per atomic length of core is only $0{\cdot}11\Omega$. For a wide edge dislocation the total volume change at the core—effectively a slit parallel to the slip plane—may be somewhat greater, perhaps by a factor of five. In general the effect of the core may be taken into account by putting

$$\Delta=D_c/R_0^2 \qquad . \ . \ . \ . \ . \ . \ . \quad (10)$$

where D_c may have different values, ${}_sD_c$, ${}_eD_c$ for screw and edge dislocations. The precise values for ${}_sD_c$, ${}_eD_c$ are, however, in doubt.

§ 3. General Theory

The scattering from a crystal containing dislocations will of course depend on the arrangement of the dislocations. In the following calculations it will be assumed that dislocations of length $2H$ are randomly orientated with an average distance $2H$ between neighbouring dislocations. This arrangement is supposed to represent a random network of dislocations. There is some doubt about the effective radius of crystal over which the stress field of the dislocation extends. Dexter (1953) in his calculation of the scattering from edge dislocations on elastic theory assumed that the strain field due to a given dislocation extends effectively only over a distance of the order of half the separation of the dislocations ; Blin (1954, 1957), however, assumed that the strain field extends over the whole of the crystal. The latter hypothesis is certainly correct for a single dislocation in a crystal ; in principle it also applies for any dislocation array. In practice, however, for a random network, where dislocations of different sign and orientation are encountered, it is convenient to consider the nature of the *resultant* strain field. For a random network it appears likely that at least half the nearest neighbours will effectively be of opposite sign, so that the strain field of a given dislocation will extend only over half the distance between them, i.e. Dexter's hypothesis applies. Blin's explicit calculation for a finite length of dislocation (1957) confirms this view (see § 2).

It will be assumed therefore that dislocations of length $2H$ are effectively lying in cylinders of length $2H$ and radius $R=H$. These cylinders are randomly orientated, and irregularly close-packed at average separations $2H$. It is immediately apparent that such a model corresponds to a dense system of particles, like a liquid, so that interferences between neighbouring particles must be taken into account. If $A(\mathbf{s})$ is the Fourier transform ($\mathbf{s}$ is the reciprocal space vector) of the density variation due to a single dislocation in a cylinder (one ' particle '), it follows from scattering theory for a dense system of particles that the average intensity per dislocation, I is given by

$$I=\bar{A}^2+\bar{A}\bar{A}^*\int_0^\infty(\rho(p)-\rho_0)4\pi p^2\frac{\sin(2\pi ps)}{2\pi ps}dp \quad . \quad . \quad (11)$$

where $\bar{A}$, $\bar{A}^*$ and $\bar{A}^2$ represent the averages of $A(\mathbf{s})$, $A^*(\mathbf{s})$ and $|A(\mathbf{s})|^2$ respectively over a sphere of radius s, $\rho(p)$=number of dislocations per unit volume at a distance p from a given dislocation, ρ_0=average number of dislocations per unit volume. For a system with liquid-like close packing of the ' particles ' it is reasonable to assume to a first approximation that

$$\begin{aligned}\rho(p)&=0 \quad \text{for} \quad p<R,\\ \rho(p)&=\rho_0 \quad \text{for} \quad p>R.\end{aligned} \quad . \quad . \quad . \quad . \quad . \quad . \quad (12)$$

This corresponds to the simplest possible radial distribution function (cf. James 1954) applicable approximately to a dense gas. It follows that

$$I=(\bar{A}^2-\bar{A}\bar{A}^*)+\bar{A}\bar{A}^*(1-v\Phi(2\pi Rs)) \quad . \quad . \quad . \quad (13)$$

where $\Phi(kR)=3(\sin kR-kR\cos kR)/(kR)^3$, $k=2\pi s$ and $v=$volume occupied by the 'particles' per unit volume. In the particular dense system postulated here $v\simeq 1$, so that

$$I=(\bar{A}^2-\bar{A}\bar{A}^*)+\bar{A}\bar{A}^*(1-\Phi(2\pi Rs)). \quad . \quad . \quad . \quad (14)$$

It follows immediately that for $2\pi Rs<1$

$$I=\bar{A}^2-\bar{A}\bar{A}^*. \quad . \quad . \quad . \quad . \quad . \quad . \quad . \quad (15)$$

Under these conditions, as will be shown later,

$$\bar{A}^2=\bar{A}\bar{A}^* \quad . \quad . \quad . \quad . \quad . \quad . \quad . \quad (16)$$

so that $I=0$ for sufficiently small s, as expected from liquids. For $2\pi Rs>4$ (see James 1954, fig. 165),

$$I=\bar{A}^2, \quad . \quad . \quad . \quad . \quad . \quad . \quad . \quad . \quad (17)$$

the diffraction pattern is therefore similar to that due to liquids or glasses. As Dexter (1953) pointed out, $\bar{A}^2$ for an individual edge dislocation on elastic theory shows a peak at $2\pi Rs\sim 2{\cdot}5$, and falls to zero at $s=0$. For a random network of dislocations a peak would be expected in this region of s on *any* of the hypotheses considered for the density change due to dislocations. It should be pointed out, however, that eqns. (11), (13), (14) and (15) were derived on the assumption that all the particles are identical. However, in general the 'particles' are not identical; for example, edge and screw dislocations have different scattering amplitudes. If it is assumed for simplicity that the dislocations are either screw or edge, i.e. that the system consists essentially of two types of 'particles' of the same size but of different scattering amplitudes, the intensity at zero angle corresponding to (15) will be proportional to the square of the difference of scattering amplitude between screw and edge dislocations and will depend on their relative proportions. The scattering at $2\pi Rs<1$ is therefore uncertain. Most of the experiments carried out so far have covered a range of s satisfying $2\pi Rs>4$ for all reasonable dislocation densities, so that (17) applies. It should be noted that a similar expression applies even when the 'particles' have different scattering amplitudes, A_s and A_e for screw and edge dislocations, that is

$$I=n_s\bar{A}_s^2+n_e\bar{A}_e^2 \quad . \quad . \quad . \quad . \quad . \quad . \quad (18)$$

where n_s and n_e are the proportion of screw and edge dislocations. The scattering will now be calculated for this range of s.

Consider a dislocation of length $2H$ (fig. 2) on the axis of a cylindrical crystal of radius $R=H$; the radius of the core is R_0. Any point P in the crystal is described by the vector $\mathbf{P}(r, \phi, z)$. For the case of edge dislocations the Burgers vector $\mathbf{b}$ lies along the x-axis. The reciprocal space vector $\mathbf{s}$ has components (s_r, ξ, s_z) and its magnitude is given by $s=2\sin\theta/\lambda\simeq 2\theta/\lambda$ for small angles, where 2θ is the scattering angle,

i.e. the angle between the incident and scattered rays. It is useful to define another vector $\mathbf{k}\ (k_r, \xi, k_z)=2\pi\mathbf{s}$. χ is the angle between $\mathbf{s}$ and the z-axis, so that $k_r=k\sin\chi$, $k_z=k\cos\chi$.

The amplitude of the radiation scattered by the dislocated crystal is

$$A(\mathbf{k})=\frac{A_a}{\Omega}\int_{\text{crystal}} \Delta \exp(i\mathbf{k}\,.\,\mathbf{P})\,dv \quad . \quad . \quad . \quad . \quad (19)$$

where A_a is the amplitude scattered from one atom under the same conditions and Ω is the atomic volume.

In terms of the cylindrical coordinates of fig. 2

$$A=\frac{A_a}{\Omega}\int_{z=-H}^{+H}\int_{\phi=0}^{2\pi}\int_{r=0}^{R} \Delta \exp\,[i\{zk_z+rk_r\cos(\xi-\phi)\}]r\,dr\,d\phi\,dz. \quad (20)$$

For the cases considered here, Δ is not a function of z. Hence

$$A=\frac{A_a}{\Omega}\int_{-H}^{+H}\exp(izk_z)\,dzX \quad . \quad . \quad . \quad . \quad . \quad (21)$$

where

$$X=\int_0^{2\pi}\int_0^{R} r\Delta \exp\{irk_r\cos(\xi-\phi)\}\,dr\,d\phi. \quad . \quad . \quad . \quad (22)$$

Integrating with respect to z

$$A=\frac{A_a}{\Omega}2H\frac{\sin Hk_z}{Hk_z}X. \quad . \quad . \quad . \quad . \quad . \quad . \quad (23)$$

Then

$$\bar{A}=2H\frac{A_a}{\Omega}\int_0^{2\pi}\int_0^{\pi}\frac{1}{4\pi}\frac{\sin(Hk\cos\chi)}{(Hk\cos\chi)}X\sin\chi\,d\chi\,d\xi \quad . \quad . \quad (24)$$

and

$$\bar{A}^2=4H^2\frac{A_a^2}{\Omega^2}\int_0^{2\pi}\int_0^{\pi}\frac{1}{4\pi}\frac{\sin^2(Hk\cos\chi)}{(Hk\cos\chi)^2}|X|^2\sin\chi\,d\chi\,d\xi \quad . \quad . \quad (25)$$

$$=\frac{4H}{k}\frac{A_a^2}{\Omega^2}\int_0^{2\pi}\int_{-Hk}^{+Hk}\frac{1}{4\pi}|X|^2\frac{\sin^2 y}{y^2}dy\,d\xi \quad . \quad . \quad . \quad . \quad . \quad (26)$$

where $y=Hk\cos\chi=Hk_z$.

Two approximations will be considered :

(1) For $2\pi Rs=kH<1$,

$$\bar{A}=2H\frac{A_a}{\Omega}\int_0^{2\pi}\int_0^{\pi}\frac{1}{4\pi}X\sin\chi\,d\chi\,d\xi \quad . \quad . \quad . \quad . \quad . \quad (27)$$

and

$$\bar{A}^2=4H^2\frac{A_a^2}{\Omega^2}\int_0^{2\pi}\int_0^{\pi}\frac{1}{4\pi}|X|^2\sin\chi\,d\chi\,d\xi. \quad . \quad . \quad . \quad . \quad (28)$$

(2) For $2\pi Rs=kH>4$, $\sin(Hk\cos\chi)/(Hk\cos\chi)$ is appreciable only for $\chi\to\frac{1}{2}\pi$; hence the limits $\pm Hk$ of the integral with respect to y

in (26) can be extended to $\pm\infty$, and $|X|^2$ can be taken outside the integral sign, so that

$$\bar{A}^2=\frac{HA_a^2}{\pi k\Omega^2}\int_0^{2\pi}|X|^2\,d\xi\int_{-\infty}^{+\infty}\frac{\sin^2 y}{y^2}\,dy$$
$$=\frac{HA_a^2}{k\Omega^2}\int_0^{2\pi}|X|^2\,d\xi. \qquad \ldots\ldots \quad (29)$$

X is a function of k_r which is equal to k in this approximation. A similar expression can be obtained for $\bar{A}$, which will not be required here. The justification for the approximation made in (29) depends on the fact that $\sin^2(Hk_z)/(Hk_z)^2$ decreases more rapidly with increasing k_z than does $|X|^2$ with k_r. This is true for all the models considered, and calculations have shown that the use of (29) introduces an error of less than 10%.

Expression (29) represents the scattered intensity from a volume of crystal containing one dislocation. The intensity scattered per unit volume, I_v, is therefore

$$I_v=\frac{\bar{A}^2}{2\pi R^2H}=\bar{A}^2\frac{L}{2H}=\frac{L}{4\pi s\Omega^2}A_a^2\int_0^{2\pi}|X|^2\,d\xi \qquad \ldots \quad (30)$$

where L=total length of dislocation line per unit volume (i.e. dislocation density).

It remains to calculate X. If the contributions to X due to the elastic strain field, the second-order elasticity effect and the core are X_e, X_s and X_c respectively,

$$\left.\begin{aligned} &X=X_e+{}_eX_s+{}_eX_c, \text{ for an edge dislocation}\\ \text{and}\\ &X={}_sX_s+{}_sX_c, \qquad \text{for a screw dislocation}\end{aligned}\right\} \qquad \ldots \quad (31)$$

the subscripts preceding the letters X standing for edge and screw respectively.

§ 4. Edge Dislocation on First Order Elasticity Theory

$$X_e=\int_0^{2\pi}\int_{R_0}^{R}F\sin\phi\exp\{irk_r\cos(\xi-\phi)\}\,dr\,d\phi$$
$$=2\pi iRF\sin\xi\{J_0(x_0)-J_0(x)\}/x \qquad \ldots\ldots \quad (32)$$

where $x=Rk_r$, $x_0=R_0k_r$. For $x<1$ and decreasing to zero, X_e goes to zero, as already pointed out by Dexter (1953), and hence I also goes to zero.

For $x>4$, (32) can be used; but generally $x_0<1$ so that

$$X_e=2\pi iRF\sin\xi\{1-J_0(x)\}/x \qquad \ldots \quad (33)$$

is a good approximation. If the oscillations of $J_0(x)$ are neglected for $x>4$, the term in the brackets reduces to $1/x$. The validity of this

approximation can be judged from fig. 3 (after Blin 1954). Equation (33) then takes the simple form

$$X_e = 2\pi i F \sin \xi / k_r. \qquad (34)$$

From (30) and (33),

$$\frac{I_v}{A_a^2} = \frac{L}{4\pi s \Omega^2}\left[\frac{\pi F^2\{1-J_0(x)\}^2}{s^2}\right]. \qquad (35)$$

If $J_0(x)$ can be neglected as above,

$$\frac{I_v}{A_a^2} = \frac{L}{4\pi s \Omega^2}\frac{\pi F^2}{s^2}. \qquad (36)$$

Hence I_v/A_a^2 is seen to vary approximately as s^{-3}. Figure 5 (1) shows (36) as a function of s.

Fig. 3

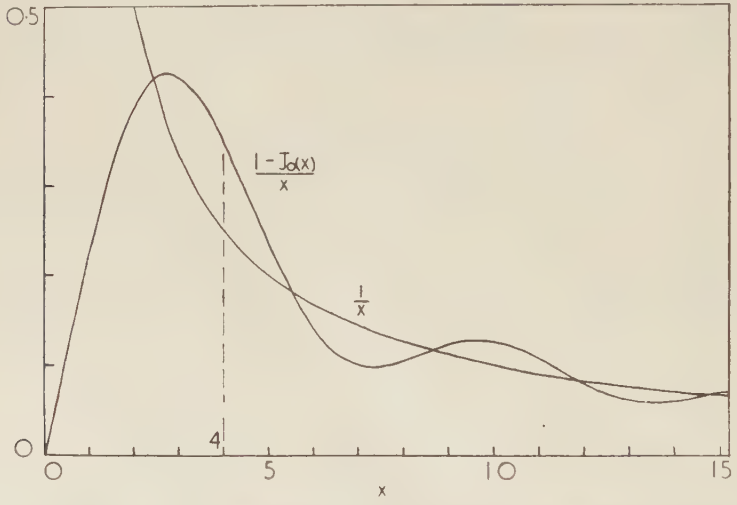

(After Blin 1954). In the calculation of the first order elasticity effect for edge dislocations, the curve $1/x$ is used to approximate the curve $\{1-J_0(x)\}/x$ for $x>4$.

It is clear from (36) that $I_v A_a^2$ is independent of the coherent length $2H$ of the dislocation. In a recent paper Blin (1957) used an equation similar to (36) to explain his observed scattering intensities, but apparently owing to a confusion with regard to the definition of dislocation density, the scattered intensity is found, incorrectly, to depend on H.

§ 5. Second Order Elasticity Effect

5.1. *For a Screw Dislocation*

$$_sX_s = \int_0^{2\pi}\int_{R_0}^{R} \frac{D}{r}\exp\{irk_r\cos(\xi-\phi)\}\,dr\,d\phi$$

$$= 2\pi D\int_{x_0}^{x}\{J_0(x')/x'\}\,dx' \equiv 2\pi DS. \qquad (37)$$

For $x<1$,

$$_sX_s=2\pi D \ln (R/R_0) \quad . \quad . \quad . \quad . \quad . \quad . \quad (38)$$

a constant independent of χ and ξ. Hence $\bar{A}^2=\bar{A}\bar{A}^*$ under these conditions, and as before I goes to zero as x goes to zero. For larger x the integral has been evaluated by dividing it into two parts:

$$_sX_s=2\pi D\left[\int_{x_0}^{0\cdot6}\{J_0(x')/x'\}\,dx'+\int_{0\cdot6}^{x}\{J_0(x')/x'\}\,dx'\right]$$
$$\equiv 2\pi D[S_1+S_2] \quad . \quad . \quad . \quad . \quad . \quad (39)$$

where $S_1+S_2=S$. S_1 may be expanded as a power series and integrated as for (38), giving approximately $S_1=\ln (0\cdot6/x_0)$; this approximation introduces an error of $<10^0{}_0$. S_2 has been calculated numerically giving the values shown in fig. 4. For $x>1\cdot5$, S_2 approaches the value 0·68. In this region of x, therefore, X is independent of R. For $x>4$ and $x_0<0\cdot6$, which is usually satisfied,

$$_sX_s=2\pi D[\ln (0\cdot6/x_0)+0\cdot68]. \quad . \quad . \quad . \quad . \quad . \quad (40)$$

It follows from (30), that

$$\frac{I_v}{A_a{}^2}=\frac{L}{4\pi s\Omega^2}\left[8\pi^3D^2\left\{\ln\left(\frac{0\cdot6}{2\pi R_0 s}\right)+0\cdot68\right\}^2\right]. \quad . \quad . \quad (41)$$

Fig. 4

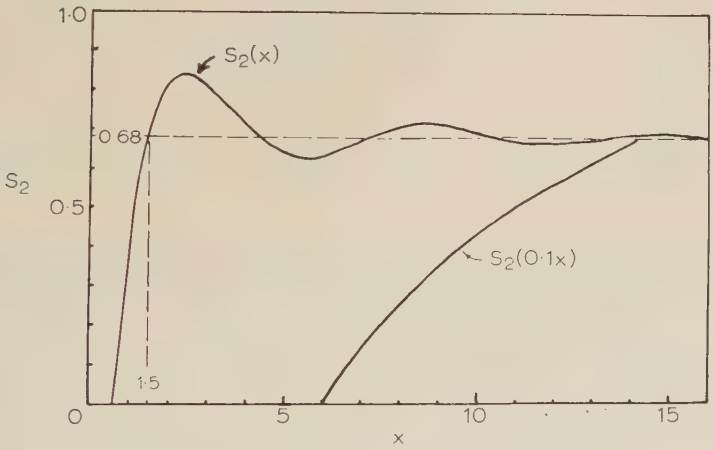

Value of the integral $S_2(x)=\int_{0\cdot6}^{x}\{J_0(x')/x'\}\,dx'$ used in the calculation of the second order elasticity effect. The variation of $S_2(x)$ for $x<1\cdot5$ can be followed more clearly on the curve of $S_2(0\cdot1x)$ which is also shown.

Figure 5 (2*a*) shows the curve of (41) for $R_0=\frac{1}{3}b$, the value favoured by Stehle and Seeger. As it is unlikely that R_0 is less than $\frac{1}{3}b$, $R_0=\frac{1}{3}b$ results in the greatest scattering possible for this effect. It appears that in this range of angles the scattering is generally smaller and decreases less rapidly with increasing s than that due to edge dislocations on first-order elastic theory.

Fig. 5

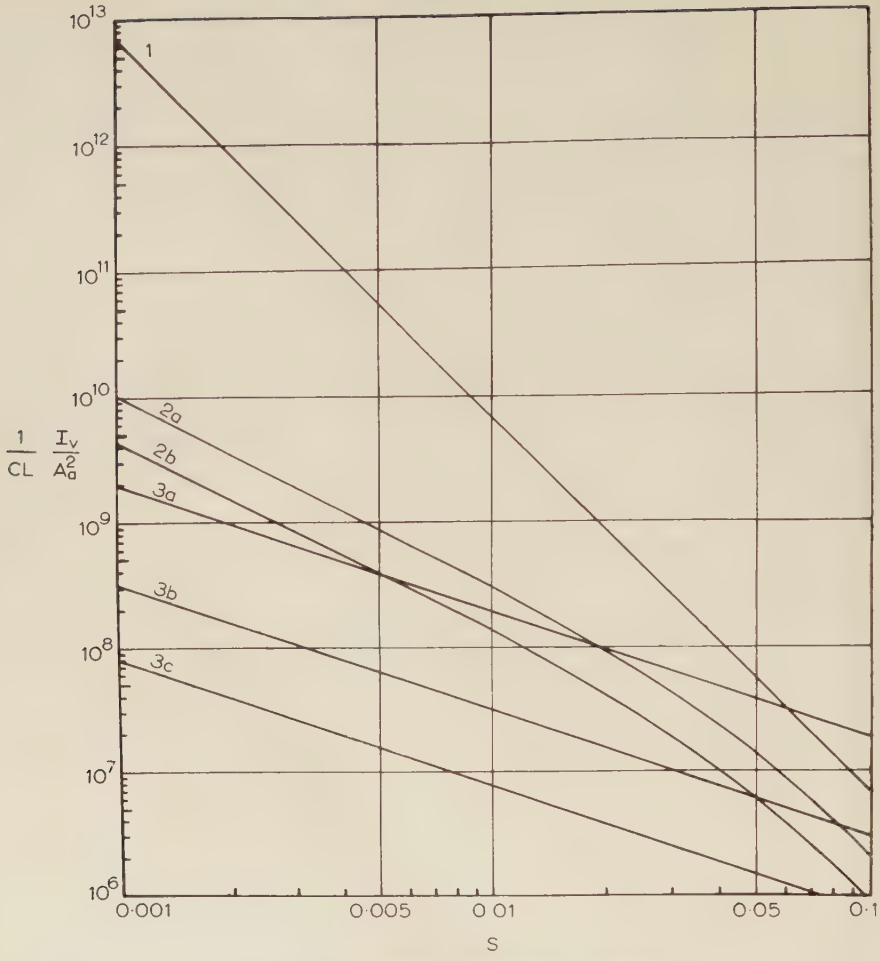

Graphs of the intensity scattered at small angles as a function of $s=2\sin\theta/\lambda$ (Å^{-1}). The curves have been evaluated for Cu, for unit density of dislocations; the ordinates represent values of $(1/CL)(I_v/A_a^2)$; C is a scaling factor which is unity for Cu, L is the dislocation density.

(1) First order elasticity effect (eqn. (36)).

(2) Second order elasticity effect for (*a*) edge dislocations, $R_0=\frac{1}{3}b=0{\cdot}85$ Å (eqn. (46)); (*b*) screw dislocations, $R_0=\frac{1}{3}b=0{\cdot}85$ Å (eqn. (41)).

(3) Core effect for total volume changes per atomic length of dislocation core of (*a*) $\frac{1}{2}\Omega$, (*b*) $1/5\Omega$, (*c*) $1/10\Omega$ (eqn. (49)).

These curves can also be used for other metals; the appropriate scaling factors are given below; in the case of the second order elasticity effect, the core radius is taken equal to the value assumed for Cu in each case, i.e., $R_0=0{\cdot}85$ Å.

	Value of C for				
Curve	Al	Fe	Ni	Cu	Pb
1	0·69	1·5	1·4	1·0	0·061
2(*a*)	1·1	1·0	1·3	1·0	0·18
2(*b*)	1·1	1·2	1·4	1·0	0·14
3(*a*), 3(*b*), 3(*c*)	0·80	1·1	1·1	1·0	0·53

5.2. *For an Edge Dislocation*

$$_eX_s=\int_0^{2\pi}\int_{R_0}^{R}\frac{D}{r}\frac{1}{(1-\nu)}\left(1+\frac{\nu}{1-\nu}\cos 2\phi\right)\exp\{irk_r\cos(\xi-\phi)\}\,dr\,d\phi. \qquad (42)$$

This is the sum of two integrals. Hence

$$_eX_s=\frac{2\pi D}{(1-\nu)}\left[S-\frac{\nu}{2(1-\nu)}\cos 2\xi\left\{\frac{2J_1(x_0)}{x_0}-\frac{2J_1(x)}{x}\right\}\right] \qquad (43)$$

where S was defined in the previous section. For $x\ll 1$ and $x_0\ll 1$, eqn. (43) becomes

$$_eX_s=2\pi DS/(1-\nu). \qquad (44)$$

Thus here also $_eX_s$ is independent of χ and ξ and I goes to zero as x goes to zero. For all x (including $x>4$), and for $x_0<0{\cdot}6$

$$_eX_s=\frac{2\pi D}{(1-\nu)}\left[\left\{\ln\left(\frac{0{\cdot}6}{x_0}\right)+0{\cdot}68\right\}-\frac{\nu}{2(1-\nu)}\cos 2\xi\left\{1-\frac{2J_1(x)}{x}\right\}\right]. \qquad (45)$$

After performing the integration of eqn. (30) it appears that the last term in (45) can be neglected. Hence

$$\frac{I_v}{A_a{}^2}=\frac{L}{4\pi s\Omega^2}\left[\frac{8\pi^3D^2}{(1-\nu)^2}\left\{\ln\left(\frac{0{\cdot}6}{2\pi R_0 s}\right)+0{\cdot}68\right\}^2\right]. \qquad (46)$$

Thus for edge dislocations the intensity is larger than for screw dislocations by a factor $(1-\nu)^{-2}$. Figure 5 (2*b*) shows the curve of $I_v/A_a{}^2$ for $R_0=\frac{1}{3}b$.

§ 6. Dislocation Core

$$X_c=\int_0^{2\pi}\int_0^{R_0}r\frac{D_c}{R_0{}^2}\exp\{irk_r\cos(\xi-\phi)\}\,dr\,d\phi$$
$$=2\pi D_cJ_1(x_0)/x_0. \qquad (47)$$

Generally $x_0<1$, so that

$$X_c=\pi D_c. \qquad (48)$$

Hence, for $x>4$,

$$\frac{I_v}{A_a{}^2}=\frac{L}{4\pi s\Omega^2}[2\pi^3D_c{}^2]. \qquad (49)$$

Again, $\bar{A}^2=\bar{A}\bar{A}^*$, so that I goes to zero as x goes to zero. It is clear from (10) that the total volume change per unit length of dislocation core is πD_c, so that (49) shows that the scattering depends only on the total volume change at the core, rather than its density. Figure 5 (3) shows curves of $I_v/A_a{}^2$ as a function of s for several values of D_c corresponding to total volume changes per one atomic length of core of $\frac{1}{10}$, $\frac{1}{5}$, $\frac{1}{2}\Omega$ respectively. It appears, as expected, that the scattering due to the core decreases less rapidly with increasing s than the scattering due to either of the other two causes.

§ 7. Discussion

The total intensity of scattering including all the contributions is found by (18) and (31) to be

$$\frac{I_v}{A_a{}^2}=\frac{L}{4\pi s\Omega^2}\int_0^{2\pi}[n_e\{X_e{}^2+(_eX_s+{}_eX_c)^2\}+n_s\{{}_sX_s+{}_sX_c\}^2]\,d\xi \qquad (50)$$

where n_e, n_s are the proportions of edge and screw dislocations in the total dislocation density L. For $2\pi Rs>4$ and $2\pi R_0 s<0{\cdot}6$ this expression becomes

$$\frac{I_v}{A_a{}^2}=\frac{L}{4\pi s\Omega^2}\left[n_e\left\{\frac{\pi F^2}{s^2}+2\pi\left(\frac{2\pi D}{(1-\nu)}\left[\ln\left(\frac{0{\cdot}6}{2\pi R_0 s}\right)+0{\cdot}68\right]+\pi_e D_c\right)^2\right\}\right.$$
$$\left.+n_s 2\pi\left\{2\pi D\left[\ln\left(\frac{0{\cdot}6}{2\pi R_0 s}\right)+0{\cdot}68\right]+\pi_s D_c\right\}^2\right]. \quad . \quad . \quad . \quad . \quad (51)$$

This expression shows immediately that the scattering in this range of s values depends only on the total dislocation density, L, and not on the coherent length of the dislocations.

It appears from fig. 5 that over most of the range of scattering angles the scattering due to the elastic strain field predominates. The intensity of this scattering, however, decreases faster with increasing s than that due to other causes, so that it is possible that at large values of s the three effects, although small, may become comparable.

Table 2. The Range of s Values ($s_{\min}$ to $s_{\max}$) for which eqns. (36), (41), (46), (49) and (51) are valid

$L\ \frac{\text{cm}}{\text{cm}^3}$	10^{10}	3×10^{10}	10^{11}	3×10^{11}	10^{12}
$2R=2H$ (Å)	1130	652	357	206	113
$s_{\min}$ (Å^{-1})	0·0011	0·0020	0·0036	0·0062	0·011
$2\theta_{\min}$ $\lambda=1{\cdot}54$ Å	6·0′	10′	19′	33′	1·0°
$2\theta_{\min}$ $\lambda=9$ Å	35′	1·0°	1·8°	3·2°	5·8°

R_0	$\frac{1}{2}b$	$\frac{1}{3}b$
$s_{\max}$ for Cu	0·075	0·11
$2\theta_{\max}$ $\lambda=1{\cdot}54$ Å	6·6°	9·9°
$2\theta_{\max}$ $\lambda=9$ Å	39°	60°

$s_{\min}=4/2\pi R=2\sqrt{(L/\pi)}$, where L is the dislocation density. $s_{\max}=0{\cdot}6/2\pi R_0$, where R_0 is the radius of the dislocation core. Values of $2\theta_{\min}$ and $2\theta_{\max}$, the corresponding mimimum and maximum scattering angles, are given for typical x-ray (1·54 Å) and cold neutron (9 Å) wavelengths.

Table 2 shows the lower limit of s (i.e. $s_{\min}=4/2\pi R$) above which (51) applies, for different dislocation densities. The corresponding lower limits of the scattering angles and the upper limit of s (i.e. $s_{\max}=0{\cdot}6/2\pi R_0$) for copper are also shown. The experiments of Blin and Guinier were in fact mostly carried out with copper K_α radiation (1·54 Å) in the range $1°<2\theta<5°$, which is the range in which (51) is seen to apply, whatever the dislocation density. Since the scattering from the elastic strain field predominates, at least at the lower end of this range, and if an appreciable proportion of the dislocations are in the edge orientation,

the order of magnitude of the scattered intensity can be estimated simply from the first term of (51). The scattered intensities are usually expressed in terms of differential scattering cross sections per atom. For x-rays a convenient unit to use is $\tau(s)$, the scattered intensity per atom of material expressed in terms of the scattered intensity from one electron, I_{el}; thus

$$\tau(s)=\Omega(I_v/I_{el})=\Omega Z^2(I_v/A_a{}^2)\equiv B_1(I_v/A_a{}^2). \quad . \quad . \quad (52)$$

For neutrons a convenient differential cross section is $d\sigma(s)$ (millibarns per steradian per atom) given by

$$d\sigma(s)=(\Omega\mathscr{S}10^3/4\pi)(I_v/A_a{}^2)\equiv B_2(I_v/A_a{}^2) \quad . \quad . \quad (53)$$

where $\mathscr{S}$ is the coherent scattering cross section of one nucleus in barns. Values of B_1 and B_2 are given for some metals in table 3.

Table 3. Relationship between $(I_v/A_a{}^2)$ and the Differential Cross Sections

Metal	B_1	B_2
Al	$2{\cdot}79\times10^{-21}$	$1{\cdot}97\times10^{-21}$
Fe	7·92	10·6
Ni	8·55	11·6
Cu	9·88	6·82
Pb	202	27·6

For x-rays, $\tau(s)=B_1(I_v/A_a{}^2)$ electrons per atom (eqn. (52)); for neutrons, $d\sigma(s)=B_2\,(I_v/A_a{}^2)$ millibarns per steradian per atom (eqn. (53)).

For cold-worked copper, assuming an edge dislocation density of 10^{11} cm^{-2}, the scattering cross section at $s\simeq0{\cdot}01$ Å^{-1} (corresponding to $2\theta=1^\circ$ for $\lambda=1{\cdot}54$ Å) is then found to be 7 electrons per atom or 4·8 millibarns per steradian per atom for neutrons, for the elastic strain field effect. This value is about 20 to 200 times smaller than that reported by Blin and Guinier, but of the same order of magnitude as the observed neutron scattering, which will be reported in a later paper by Atkinson and Lowde. Blin (1957) has suggested that even the large intensities observed in his experiments could be explained on the elastic strain field effect; although no explicit statement was made, presumably reasonable dislocation densities were assumed. However, this conclusion is incorrect and arose as a result of the confusion already referred to in § 4.

It appears then that unless screw dislocations predominate in the metal, the small angle scattering in the experimentally observed range of scattering angles will be mainly due to the elastic strain field of edge dislocations, except perhaps for a contribution due to the core at high angles. The second-order elastic effect does not seem to be important

in this range, although of course it is important with regard to total density changes (Stehle and Seeger 1956).

Distributions of dislocations other than the random network have to be considered individually. However, for pile-ups containing closely-spaced dislocations the scattering may be considerably greater; as a limiting approximation b in Δ might be replaced by nb where n is the effective number of dislocations in the pile-up. Thus the scattering per dislocation on first-order elasticity theory (the Dexter model) will be proportional to n, on second-order theory (the Seeger and Stehle model) to n^3. However, only the very closely-spaced dislocations at the head of the pile-ups could contribute to this effect. On the other hand, regular arrays of dislocations in low angle boundaries could lead to interference effects. Recent electron microscope observations on thin foils of cold-worked copper (Murphy 1957) show, however, a very irregular arrangement of dislocations, so that the model of a random network appears to be reasonable.

Acknowledgments

The authors are indebted to Professor N. F. Mott, F.R.S., and to Dr. W. H. Taylor for their interest and encouragement. One of the authors (H. H. A.) wishes to thank the Master and Fellows of Corpus Christi College for the award of the Plumian Research Studentship and the Imperial Chemical Industries for a maintenance grant.

References

Atkinson, H. H., and Lowde, R. D., 1957, *Phil. Mag.*, **2,** 589.

Beeman, W. W., Kaesberg, P., Anderegg, J. W., and Webb, M. B., 1957, *Handb. Physik*, **32,** 440.

Blin, J., 1954, *Thesis*, University of Paris; 1955, *Defects in Crystalline Solids* (London: The Physical Society,), p. 420; 1957, *Acta Met.*, **5,** 528.

Blin, J., and Guinier, A., 1951, *C. R. Acad. Sci., Paris*, **233,** 1288; 1953, *Ibid.*, **236,** 2150.

Clarebrough, L. M., Hargreaves, M. E., and West, G. W., 1955, *Proc. roy. Soc.* A, **232,** 252.

Dexter, D. L., 1953, *Phys. Rev.*, **90,** 1007.

Hayes, S., and Smoluchowski, R., 1954, *Appl. sci. Res., Hague*, B, **4,** 10.

James, R. W., 1954, *The Optical Principles of the Diffraction of X-rays* (London: Bell).

Lomer, W. M., 1957, *Phil. Mag.*, **2,** 1053.

Murphy, H. M., 1957, unpublished results.

Robinson, W. H., and Smoluchowski, R., 1956, *J. appl. Phys.*, **27,** 657.

Seeger, A., 1956, *Z. Naturf.*, **11***a*, 724; 1957, *Acta Met.*, **5,** 24.

Seeger, A., and Stehle, H., 1956, *Z. Phys.*, **146,** 242.

Slater, J. C., 1939, *Introduction to Chemical Physics* (New York: McGraw-Hill), p. 451.

Stehle, H., and Seeger, A., 1956, *Z. Phys.*, **146,** 217.

Weiss, R. J., Clark, J. R., Corliss, L., and Hastings, J., 1952, *J. appl. Phys.*, **23,** 1379.

Zhurkov, S. N., and Slutsker, A. I., 1957, *Zh. tekh. Fiz.*, **27,** 1392.

Calculations of Solid-State Data of Neon, and the Vapour Pressure Ratio of its Isotopes†

By T. F. Johns
Atomic Energy Research Establishment, Harwell, Berks.

[Received December 21, 1957]

Abstract

Calculations have been made of the free energies and equations of state of solid ^{20}Ne and ^{22}Ne, using the method of Henkel. The vapour pressure ratio of the neon isotopes deduced from the calculated difference in their free energies is in excellent agreement with experimental measurements. Although the molecular volumes of the two isotopes differ by about 0·5%, the vapour pressure ratio can be calculated quite accurately on the assumption that there is no such volume effect ; the reasons for this are explained.

§ 1. Introduction

More than 20 years ago Keesom and Haantjes (1935) calculated the vapour pressure ratio of the (solid) neon isotopes, assuming that the binding energies of the two species are the same and that the frequencies of oscillation of the atoms in the crystal lattice are inversely proportional to the square roots of their masses. Though their calculated results were in reasonable agreement with their experimental results (being about 25% lower throughout the temperature range investigated) it has been made clear, by the work of de Boer (1948) and others, that the assumptions made in the calculation are in fact far from true. For a low-boiling substance such as neon the zero-point energy is of considerable importance in determining the thermodynamic properties, and since the lighter isotope has a larger zero-point energy, it has a slightly larger molecular volume, and the atoms are less strongly bound in the solid state. The recently developed method of Henkel (1955) makes it possible to calculate rather precisely the solid-state properties of inert gases, from quite basic principles, and this method has therefore been used to calculate the vapour pressure ratio of ^{20}Ne, ^{22}Ne. The calculated values are in excellent agreement with the experimental results. The calculation makes clear why the method of calculation used by Keesom and Haantjes yields such satisfactory results in spite of its wrong premises.

§ 2. Henkel's Method

Henkel's method is essentially a modified and refined Einstein treatment of a crystal lattice, taking due account of anharmonicity in the vibrations of the atoms. Henkel assumes that the potential energy of

† Communicated by the Author.

one atom due to another identical atom as distance r is given by

$$\phi = \frac{A}{r^n} - \frac{B}{r^6} \quad . \quad . \quad . \quad . \quad . \quad . \quad . \quad . \quad (1)$$

(he puts $n=10$) and proceeds to calculate the partition function of the solid as a function of r, n, A and B. From the partition function, the Helmholtz free energy and the pressure can be calculated, thus giving the equation of state of the solid. The thermal expansion, compressibility and specific heat can then be calculated. It has been shown (Domb and Zucker 1956) that in the case of argon this theory leads to results which are in most excellent agreement with experiment. Also Zucker (1956) has shown that the theory leads to correct values for the compressibility of solid neon and krypton, if suitable values of n are chosen in the above equation.

In the present calculation, it has been assumed that for neon, eqn. (1) has the form

$$\phi = \frac{A}{r^{14}} - \frac{B}{r^6}, \quad . \quad . \quad . \quad . \quad . \quad . \quad . \quad . \quad (2)$$

where $A=0{\cdot}373\times10^{-119}$ erg cm^{14}, and $B=0{\cdot}90\times10^{-59}$ erg cm^6; these values are almost identical to those used by Zucker (1956), the only difference being that the value of B chosen is about 1% greater (this leads to a slightly better figure for the latent heat of evaporation).

The Helmholtz free energy f per atom of each isotopic species, mass M, has then been calculated at various temperatures T from Henkel's equations :

$$f=-kT \ln Q, \quad . \quad . \quad . \quad . \quad . \quad . \quad . \quad . \quad . \quad . \quad . \quad . \quad . \quad (3)$$

$$Q=\exp\left(-\frac{P_0}{2kT}\right)\exp\left(-\frac{3W}{2kT}\right)\left\{\sum_{n=0}^{\infty}\left[\exp-\frac{1}{kT}(nW+n^2Y)\right]\right\}^3, \quad . \quad . \quad . \quad (4)$$

$$W=\frac{h}{2\pi}\cdot\left(\frac{2P_2}{M}\right)^{1/2}+Y, \quad . \quad . \quad . \quad . \quad . \quad . \quad . \quad . \quad . \quad . \quad (5)$$

$$Y=\frac{3}{4}\cdot\left(\frac{h}{2\pi}\right)^2\cdot\frac{P_4}{MP_2}, \quad . \quad . \quad . \quad . \quad . \quad . \quad . \quad . \quad . \quad . \quad (6)$$

$$P_0=\frac{AD_7}{a^{14}}-\frac{BD_3}{a^6}, \quad . \quad . \quad . \quad . \quad . \quad . \quad . \quad . \quad . \quad . \quad (7)$$

$$P_2=\frac{91AD_8}{3a^{16}}-\frac{5BD_4}{a^8}, \quad . \quad . \quad . \quad . \quad . \quad . \quad . \quad . \quad . \quad . \quad (9)$$

$$P_4=\frac{1820AD_9}{3a^{18}}-\frac{70BD_5}{3a^{10}}, \quad . \quad . \quad . \quad . \quad . \quad . \quad . \quad . \quad . \quad . \quad (9)$$

$$a=2\,.\,d, \quad . \quad . \quad . \quad . \quad . \quad . \quad . \quad . \quad . \quad . \quad . \quad . \quad . \quad . \quad . \quad . \quad (10)$$

where d is the distance between nearest neighbours in the crystal lattice,

and D_3–D_9 are lattice sums of the form calculated by Lennard-Jones and Ingham (1925), namely

$$D_3=115{\cdot}631, \qquad D_4=204{\cdot}831,$$
$$D_5=393{\cdot}960, \qquad D_7=1543{\cdot}551,$$
$$D_8=3078{\cdot}912, \qquad D_9=6150{\cdot}656.$$

Q is the partition function of the solid, $P_0/2$ represents the potential energy (per atom) in the crystal lattice, and $3W/2$ the zero-point energy. Y is the part of W associated with anharmonicity.

Values of P_0, P_2, P_4, Y, W, Q and hence f were calculated, for each temperature, at a number of values of a. The equilibrium state corresponds to $df/da=0$ (this assumes that the vapour pressure of neon is negligibly small compared with the pressure necessary to cause appreciable compression of the solid, which is in fact the case). Hence, for each temperature, the equilibrium value a_e of a was determined, and hence the equilibrium value of f. Having made the calculation for the two isotopic species, masses M_1, M_2, the difference between their Helmholtz free energies (f_1-f_2), was calculated, and it was assumed that this was also equal to the difference between their Gibbs free energies. This assumption leads to a negligible error, since the values of pv for the two solids are not only numerically small, but very nearly equal to one another.

Equating the difference of the Gibbs free energies to the corresponding difference per atom for the two vapours, leads to the equation

$$\ln\frac{p_1}{p_2}-\frac{3}{2}\ln\frac{M_1}{M_2}=\frac{f_1-f_2}{kT}, \qquad \ldots\ldots\ldots \quad (11)$$

for the vapour pressure ratio of the two species, if we ignore the correction due to the deviations of the vapours from the ideal gas laws. (It is probable that the deviations for the two isotopic species are nearly equal to one another). The vapour pressure ratio of the solids was calculated directly from eqn. (11).

§ 3. Results of the Calculation

The chief results of the calculations are shown in the table, which is self-explanatory. The calculated values for the lattice spacing and latent heat of evaporation (of natural neon) at 0°K are respectively 3·21 Å and 448 cal/mole, which are both practically identical with the experimental values (Hirschfelder *et al.* 1954).

The calculated values of the vapour pressure ratio are shown in fig. 1. They are in remarkably good agreement with the experimental results of Keesom and Haantjes. The variation of $(f_1-f_2)/k$ with temperature is as shown in fig. 2.

The molecular volume of ^{20}Ne is greater than that of ^{22}Ne by about 0·5% at 0°K and by about 0·4% at 20–24°K. Because of the difference in volumes, there is a difference in the potential energies per atom at 0°K of $1{\cdot}8\times10^{-16}$ ergs. This is far greater than the difference

Results of Calculation

Temperature (°K)	0		12		20		22		24	
Isotope	^{20}Ne	^{22}Ne	^{20}Ne	^{22}Ne	^{20}Ne	^{22}Ne	^{20}Ne	^{22}Ne	^{20}Ne	^{22}Ne
a_e (Å)	4·5385	4·530	4·542	4·534	4·564	4·5575	4·572	4·566	4·581	4·575
$f_{\min}$ (ergs 10^{-14} per atom)	3·0875	3·1416	3·0920	3·1471	3·1400	3·2008	3·1632	3·2262	3·1912	3·2567
$(f_1-f_2)/k$ (°K)	3·94		4·02		4·43		4·59		4·78	
$\ln(p_1/p_2)$	—		0·192		0·0785		0·0660		0·0566	

($0{\cdot}33 \times 10^{-16}$ ergs per atom) invoked by Keesom and Haantjes as a possible means of explaining why their calculated results were lower than their experimental ones. But the volume difference has another effect—it reduces the difference in zero-point energies from the value $5{\cdot}4 \times 10^{-16}$ ergs

Fig. 1

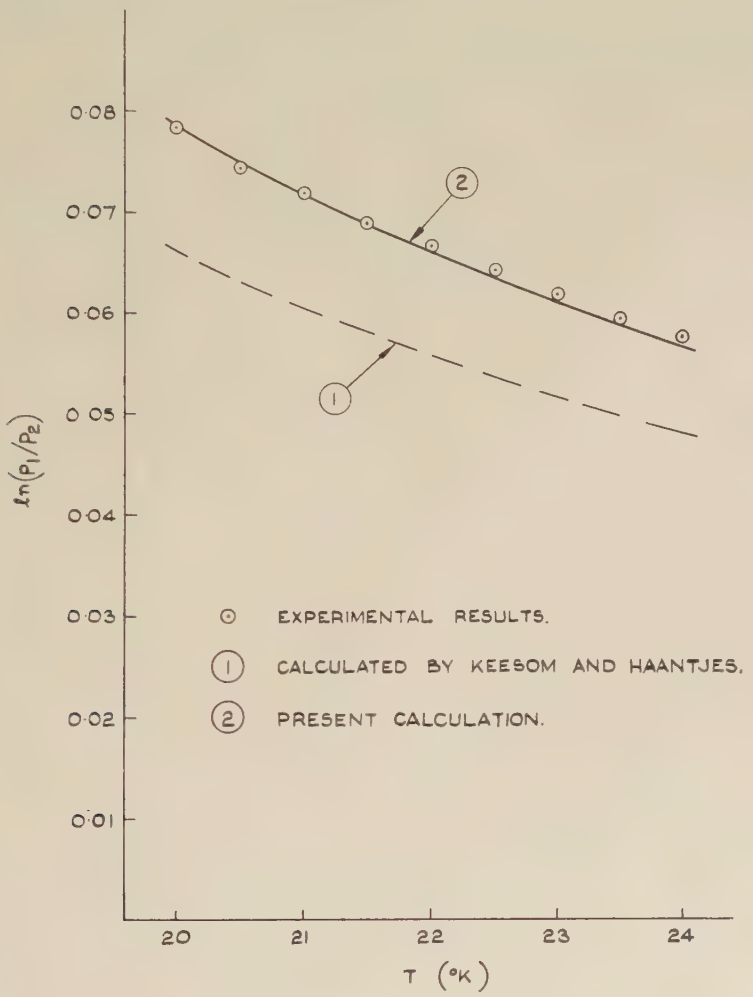

Vapour pressure ratio.

per atom which it would have had if there had been no volume effect, to only $3{\cdot}6 \times 10^{-16}$ ergs per atom, and this compensates for the difference in potential energies. The difference between the free energies of the two isotopes is therefore almost exactly what it would have been in the absence of a ' volume effect '.

It can be seen from fig. 3 that this is the case because the equilibrium condition corresponds to the minimum of the function $f_0=(\frac{1}{2}P_0+\frac{1}{2}3W)$, and this minimum is a rather flat one. This, then, explains why the calculations of Keesom and Haantjes gave reasonable results—there is a considerable difference in the binding energies of the two species, but this has virtually no effect on the vapour pressure ratio. The agreement of the experimental and calculated results of Keesom and Haantjes was by no means perfect, but this was due to the fact that they did not allow for the effects of anharmonicity.

Fig. 2

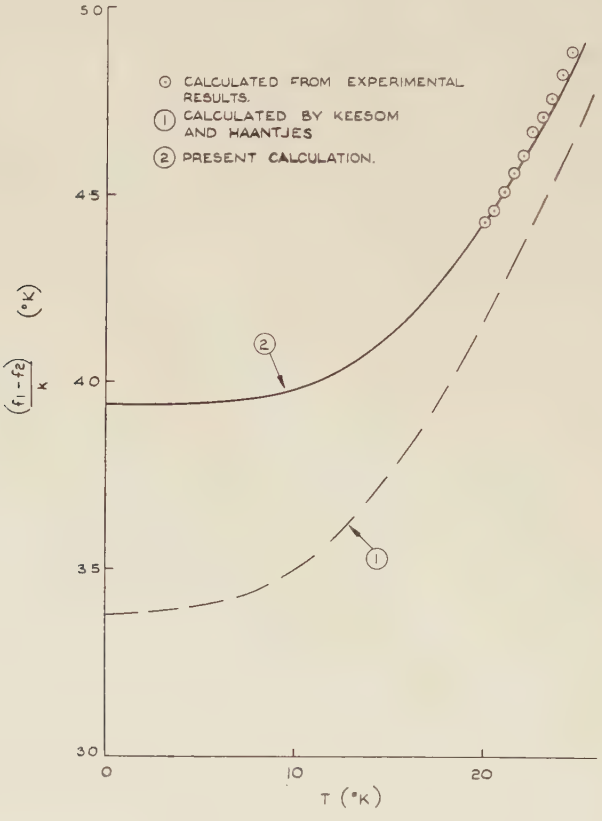

Free energy differences.

The main weakness in the calculation is that it leads to values of the free energy which are lower than the experimental figures. This is presumably due to the fact that an Einstein-type of treatment has been used, rather than one of the type used by Debye. It is, however, at first sight a little surprising that in spite of this the agreement between theory and experiment is so good. The reason seems to be that the

rates of change of the free energy with temperature of (equivalent) functions of the two types are very nearly equal in the temperature range concerned, in spite of the fact that the actual values of the free energy are quite different, and it is the rate of change of the free energy with temperature which is important in determining the vapour pressure ratio. It appears that the calculation leads to values for the characteristic temperature which are slightly too large. This probably does not have much effect on the calculation of the vapour pressure ratio, but it does tend to suggest that the value $n=14$ chosen by Zucker in eqn. (2) is a little too big. The fact that the agreement with experiment is almost perfect is perhaps fortuitous, though it should be noted that no attempt has been made to ' fit ' the results. Zucker's values of A, B and n were used, with the slight modification already noted, which was made at an early stage of the calculation to get a better value for the latent heat.

Fig. 3

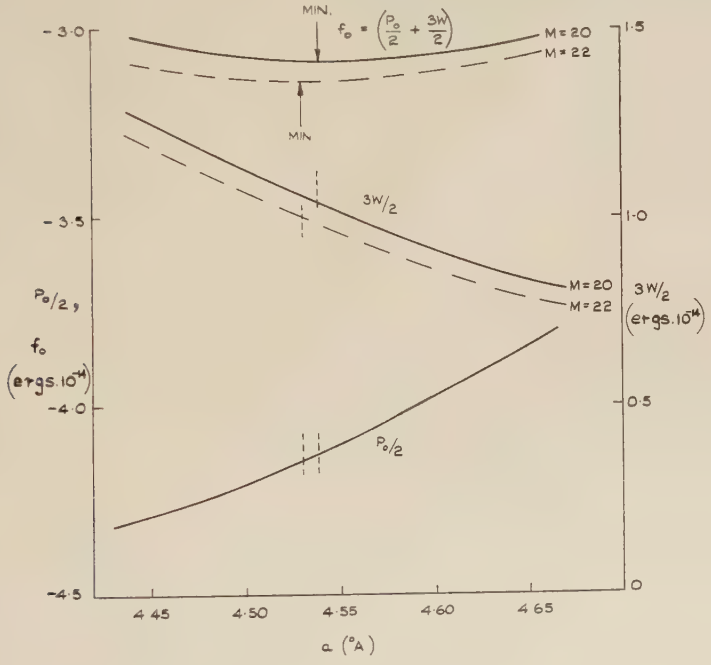

Free energy minima.

It is perhaps worth noting that Henkel's approximate eqns. (25), (27), and (28) were not used, since his expansion of

$$\exp(-n^2 Y/kT)$$

cannot be safely used in the case of neon. Instead, everything was calculated from the original form of his eqn. (21).

§ 4. Conclusion

It appears that Henkel's method can be used with confidence to predict the vapour pressure ratios of the isotopic species of monatomic substances.

Acknowledgments

The author wishes to acknowledge the help given him by the computing group at Harwell, and to record his thanks to Dr. W. M. Lomer and Dr. H. London for commenting on the manuscript of this paper.

References

de Boer, J., 1948, *Physica*, **14**, 139.
Domb, C., and Zucker, I. J., 1956, *Nature, Lond.*, **178**, 484.
Henkel, J. H., 1955, *J. chem. Phys.*, **23**, 681.
Hirschfelder, J. O., Curtiss, C. F., and Bird, R. B., 1954, *Molecular Theory of Gases and Liquids* (New York : John Wiley & Sons), p. 1043.
Keesom, W. H., and Haantjes, J., 1935, *Physica*, **2**, 986.
Lennard-Jones, J. E., and Ingham, A. E., 1925, *Proc. roy. Soc.* A, **107**, 636.
Zucker, I. J., 1956, *J. chem. Phys.*, **25**, 915.

Analysis of Nuclear Interactions of Energies between 1000 and 100 000 BeV†

By B. Edwards, J. Losty, D. H. Perkins, K. Pinkau, and J. Reynolds‡
H. H. Wills Physical Laboratory, University of Bristol

[Received December 1, 1957]

Abstract

Twenty nuclear interactions produced by protons and ten produced by α-particles of energies above 1000 Bev have been analysed.

The proportion of pions amongst the secondaries is found to be 80% for the core and less than 70% for the wide angle tracks. The average transverse momentum resulting from our measurements is $p_T=0{\cdot}5$ Bev/c for pions and $p_T=1$–2 Bev/c for heavy particles. It appears to be independent of angle of emission and primary energy. The multiplicity of the interaction, n_s shows no variation with primary energy; it varies, however, with the anisotropy of the angular distribution, and shows wide fluctuations at a fixed primary energy. The inelasticity, K, of the collisions is close to unity for secondary interactions of mean energy ~100 Bev and about 0·2 for jets produced by protons of energy ~10 000 Bev. At a fixed energy, K does not appear to be strongly dependent on n_s. None of the current theories appears capable of giving a satisfactory explanation of the experimental results, and an alternative model is proposed.

§ 1. Introduction

In a recent publication (Brisbout *et al.* 1956, hereafter referred to as 'A') from this laboratory, experimental results were described relating to the nature of the secondary particles produced in the nuclear interactions, in nuclear emulsions, of cosmic ray primaries of energies exceeding about 1000 Bev nucleon. The present paper contains some additional data regarding the nature of the secondary particles, but is mainly concerned with their distribution in energy and angle of emission, and the comparison of these distributions with the various theories of energetic nucleon–nucleon interactions which have been proposed in recent years.

Table 1 gives a summary of the jet events observed to date in various emulsion stacks exposed by this laboratory.

The scanning procedure employed in the detection of these events has already been described in 'A'. Essentially it depends on observation of cores of electromagnetic cascades created by high energy γ-rays, which are the decay products of neutral pions resulting from the original nuclear interaction.

† Communicated by the Authors.
‡ Now at the University of California, Berkeley.

Table 1

Stack Designation	Volume in litres	Exposure	Number of jets above 10^3 BEV per nucl.	
			α primary	proton primary
G	7·0	6 hr at 83 000′	3	10
E	1·4	6 hr at 105 000′	3	3
I	4·5	6 hr at 108 000′	0	3
M	10·8	8 hr at 117 000′	4	1
P	1·8	6 hr at 104 000′	0	1
J	7·0	180 days at 11 000′	0	2
		TOTAL	10	20

§ 2. PRONG DISTRIBUTION IN JETS

Figure 1 shows the variation of n_s with energy of the incident particle whether of primary or secondary nature. Apparently the multiplicity depends little on the energy.

Fig. 1

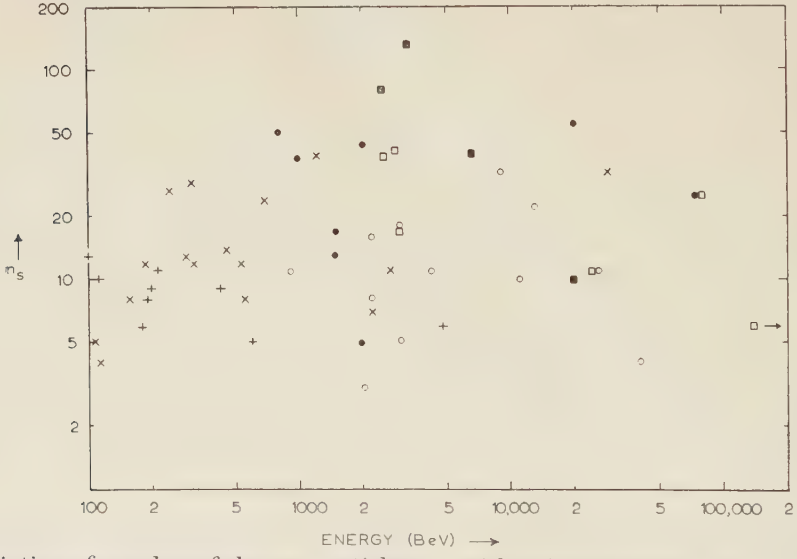

Variation of number of shower particles, n_s, with primary energy, per nucleon.
○ Primary proton jets, $N_h \leqslant 2$; ● Primary proton jets, $N_h > 2$;
□ Primary α-particle jets, $N_h \leqslant 2$; ■ Primary α-particle jets, $N_h > 2$;
+ Secondary jets, $N_h \leqslant 2$; × Secondary jets $N_h > 2$.

Figure 2 (*a*) displays the distribution in the number of heavily-ionizing prongs, N_h, associated with the 30 ‘primary jet’ events. In 11 cases, no heavy prong is observed. In many papers, it has been

assumed that such events represent the collision of a primary particle with either a hydrogen atom in the emulsion, or with a single nucleon on the periphery of a complex nucleus. Since, in our data, such events account for more than one-third of the total, geometrical considerations suggest that most of the events with no associated heavy prongs do in fact result from collisions with nuclei in which more than one, and

Fig. 2

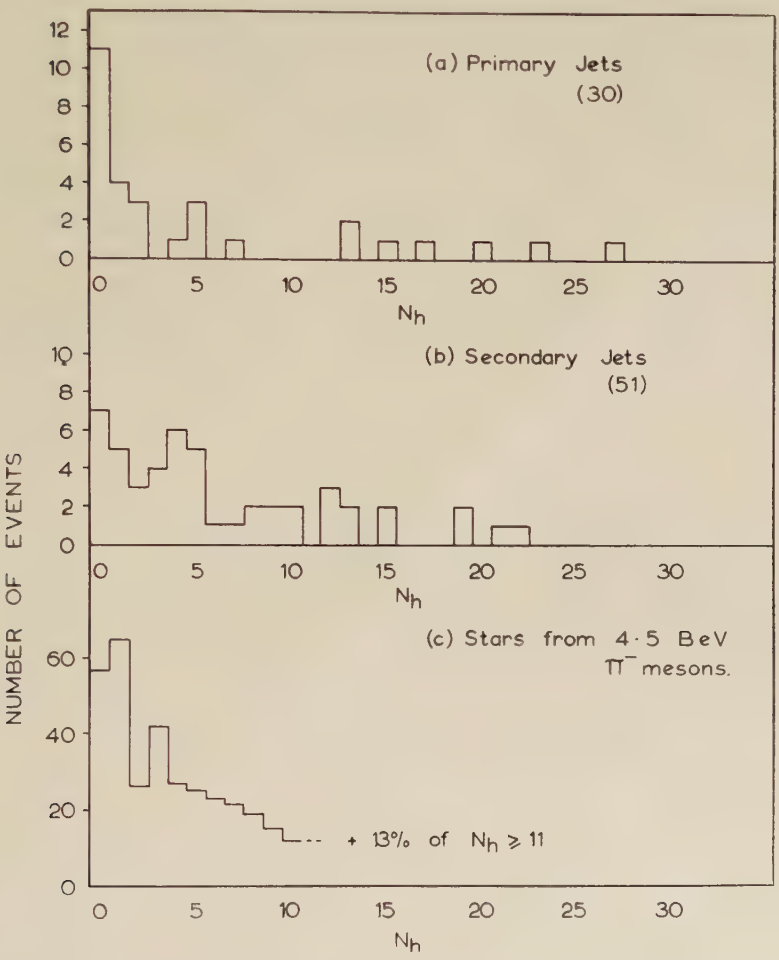

Distribution of the number of heavy prongs, N_h, emitted in (*a*) primary jets, (*b*) secondary jets, and (*c*) stars from 4·5 BEV π^--mesons.

presumably on average two or three, target nucleons lie along the trajectory of the incident particle. The fact that, in these cases. no charged ' evaporation ' particle is emitted, only implies that the excitation energy communicated to the residual nucleus is less than about 50 MEV in the case of collisions with silver and bromine ; and still smaller for the nuclei of the light elements carbon, oxygen and nitrogen.

On the other hand, events of high N_h will correspond to the traversal by the primary of a large amount of nuclear matter. A mixed cascade of nucleons and mesons pervades a large part of the nuclear volume, the number of particles increasing rapidly through the cascade. Experimentally it is found that the number of shower particles in jets of $N_h \geqslant 3$ is about three times that in jets for which $N_h = 0$, 1 or 2 (see fig. 1).

Figure 2 (*b*) shows the distribution in N_h observed for the interactions produced by the secondary particles of the events of fig. 2 (*a*). The mean energy of these secondary jets is known to be of the order of one-tenth of the mean energy of the primary jets, and the smaller proportion (14%) of events of $N_h = 0$ is at once apparent. It is important to emphasize that in the detection of these events there is little bias in favour of high values of N_h, the primary events having been detected by scanning for cascades, and most of the secondary events by following tracks of individual particles. Figure 2 (*c*) shows, for comparison, the N_h distribution for stars produced by 4·5 BeV π -mesons (Edwards *et al.* 1957). In this case, 13% of events have $N_h = 0$. Such a behaviour is to be expected, as has been pointed out by Roesler and McCusker (1953): the increase in divergence of the nuclear cascade, as the primary energy is decreased, will clearly result in a larger number of nucleons of the target nucleus being affected.

§ 3. Nature of the Secondary Particles

3.1. *Measurements in the Inner Cone*

Paper 'A' described statistical methods of determining the constitution of the relativistic particles in the inner cone of jets. One method, which has been widely used, is to compare the relative numbers of charged shower particles and electron pairs. This comparison determines the ratio R of neutral pions to charged particles. In 'A', on the basis of 77 pairs, it was found that $R = 0{\cdot}37 \pm 0{\cdot}04$. The statistical weight of the observations has now been increased, and on the basis of 116 pairs, we find $R = 0{\cdot}40 \pm 0{\cdot}04$. The quantity R may be written:

$$R = \frac{N_{\pi^0}}{(N_{\pi^\pm} + N_{x^\pm})}$$

where x refers to particles other than pions. Assuming $N_{\pi^0}/N_{\pi^\pm} = 0{\cdot}5$, we then have

$$\frac{N_{x^\pm}}{(N_{x^\pm} + N_{\pi^\pm})} = 1 - 2R = 0{\cdot}20 \pm 0{\cdot}07.$$

The statistical weight of the observations is small, but it may be mentioned that if the events are divided into two groups according to multiplicity, we find

$$R(n_s \leqslant 22) = 0{\cdot}59 \pm 0{\cdot}10 \text{ (39 pairs)},$$

$$R(n_s > 22) = 0{\cdot}35 \pm 0{\cdot}04 \text{ (77 pairs)}.$$

These figures suggest, very tentatively, that the proportion of particles x is greatest in events of high multiplicity.

The second method employed in 'A' in investigating the nature of the inner-cone particles, was to compare the number of interactions produced

by neutral and charged secondary particles. On account of their short lifetime, practically all neutral pions will decay before they can interact. Thus, if we assume that neutral and charged particles have the same interaction length in emulsion, the ratio of the number of stars is :

$$Q=\frac{N_{x^0}}{(N_{x^\pm}+N_{\pi^\pm})}$$

where x^0, $x^\pm$, refer to neutral and charged particles other than pions. In ' A ' 9 secondary jets produced by neutral, and 36 by charged particles, were observed, giving $Q=0{\cdot}25\pm0{\cdot}09$. The number of events has now been slightly increased, and the value obtained is $Q=12/48=0{\cdot}25\pm0{\cdot}08$. From these data, the ratio

$$\frac{N_{x^0}}{N_{x^\pm}}=\frac{Q}{(1-2R)}=1{\cdot}25\pm0{\cdot}5$$

is obtained.

The proportion of non-pions among all secondaries, charged or neutral, is

$$W=\frac{N_{x^0}+N_{x^\pm}}{(N_{x^0}+N_{x^\pm}+N_{\pi^0}+N_{\pi^\pm})}=1-\frac{3R}{(Q+R+1)}=0{\cdot}27\pm0{\cdot}08.$$

It is reasonable to assume that many of the particles x will be nucleons projected from the target nucleus.

3.2. *Measurements in the Outer Cone*

The above analysis refers to particles in the core of the jet, i.e. those projected forwards in the assumed centre-of-momentum system. In paper ' A ', attempts were also made to obtain information regarding the flux of strange particles among those emitted at wide angles, by examination of the nuclear interactions which they produced. The number of identified strange particles in secondary interactions was, however, too small for any definite conclusions to be drawn, regarding the frequency of such particles in the original jets.

In the present analysis, attempts have been made to determine the masses of the particles emitted at wide angles, directly, by simultaneous measurements of grain density and scattering as described by Daniel *et al.* (1952). Making use of the ' trough ' in the curve of grain density versus energy, it is possible to differentiate between π-mesons and heavier particles for energies up to 6 Bev. Observations were restricted to a single stack in which the spurious scattering was sufficiently low that significant scattering measurements could be made. It is important to emphasize that in the jet events, the magnitude of the spurious scattering can be estimated in the vicinity of the tracks under consideration, by observations on the very energetic particles in the core.

Selection of tracks was first on the basis of length per emulsion, which was required to be at least 1 cm ; and secondly on the value of $p\beta$, which was required to be between 100 Mev/c–10 Bev/c. The normalized blob densities of the tracks thus selected were determined with a statistical error of less than 2%. The data were obtained from three jets produced

by α-particles, types $2+39\alpha$, $15+123\alpha$ and $1+41\alpha$; one induced by a neutral particle, type $4+11$n and two by protons, types $0+18$p and $0+16$p. All the primary energies were in the interval 1000–3000 Bev/nucleon.

Twenty-six tracks were found satisfying the above criteria, and the results are plotted in fig. 3. The curves in this diagram are those obtained in independent measurements on shower particles from interactions produced by 4·5 Bev π-mesons, and are in fair agreement with those of Daniel *et al.* (1952).

Fig. 3

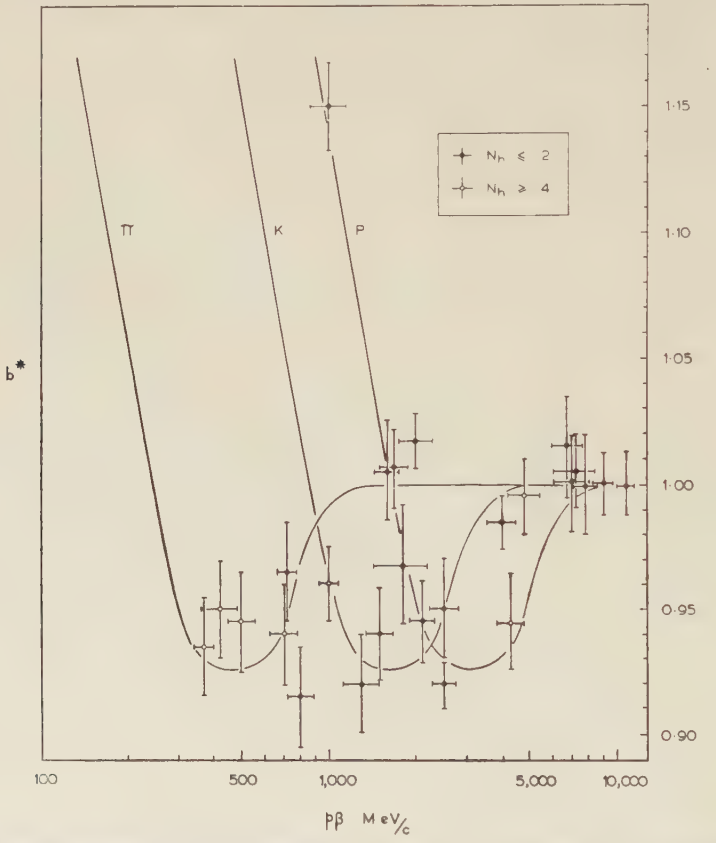

Plot of measurements of blob density, b^*, and the values of $p\beta$, obtained on tracks in the outer cone.

For energies below 6 Bev, where discrimination is possible, seven points out of a total of twenty lie at least two standard deviations (in both $p\beta c$ and b^*) from the accepted curve for pions. The proportion of protons and/or K-particles among the shower particles is therefore at least 30%, and may be considerably greater. All the above seven tracks have been followed, and two of them interact before leaving the stack. There is no indication from these interactions that either of the particles is an anti-proton.

In a collision system in which equal numbers of particles are emitted symmetrically backwards and forwards one would expect the proportion of particles which are not pions to be about the same in both backward and forward hemispheres; in fact, however, the proportion of the heavy particles at wide angles appears to be somewhat greater than that in the core. However, it should be emphasized, that the events in which scattering measurements were made have a higher than average multiplicity and secondary interactions may thus have contributed to a high proportion of heavy particles; as we have seen, in such events, the value of R in the core is somewhat less than for events of low multiplicity.

§ 4. Energy and Transverse Momentum of Secondary Charged Particles

As a general rule, a complete analysis of individual jet events (involving the estimation of the energies of all secondary particles) is impracticable. Usually the energies of only one or two particles in each event can be determined, and it is desirable, in collecting results from a large number of events, to choose, to represent the data, some parameter which varies as little as possible from one event to another. The transverse momentum p_T of the secondary particles, turns out to be such a parameter, and it has the additional advantage of being Lorentz invariant. Furthermore, if the created particles are emitted equally backwards and forwards from a single collision system, considerations of symmetry suggest that p_T should be the same for both forward and backward particles.

Table 2

Type of secondary interaction	Primary energy estimated from angular distribution of shower particles (BeV)	Primary energy estimated by relative scattering (BeV)
1+ 9p	420±140	220±80
0+ 6p	31± 13	22± 5
12+ 5p	110± 50	120±40
0+13p	90± 20	80±20

A determination of p_T obviously necessitates measurements of both the energy, and angle of emission relative to the primary direction of a secondary particle. In the case of the relatively low energy particles (at wide angles), the energies may be estimated by observation of Coulomb scattering along the tracks, as described in the preceding section. If the tracks are steep, the ' surface-angle ' or ' glass coordinate ' method (Barkas *et al.* 1957) can be employed up to energies ~2 BeV.

In general, the energies of particles in the core cannot be estimated by scattering measurements, since they are typically of the order of a 100 BeV.

In exceptional cases, where three or more secondaries occur with extremely small separations in azimuth and dip, relative scattering measurements, over distances ~ 10 cm or more, can be made. Usually, however, estimates of the energies of the particles in the core have been based on the angular distribution of the shower-particles in the secondary jets which they produce (see § 6), and to this end, the employment of large stacks of emulsion is clearly advantageous. In four cases only has it been possible to compare the energy estimates by the two methods, and the results obtained are indicated in table 2.

The errors quoted in the second column correspond to a fractional error in primary energy of $1/\sqrt{n_s}$, where n_s is the number of charged shower particles. The agreement between the two sets of measurements is seen to be reasonably good.

As in the case of primary jets (see § 7) only those secondary jets for which $N_h < 13$ were accepted for measurement. This selection was made in order to exclude events (accounting for 16% of the total —see fig. 2 (*b*)) in which large contributions from secondary interactions occurred. A further requirement, made in order to reduce statistical errors in energy determination, was that $n_s \geqslant 4$.

In addition to the energy, the other quantity required in determining p_T is the angle, θ, which the secondary makes with the primary direction. An accurate determination of this angle often presents great difficulties in the case of the innermost tracks of the jet. Even in "flat" events, where both the primary and the secondary particles in the core make very small angles with the plane of the emulsion, it is difficult, especially in the presence of spurious scattering, to determine the projected value of θ in the plane of the emulsion to better than 10^{-4} radians. Uncertainties in determination of dip angles are even greater, limiting the accuracy with which the vertical component of θ can be estimated to about 10^{-3} radians. On the other hand, the *relative* angles of emission of the secondary particles may be determined with very great precision, and in cases where absolute measurements of θ are unreliable, we have taken as the reference track, that secondary which is most nearly coincident with the primary direction.

The difficulties in measuring the angular distributions in secondary jets are not nearly so acute; first of all, because they are usually of much lower energy, and secondly because shower particles adjacent to the secondary which interacts often provide reference tracks.

Figure 4 shows the distribution in p_T obtained for three ranges of primary energy, and it appears that there is no significant variation. Figure 5 displays the results of plotting individual values of p_T against C-system angle of emission, $\bar{\theta}$. There is apparently a small increase of the mean value of p_T with decreasing $\bar{\theta}$. The effect is probably not genuine, and is most likely due to the fact that for particles emitted at small $\bar{\theta}$, energies have been estimated predominantly from the angular distribution of shower particles in secondary disintegrations, whereas the energies of particles emitted at large $\bar{\theta}$ are generally sufficiently small to allow

estimation by scattering methods. The errors associated with the former method can lead to over-estimation of the energy, whereas this is not the case for scattering measurements; indeed, tracks associated with exceptionally high values of p_T will be excluded, since the corresponding scattering measurements might have to be rejected as not significant. Depending on the length per emulsion of each track, and magnitude of spurious scattering in its neighbourhood, we have estimated the maximum

Fig. 4

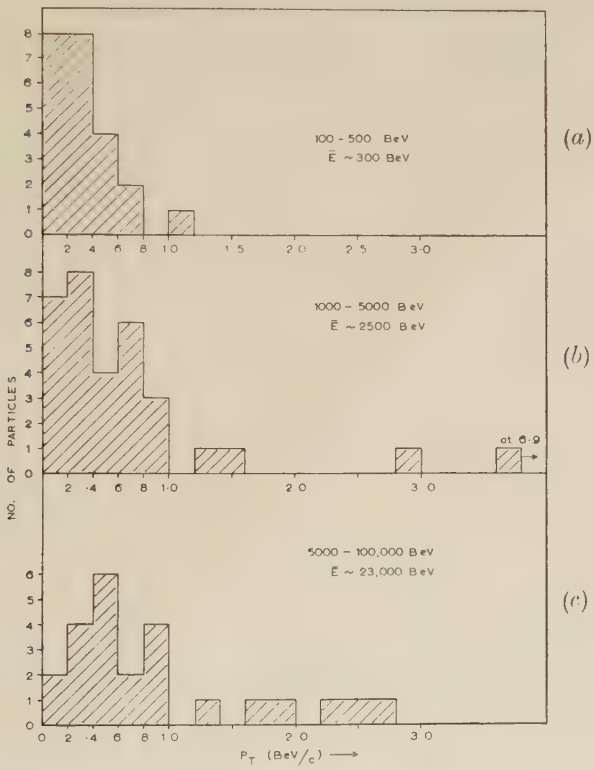

Distribution of transverse momentum, p_T, for three ranges of primary energy. Figure 4 (*a*) consists of (i) the results of Daniel *et al.* (1952), and (ii) scattering measurements on tracks in secondary jets.

value of $p\beta$, and hence p_T, which could have been reliably measured. In this way, it is found that a value of $p_T = 0{\cdot}5$ BeV/c could have been measured in 80% of the cases, of $p_T = 1{\cdot}0$ BeV/c in 60% of the cases, and of $p_T = 2{\cdot}0$ BeV/c in only 30% of the cases. The bias in favour of small values of p_T is therefore considerable. The distributions in p_T obtained by the different types of measurement are shown in fig. 6.

Most of the values in the above measurements refer to pions, but it would be of great interest to determine separately values of p_T for particles other than pions. In fig. 6 (*c*), the values obtained from the interactions produced by neutral secondaries (some of which will be neutrons), are shown separately. The number of such events is at present very small, but they appear to indicate that the average value of p_T may be somewhat higher than for the charged particles.

Fig. 5

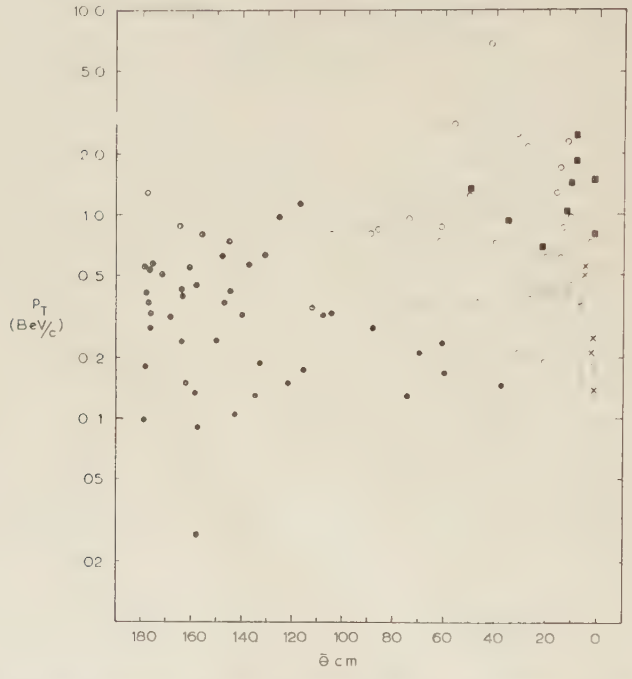

Plot of transverse momentum, p_T, versus angle of emission in the centre-of-momentum system, $\bar{\theta}$. The energies have been determined by several methods :

● Scattering measurements ; ○ Angular distribution of secondary jets produced by charged particles ; ■ Angular distribution of secondary jets produced by neutral particles ; × Angle of divergence of photons from π^0-mesons.

As shown in § 3, about one-quarter of the charged particles in the cores of jets are not π-mesons. If we subtract, out of the total of 36 events in fig. 6 (*b*), the nine events with the highest values of p_T, the mean value of p_T is in good agreement with that obtained for π^0-mesons in the core (see table 3).

In addition to the observations on the ' primary ' jets, some measurements have also been made on the transverse momenta of the shower particles from ' secondary ' jets. The distribution is given in fig. 4 (*a*), which includes also the earlier results of Daniel *et al.* (1952).

Table 3

	Scattering measurements	Angular distribution of secondary jets produced by :			Electron pairs
		(*a*) Charged particles		(*b*) Neutral particles	
		Total	Less nine highest values		
No. of events	43	36	27	9	80
Mean p_T (Bev/c)	$0{\cdot}41 \pm 0{\cdot}13$	$0{\cdot}8 \pm 0{\cdot}1$	$0{\cdot}5 \pm 0{\cdot}1$	$1{\cdot}4 \pm 0{\cdot}2$	$0{\cdot}26 \pm 0{\cdot}08$ ($0{\cdot}52 \pm 0{\cdot}16$ for π^0)

Fig. 6

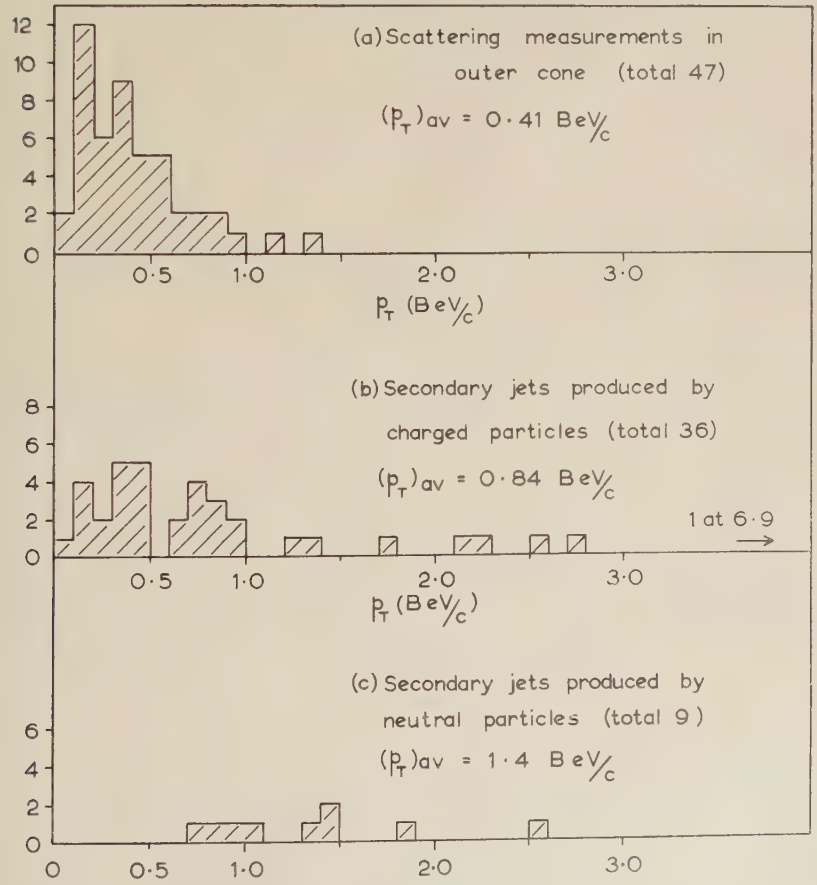

Distribution in transverse momentum, p_T, obtained in different types of measurement.

§ 5. Energy and Transverse Momentum of Secondary Photons

In addition to that deduced from observations on the nuclear-active secondaries of the jets, useful information regarding the distribution of p_T can be obtained from measurements of the energies and directions of emission of the photons assumed to result from the decay of neutral pions. Whilst the method is not so direct, it has the advantage that energy estimates can be made on a much greater proportion of the electron pairs than is possible for the nuclear-active particles. However, the observations (see § 3) are restricted to the core of the jets, since the detection of electron pairs resulting from the conversion of photons emitted at wide angles to the primary direction is extremely arduous.

The measurement of the energies of pairs, and of the parent π^0-mesons, may be achieved by several methods. The most widely used method has been the measurement of either relative scattering or individual scattering of the electrons of a pair. For electron pairs in the core, relative scattering is almost an order of magnitude greater than that of a pair of shower particles in the same region, and can thus often be measured. For photons of a given energy, the relative scattering between the electrons into which they convert will depend on the disparity in each case, and will therefore fluctuate widely. In the present work, we have calculated the average value, α_{av}, of the relative scattering of the electrons of a pair, compared with that obtaining when both particles have equal energy, say α_0. For a flat disparity distribution, a value of $\alpha_{av}/\alpha_0=4$ was calculated. In arriving at this estimate, it has been assumed that individual values of disparity exceeding 100 would be detectable by inspection, and rejected. An experimental check of the above value was obtained on several pairs which provided sufficiently good conditions for accurate measurement of 'single' as well as relative scattering, and a ratio of $4\pm1{\cdot}5$ was obtained.

The second approach employed in determining pair energies has been to measure the total energy in the ensuing soft cascade, from the lateral spread (Pinkau 1957). This method is applicable chiefly to pairs of energy exceeding 50 Bev. When necessary, backgound corrections have been made to take account of stray tracks from secondary nuclear interactions, and neighbouring cascades.

In events of very low multiplicity, it is often possible to correlate pairs of photons resulting from the decay of individual neutral pions. These cases, whilst few in number, serve as a valuable check on the other methods of energy estimation. If the kinetic energy of a neutral pion, in terms of its rest energy, is γ, then the angle ϵ between the pair of photons is

$$\epsilon=\frac{1}{\gamma}\left(\sqrt{D}+\frac{1}{\sqrt{D}}\right)$$

where D is the ratio of the energies of the two photons. Even for a large value of D, say 16, the value of ϵ is only twice that for equipartition, so that only a rough measure of D is necessary to determine γ. A few values of transverse momentum of neutral pions, deduced in this manner, are included in fig. 5.

Figure 7 shows values of p_T of electron pairs, plotted against the C-system angle of emission $\bar{\theta}$ (assuming that the photons originated directly from the jet, rather than by decay of the short-lived neutral pion). Again, p_T appears to vary little with $\bar{\theta}$.

Fig. 7

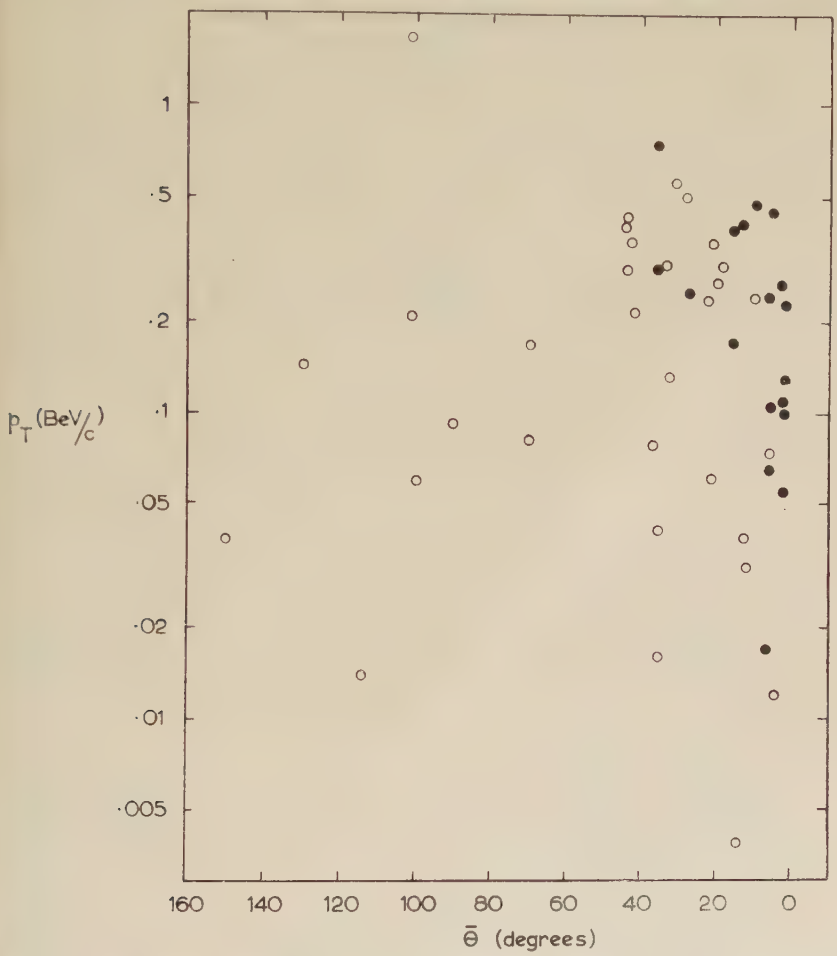

Plot of transverse momentum, p_T, of electron pairs in proton induced jets versus their space angle with respect to the primary direction, $\bar{\theta}$. The energy has been determined by two methods: ○ relative scattering measurements on electron pairs; ● measurement of the cascade development.

Figure 8 displays the distribution in p_T observed for all the pairs examined. One can compare the distribution in fig. 8 with that in fig. 6 in the following way. In fig. 6, only 3% of the individual values of p_T are below 100 MeV/c, and the average value of p_T is large compared with the maximum transverse momentum of the photons relative to the parent π^0-particle (70 MeV/c). Let us therefore assume that the transverse

momentum of the photons relative to the neutral pion is negligible compared with that of the neutral pion, p_T^1, relative to the primary of the jet. For a neutral pion of high energy the energy distribution of the photons into which it decays will be flat, extending from E down to nearly zero energy. Thus, the transverse momentum distribution of the photons will also extend from p_T^1 to zero. Assuming the

Fig. 8

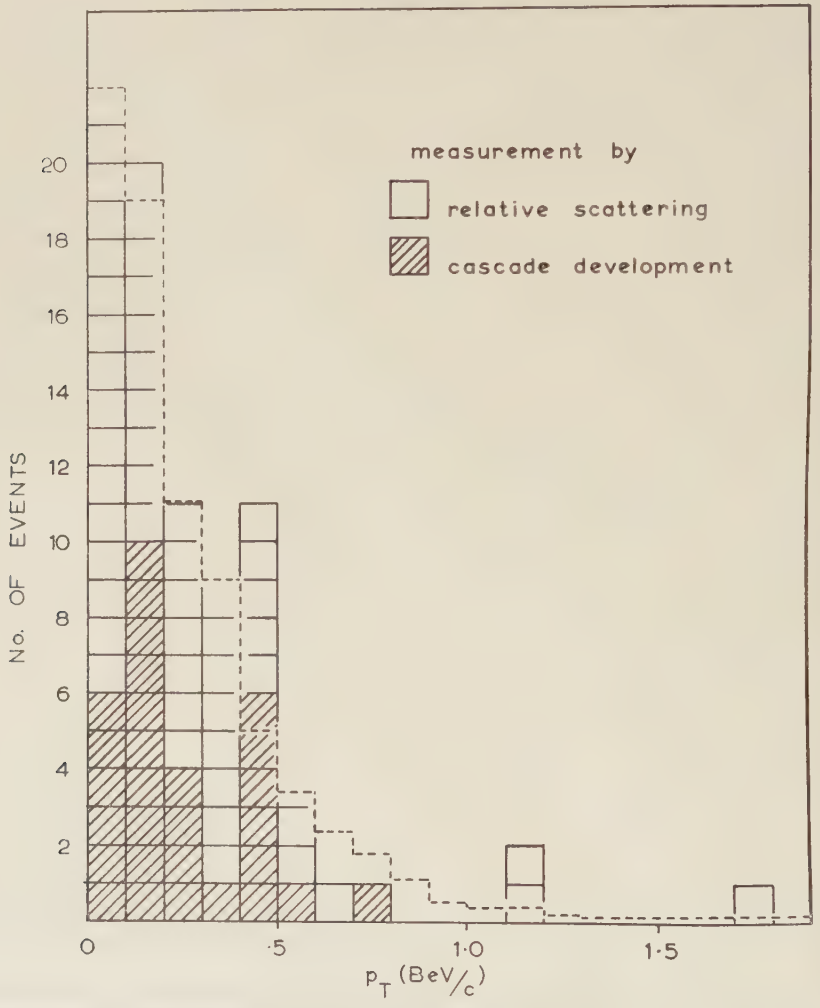

Distribution in transverse momentum for the electron pairs. The dashed line is what would be expected if the combined distributions of fig. 6 (*a*) and 6 (*b*) were also representative for the π^0-mesons.

combined distribution of figs. 6 (*a*) and 6 (*b*) to be representative of that of the neutral pions, one can therefore compute that to be expected for the photons, and in this way the broken histogram in fig. 8 is obtained. The agreement between the two histograms is reasonably good.

From the foregoing discussion, it will be clear that the average transverse momentum of the neutral pions will be just twice that for the photons, and is thus found to be $0{\cdot}52\pm0{\cdot}16$ BeV/c. This value is in fair agreement with the independent measurements of the Japanese emulsion group (report by Oda 1957). We regard the above mean value of p_T as the most reliable figure for pions, charged or neutral. The average values of p_T found by the various methods described in §§ 4 and 5 are collected in table 3.

§ 6. Determination of Primary Energy of Jets

Let θ be the angle of emission, relative to the primary direction, of a secondary particle, β_s its velocity in terms of that of light, and

$$\gamma_s=1/\sqrt{(1-\beta_s^2)},$$

all measured in the L-system. Bars denote corresponding quantities in the C-system, the velocity of which in the L-system is denoted by β_c, γ_c. Then

$$\gamma_c \tan\theta=\frac{\sin\bar{\theta}}{[(\beta_c/\bar{\beta}_s)+\cos\bar{\theta}]}. \qquad (1)$$

If two particles are emitted symmetrically forwards and backwards in the C-system (i.e. at $\bar{\theta}$ and $\pi-\bar{\theta}$), the L-system angles will be θ_f and θ_b respectively where

$$\gamma_c^2 \tan\theta_f \tan\theta_b=\frac{\sin^2\bar{\theta}}{[(\beta_c/\bar{\beta}_s)^2-\cos^2\bar{\theta}]}. \qquad (2)$$

If $\beta_c/\bar{\beta}_s\simeq1$, and $\bar{\theta}$ is not too small, then the right-hand side of the above equation is close to unity. Thus, if there is backward–forward symmetry in the C-system, in the nomenclature of Castagnoli *et al.* (1953),

$$-\log\gamma_c=\frac{1}{n_s}\sum_{i=1}^{i=n_s}\log\tan\theta_i.$$

In the present work, we have found that it is advantageous to be able to display the angular distribution graphically, in the following manner. When $\bar{\theta}=90°$, let $\theta=\eta$, the median angle. For the approximation $\beta_c/\bar{\beta}_s=1$, we have:

$$\gamma_c \tan\theta_f=\frac{\tan\bar{\theta}_f}{\tan\eta}=\tan\tfrac{1}{2}\bar{\theta};$$

$$\frac{\tan\theta_b}{\tan\eta}=\cot\tfrac{1}{2}\bar{\theta}=\frac{1}{\tan\theta_f/\tan\eta}. \qquad (3)$$

Thus, if we plot the values of $\tan\theta$ on a logarithmic scale, $\tan\eta$ corresponds to the centre of gravity of the distribution: further, the displacement of any particular track on this scale is

$$\log(\tan\theta/\tan\eta)=\pm\log\cot\tfrac{1}{2}\bar{\theta},$$

so that for the case of symmetrical emission from the C-system, the values of $\tan\theta$ transform to a distribution symmetrical about the point $\tan\eta$ – see examples in fig. 9. An important advantage of this graphical plot lies

in the fact that the structure of the C-system angular distribution is at once apparent.

The approximation, $\beta_c/\bar{\beta}_s = 1$, made above, whilst adequate for not too large values of $\bar{\theta}$, may be seriously questioned for particles travelling backwards at very small angles $\bar{\theta}' = (\pi - \bar{\theta})$, for then we are interested in the difference $(\beta_c/\bar{\beta}_s - \cos\bar{\theta}')$, both terms being of the order of unity. We may make use here of the empirical fact that p_T is independent of $\bar{\theta}'$, and it may be shown that, for small values of $\bar{\theta}'$, of the order of η,

$$\frac{\tan\theta_b}{\tan\eta} \simeq \cot\tfrac{1}{2}\theta' \left[\frac{1}{1+M^2(1-\alpha^2)/p_T^2}\right] \quad . \quad . \quad . \quad . \quad (4)$$

where M is the mass of the secondary particle, in terms of the nucleon rest-mass, p_T is measured in the same units, and α is the ratio $\bar{\gamma}_s/\gamma_c$.

For pions, α will be of the order of unity or less, and, on average, $M^2/p_T^2 \simeq 0{\cdot}1$, so that the error involved in the approximate formula (3) is only of the order of 10%. Only for about 9% of the pions is $p_T < M$, and hence the error as high as a factor 2. The case for secondary nucleons is not so clear. First of all, the appropriate value of p_T is not well known, but the limited statistics suggest that it may be of the order of 1–2 Bev/c (fig. 6 (*c*)). Thus, M/p_T is most likely of the order of unity. α clearly must be less than unity—the evidence from extensive air showers suggesting an average value of α exceeding 0·7, i.e. $(1-\alpha^2) < 0{\cdot}5$. One can conclude that eqn. (3), when applied to the emergent nucleons travelling at very small backward angles, will lead to errors in C-system angle in general not exceeding a factor 2, and in many cases much less.

To summarize, large errors will be introduced by using the approximate transformation (3) only when abnormally low values of p_T, combined with C-system angles of emission $\bar{\theta}' \leqslant \eta$, occur. In practice, such a combination appears to be rare, and the average error in the estimate of primary energy, introduced by the assumption $\beta_c/\bar{\beta}_s = 1$, is extremely small.

It sometimes happens, particularly in events of low multiplicity, that the number of charged secondary particles, emitted backwards in the C-system appears to differ considerably from the number emitted forwards. This is to be expected, purely on the basis of statistical fluctuations in the ratio of neutral and charged particles. Event P20, of fig. 9 is a clear case, where 3 charged particles are projected backwards, and one forwards. As stated above, in such events (P20, Chicago S-event; Glasser *et al.* 1955), where the distinction between forward and backward particles is fairly clear, the primary energy has been estimated by finding the mean of $\log\tan\theta$ for the forward and backward tracks, separately, and taking the average:

$$-\log\gamma_c = \tfrac{1}{2}[1/n_f \sum \log\tan\theta_f + 1/n_b \sum \log\tan\theta_b].$$

This procedure fails, if by chance only one or two, or perhaps no charged particles are projected into one or other hemisphere. (Event P20 is exceptional since, in addition to one charged particle, 2 neutral pions

travel forwards). If no neutral pions are projected forwards, the event would not usually be detected. We are therefore more concerned with events in which few or no charged particles travel backwards (P24 and P15). It will be noticed, in fig. 9 that, where backward particles in low-multiplicity, high-energy events *do* occur (P20, P20s4), they are emitted mostly at wide angles, tan $\theta_b \sim 0{\cdot}3$ -1·0. In events P15 and P24 where only two out of the eleven shower particles travel backwards, it has been assumed that $\overline{\tan \theta_b} = 0{\cdot}3$.

Fig. 9

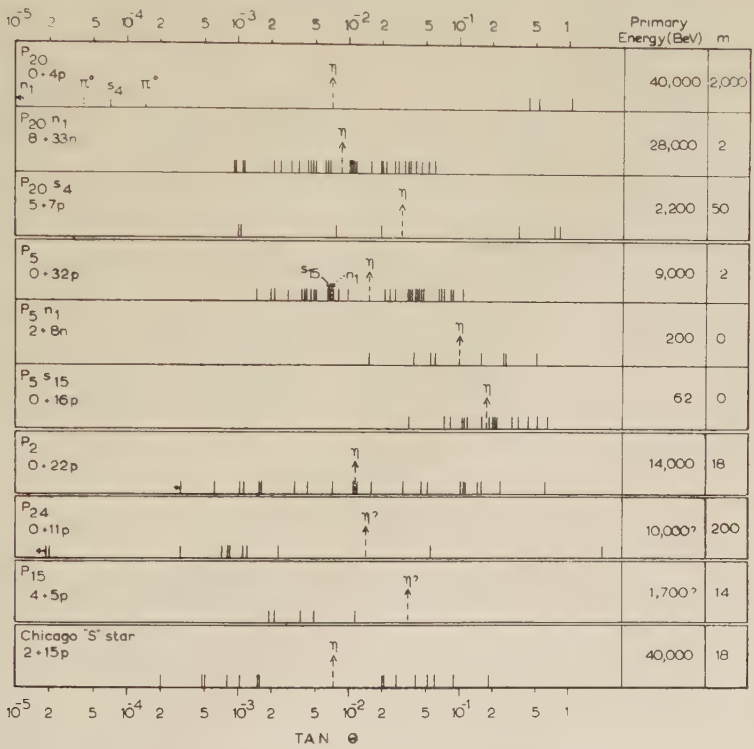

Plots of log tan θ for a representative sample of primary and secondary jets.

In the events shown in fig. 9, the points indicating tracks at very small values of θ sometimes have an arrow showing that the angle quoted is only an upper limit, and that this particular track has been taken as the reference from which to measure the angles of the remaining tracks. In determining the primary energy in these cases, this reference track has been ignored, together with that track emitted at the largest laboratory angle. If symmetry holds in the C-system, this procedure should lead to the correct value of the primary energy as determined on the remaining (n-2) tracks in the event.

It must be emphasized that the foregoing analysis has been based on the assumption that, in the collision of a nucleon with a nucleus, symmetrical or nearly symmetrical emission of secondary particles takes place,

in what is effectively a single collision system. Further, that if γ_c is the value of γ for the centre-of-momentum system, the total energy in this system is $2\gamma_c$ (in Bev), and that the primary energy in Bev is $\gamma_p = 2\ \gamma_c^2$. As described above, most of the secondary particles of the jets are pions, and the energies of these have frequently been estimated from the foregoing analysis applied to the secondary jets which they produce. In particular the connection between γ_c and C- and L-system energies are assumed to be the same as for the case of an incident nucleon. These assumptions are further examined in the discussion of the results; however, the ultimate justification for them comes not from theoretical considerations, but must be found in the internal consistency of the results which follow from them.

An experimental check of the validity of the above hypothesis, for nucleon–nucleus collisions, could in principle be made by a comparison of the jets resulting from interactions of a beam of nucleons forming the fragmentation products of very heavy primary nuclei, the mean energies of the nucleons being determined independently from their angular spread. So far, however, no collisions of heavy primary nuclei of sufficiently great energy have been observed in this laboratory. As far as the interactions of secondary particles are concerned, the values of p_T deduced from such an analysis, are, as we have seen, in fair agreement with those deduced by independent methods, such as Coulomb scattering along tracks in the outer cone, and measurements of the energies of photons arising from decay of the neutral pions.

§ 7. Angular Distribution of Secondary Particles

The angles of emission, $\bar{\theta}$, of the secondary particles in the C-system, can be obtained from the displacement of each point from the centre of gravity of the laboratory angular distribution shown in fig. 9. This displacement is equal to $\log \cot \frac{1}{2}\bar{\theta}$—see eqn. (3). The exact form of the angular distribution is unknown; for example, it may be represented by the expression $\cos^m\bar{\theta}\ \mathrm{d}(\cos\bar{\theta})$, with m even. A convenient parameter specifying the degree of anisotropy is $(\mathrm{cosec}\,\bar{\theta})_{\mathrm{av}}$, which for the above distribution is

$$(\mathrm{cosec}\,\bar{\theta})_{\mathrm{av}} = \frac{\pi \lfloor (m+1)}{2^{m+1}\,(\lfloor \frac{1}{2}m)^2}$$

$$\simeq (m+1)\sqrt{\frac{\pi}{2m}} \simeq 1{\cdot}25\sqrt{m}\ \text{(for large } m\text{)}.$$

In fig. 9, the values of m, computed from the above equation are shown in the right-hand margin. It will be seen that, even over a small range of primary energy, the values of m fluctuate widely. There appears to be a strong dependence of m upon n_s. In fig. 10, the mean value of cosec $\bar{\theta}$ is plotted versus γ_c/n_s, a quantity proportional to the energy available per shower particle in the C-system. It will be observed that $(\mathrm{cosec}\,\bar{\theta})_{\mathrm{av}}$

increases with increasing γ_c/n_s. Thus, events of low multiplicity will have high m-values and strongly-peaked angular distributions, whereas those of high n_s will be much more isotropic. This effect is well illustrated by event P20, for which $n_s=4$, and $m=2000$, and the secondary jet P20 nl, of comparable energy, with $n_s=33$, and $m=2$.

Fig. 10

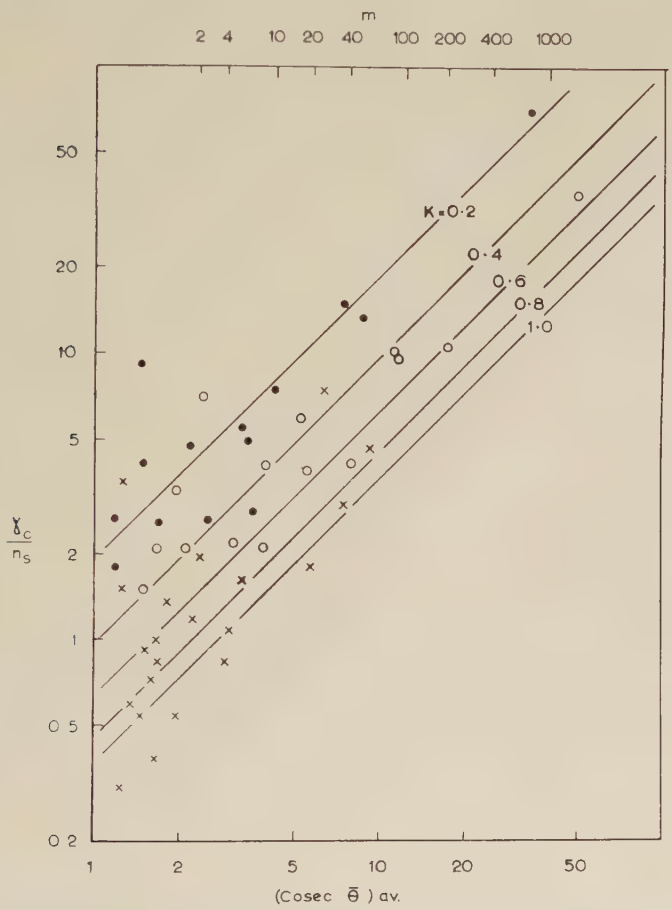

Plot of $(\text{cosec}\,\bar{\theta})_{\text{av}}$ *vs* γ_c/n_s for primary and secondary jets: ○ Primary jets, assuming all secondaries to be pions; ● Primary jets, assuming only 80% of the shower particles to be pions; × Secondary jets, all shower particles are assumed to be pions.

The striking feature about the interaction P20 nl, and indeed many events of high multiplicity, which we have observed, is the absence of particles both at very small *and* very large angles in the L-system. If an event such as P20 were ascribed to a single nucleon–nucleon collision, event P20 nl cannot be regarded as a succession of elementary collisions (cascading in the nucleus) of type P20, since the presence of tracks at

large angles should still be observed. There appears to be an underlying difference in the two types of collision, possibly in the effective impact parameter. This point is further discussed in § 10.

When the individual values of $z = 1/\sin\bar{\theta}$ from all events are collected together, the integral distribution in z over 250 particles is accurately represented by the relation $N(>z) = \text{const.}\ z^{-1}$ over the range $50 > z > 1$. This implies that the differential momentum spectrum of the mesons, averaged over all the events, and under the assumption $p_T = \text{const.}$, is of the form dp/p^2, as assumed by Heisenberg (1952).

§ 8. Inelasticity of the Collisions

Perhaps the most important quantity of interest, in the study of high energy interactions, is the inelasticity, K, of the collision. K is defined as the fraction of the total available kinetic energy of the colliding particles, before the collision, which is subsequently radiated in the form of newly created particles (measured in the centre-of-momentum system). In what follows, since the nature of the heavy particles x is unknown, the value of K will refer to π-mesons only.

A simple, approximate, method of determining the amount of energy radiated in a collision, is to make use of the principle that p_T is invariant with respect to the angle of emission. If all secondary particles were emitted with a constant and known value of p_T, measurement of their angular distribution would yield the total energy. In practice, since the distribution in p_T is a wide one, the information obtained will be of a statistical nature.

The analysis has been carried out in the C-system. This has the advantage that about half the total energy is carried away by the particles travelling backwards, which are emitted at fairly large and accurately measurable angles in the L-system. Moreover, for those particles emitted backwards at small angles $\bar{\theta}'$, with energies $\bar{E}_s$, the ratio $\bar{E}_s/\gamma_c$ is almost independent of errors in estimating primary energies, for :

$$\frac{\bar{E}_s}{\gamma_c} \simeq \frac{p_T}{\gamma_c \sin\bar{\theta}'} \simeq \frac{p_T}{2\gamma_c} \cot \tfrac{1}{2}\bar{\theta}' \simeq \tfrac{1}{2} p_T \tan\theta_b$$

from eqn. (3).

On the other hand, especially in the case of primary jets, the angle of emission of that secondary particle closest to the primary direction cannot always be measured with great accuracy in the L-system ; in some events even, only an upper limit can be given. It is, however, possible to compare the value of $\bar{\theta}$, for that particle travelling at the smallest forward angle, with that of the particle travelling at the smallest backward angle, in order to check that large errors have not occurred in the former. In all cases examined, the two were equal within a factor 2 in either direction. In cases where the smallest forward angle could not be measured at all (shown by arrows in fig. 9), it was assumed to be equal to the smallest backward angle.

8.1. *Energy Balance in Interactions of Secondary Particles*

Such an analysis has first of all been made of the 'secondary jets', with energies typically of a few hundred BEV. As mentioned before, an arbitrary selection $N_h<13$, corresponding to 84% of all the events, was made. Most of the secondary jets are known to be produced by pions, and in order to exclude nucleon primaries as far as possible secondary jets produced by neutral particles were omitted from the analysis.

Our experimental material regarding the transverse momentum of the particles produced in secondary jets is at present rather meagre (fig. 4 (*a*)). p_T was therefore assumed to have the same average value as that of the pions in the primary jets, i.e. 0·5 BEV/c. Allowing a factor 1·5 to account for the neutral pions, we have defined a quantity K' from the formula

$$K'=\frac{1{\cdot}5p_T \sum \operatorname{cosec}\bar{\theta}}{2\gamma_c}. \qquad (5)$$

The numerator in eqn. (5) equals the sum of the momenta, without regard to sign, of the secondary particles, in BEV/c, which to sufficient accuracy for our purpose is also their energy in BEV. The denominator, $2\gamma_c$, will be the total energy in BEV in the C-system, assuming the collision to occur with a single target nucleon.

The distribution in K' observed is shown in fig. 11 (*a*), and a mean value of $0{\cdot}83\pm0{\cdot}18$ obtained. The fluctuations about the mean will presumably arise from (*a*) fluctuations in the ratio of neutral and charged secondary particles, (*b*) errors in estimating γ_c from the angular distribution, and (*c*) fluctuations in values of p_T about the assumed average of 0·5 BEV/c.

If all the secondary particles in these events were pions, then K' should on average be unity. If nucleons are also present, then the apparently higher values of p_T of these particles would lead to a value of $K'<1$. The fact that the observed value of K' is close to unity may be taken to indicate that, in pion–nucleon collisions at these energies (typically one or two hundred BEV), only a small fraction of the incident energy is carried off by nucleons.

It is of interest to note that if K' is evaluated in the L-system in the case of secondary jets, the mean value becomes $1{\cdot}0\pm0{\cdot}2$. This suggests that the nucleons in the secondary jets travel mainly in the backward direction in the C-system, since these tracks get equal weight with the forward tracks when the calculation is done in the C-system, while their influence on the value of K' is negligible for computations in the L-system.

It follows, from eqn. (5), that

$$(\operatorname{cosec}\bar{\theta})_{\mathrm{av}}=\frac{4K'}{3p_T}\left(\frac{\gamma_c}{n_s}\right),$$

so that, for fixed values of p_T and K', the relation between $(\operatorname{cosec}\bar{\theta})_{\mathrm{av}}$ and γ_c/n_s is linear. This alternative method of displaying the results is shown in fig. 10.

8.2. *Energy Balance in Primary Jets*

Using the same method as employed for the secondary jets, we have calculated K' for the primary proton-induced jets, again with the restriction $N_h < 13$. First of all, let us make the fallacious assumption that all the

Fig. 11

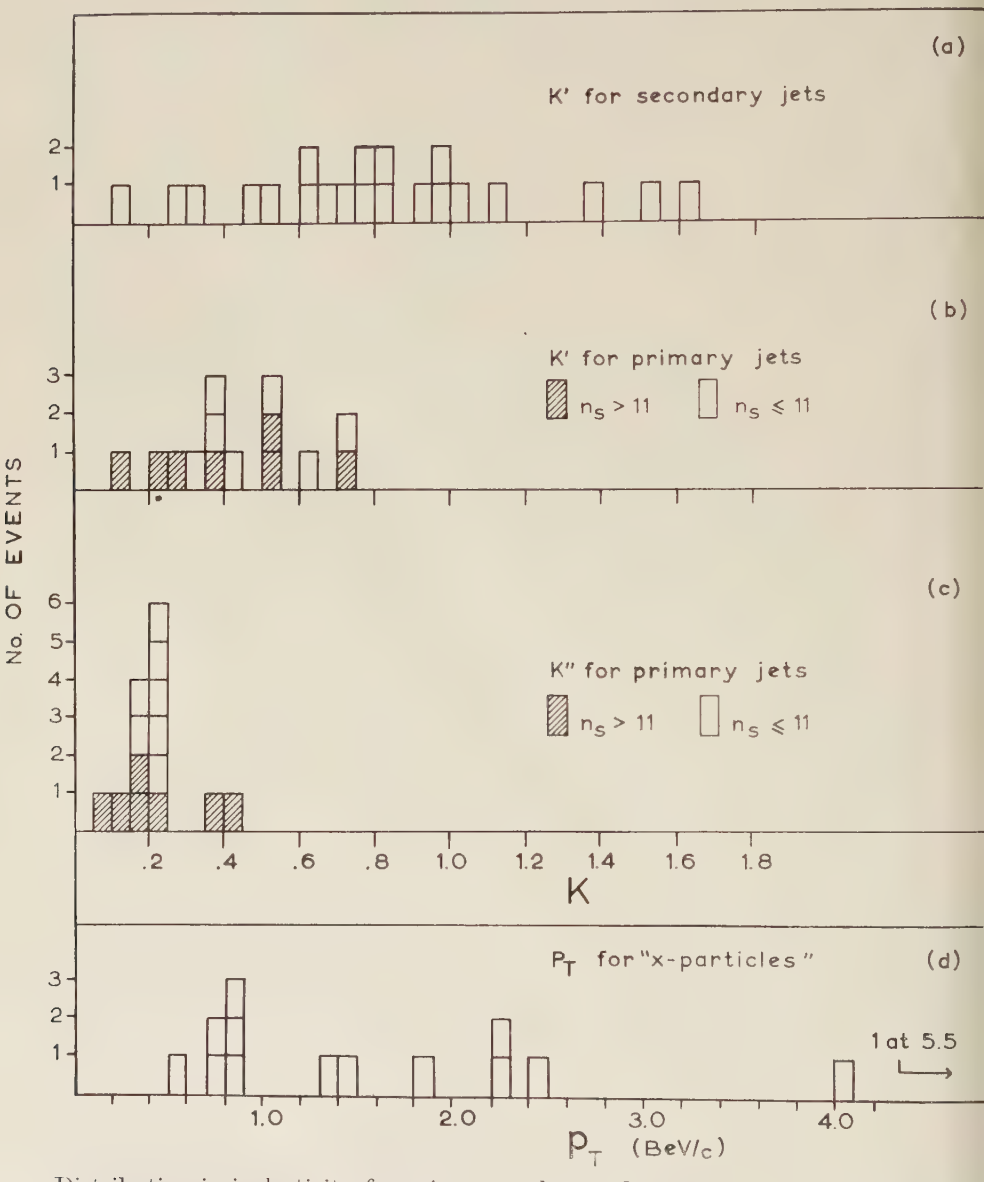

Distribution in inelasticity for primary and secondary jets. K' is the inelasticity assuming all secondaries to be pions, K'' is the inelasticity assuming that 80% of the charged secondaries are pions. For a precise definition of K' and K'' see text. Figure (*d*) gives the distribution of transverse momentum, p_T, for x-particles, obtained, using the values of K''.

secondary particles are pions with $p_T=0{\cdot}5$ BeV/c. Allowing for neutral pions as before, the values of K' obtained are shown in fig. 11 (*b*). The mean value of K' is $0{\cdot}40\pm0{\cdot}07$. One must conclude that the pions carry away *less* than 40% of the total available energy. The inequality arises from the fact that all shower particles have been included in the estimate of K', whereas in fact only 80% are pions.

Even if a value of p_T of 0·8 BeV/c, the mean of the distribution for all charged particles (fig. 6 (*b*)), is assumed, the value of K' is increased only to 0·64. In order to account for the missing energy therefore, one has to assume that the angular distribution of heavy particles, x, is different from that of pions.

We know that the *average* proportion of x-particles among the shower particles is about 20% (see §3). Let us assume that such a proportion holds in *each* event, and that these particles are those emitted at the smallest forward and backward angles in the C-system. The nearest integral number of tracks corresponding to this fraction has been subtracted from both forward and backward cone. In the few events where apparently no charged particles are emitted backwards, 20% have been deleted from the forward cone alone. Assuming the remaining particles to be pions, of $p_T=0{\cdot}5$ BeV/c, the fraction K'' of the available energy radiated in the form of pions, charged or neutral, has been computed according to eqn. (5). The new results for $(\mathrm{cosec}\,\bar{\theta})_{\mathbf{av}}$ have also been plotted in fig. 10, and for K'' in histogram form in fig. 11 (*c*).

The average value of K'' is $0{\cdot}22\pm0{\cdot}05$, with 70% of the values lying between 0·15 and 0·25. The balance must presumably be carried away by the particles x which have been subtracted, and this missing energy can be found in each event. Assuming equal numbers $N_{x^0}=N_{x^\pm}$ as shown in §3, we can therefore compute the mean value of p_T of these particles in each event. The distribution over all events is shown in fig. 11 (*d*), the average value of p_T for x-particles being $1{\cdot}8\pm0{\cdot}5$ BeV/c, which is to be compared with that measured directly from secondary jets produced by neutral particles—fig. 6 (*c*) and table 3. The agreement is seen to be good.

The above procedure involves the extreme assumption that the x-particles are emitted at the smallest angles in the C-system. There is indeed some evidence from fig. 5 that the heavy neutral particles are emitted predominantly at small angles. If they are in fact more widely distributed in angle of emission, there will still be energy unaccounted for. According to some theories, e.g. that of Heisenberg (1953), this energy may be carried away by the incident nucleon. In one of the events in fig. 9 (P20 and P20 nl), a single secondary particle does in fact account for ~75% of the total energy. In other interactions, e.g. (P5 nl), the energy of the neutral secondary particle is much smaller that that of the primary. Thus, many of the heavy x-particles may be θ-particles, emitted with relatively low energy.

No kinematical analysis has yet been made of the jets produced by α-particles, which will form the subject of a separate investigation.

8.3. *Variation of Inelasticity with Energy*

According to the foregoing analysis, the value of K' in the interactions of the secondary particles of jets appears to be large. Since most of these interactions are those of pions, it was concluded that, in pion–nucleon collisions, nearly all the energy re-emerges in the form of pions. In primary proton induced jets, on the other hand, only about one quarter of the available energy appears as pions, the remainder being accounted for by nucleons, or other heavy particles.

In fig. 12, the values of K' for ' secondary ' jets, and K'' for ' primary ' jets, have been plotted as a function of γ_c. Furthermore, secondary jets produced by neutral particles have been included. The distribution obtained shows considerable spread, but there is a general trend of decreasing K with increasing γ_c. It is also apparent that the above distinction between ' primary ' and ' secondary ' jets may be one of energy, rather than of the nature of the initiating particle.

Fig. 12

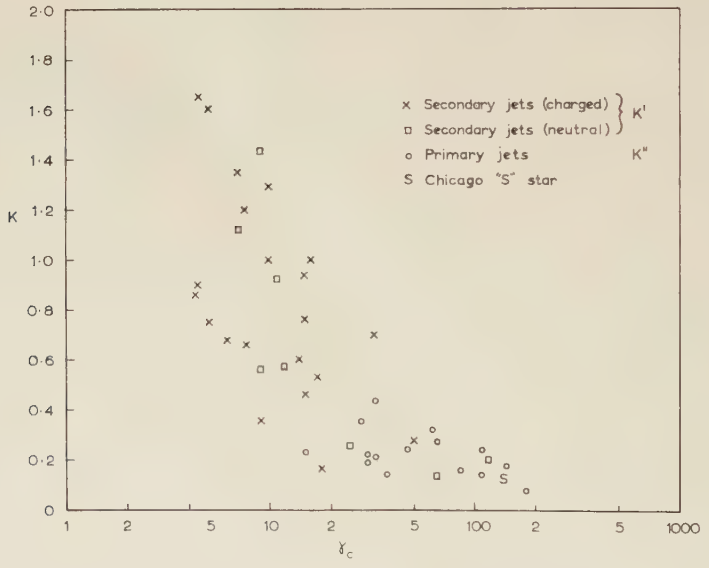

Plot of the inelasticity, K, *vs* γ_c for primary and secondary jets. K was identified with K' for secondary jets, and with K'' for primary jets.

8.4. *Discussion of Results on Inelasticity*

In order to discuss this result further, it is necessary to re-examine the assumptions upon which the calculations of K have been based. The principal assumptions on which our analysis relies are that (1) meson emission takes place symmetrically backwards and forwards from the centre-of-momentum of the collision system, and (2) that if the velocity of the C-system is γ_c, the total available energy in Bev in this system (including rest-energy of the colliding particles), is $2\gamma_c$.

In general, if a primary particle, mass M (in proton mass units) and energy, in terms of its own rest energy, γ_p, in the L-system, collides with a stationary particle of mass N, then

$$\gamma_c \simeq \sqrt{(M\gamma_p/2N)}.$$

The total energy available in the C-system is $\simeq 2N\gamma_c$, and the primary energy would be $\simeq 2N\gamma_c^2$. Thus, if the target is a single nucleon ($N=1$), the energy in the C-system in BeV is approximately $2\gamma_c$ as assumed above, irrespective of the nature of the incident particle. The primary energy, again in BeV, is $M\gamma_p = 2\gamma_c^2$. As mentioned above, the fact that the values of p_T derived from secondary jets agree well with those found by independent methods (and also the evidence in table 3), supports the assumption that the target particle is effectively a single nucleon. The alternative would be to reject the principle of symmetrical emission from the C-system, and the consistency between the different methods of measuring p_T would then have to be regarded as fortuitous.

The assumption $N=1$ implies a long mean free path for pions through nuclear matter. Some information on this point can be obtained from the observed interaction length of the charged particles in the cores of the primary jets. On the basis of 68 interactions, we find a value of 34 ± 4 cm, to be compared with one of 27 cm if the emulsion nuclei were perfectly opaque. If the interaction length were in fact as high as 38 cm, the cross section per nucleon for the charged secondaries would be as low as 20 mb. The corresponding mean free path of the particles through nuclear matter, $\sim 6\times 10^{-13}$ cm, would then be such that, on average, the number of collisions in traversing a light emulsion nucleus (C, N, O) is one, and for the heavy elements (Ag, Br), is between one and two. Since 14% of the secondary events, of high N_h, which probably correspond to ' diametral ' traversals through heavy nuclei, have been excluded, the above hypothesis $N\simeq 1$ would then be quite reasonable.

For the ' primary ' jets, no independent check on the assumed value of the primary energy has been possible. However, the following considerations suggest again that N, the number of simultaneous collision partners, cannot be large. In event P20 (fig. 9), it seems highly probable that the primary event is the result of a single nucleon–nucleon collision, on account of its low multiplicity. The energy of this event is about 40 000 BeV. The energy of event P20 nl, assuming $N=1$, is about 28 000 BeV. If, as might seem probable, on account of the high value of $N_h(8)$, and $n_s(33)$, the neutral particle made several collisions, which were then regarded as simultaneous from the point of view of meson emission, we should have $N>1$, and the energy estimate for the secondary particle would exceed that for the primary.

Furthermore, it can be seen that, if in fact meson emission occurs symmetrically in the C-system of an incident proton and N target nucleons, the values of K' and K'' in fig. 11 (*b*) and 11 (*c*) would have to be decreased by a factor N. According to Cocconi (1954), and Roesler and McCusker

(1953), events of high n_s will correspond to a higher average value of N than those of small n_s. Thus, instead of the quantities K' and K'' being independent of n_s, as shown in fig. 11, they would be smallest for the highest values of n_s and N—a result very difficult to understand on the models of Cocconi, and Roesler and McCusker.

The considerations above suggest therefore that, *either* the concept of (on average) symmetrical emission of particles from the C-system must be rejected, *or* that the velocity of the C-system, and the energy available in it, is determined predominantly by the collision of the incident particle and a single nucleon. This would be reflected in a long mean free path of the primary particles through nuclear matter.

§ 9. Summary and Comparison of Experimental Results with Theory

The main results of the present analysis may be summarized as follows :

(*a*) In the core of the jets, $80\pm7\%$ of the particles are pions ; the remainder are nucleons and other heavy particles.

(*b*) The composition of the particles at wide angles has been investigated by direct mass measurements and less than 70% of the charged particles are pions.

(*c*) The mean transverse momentum of the pion secondaries of jets is 0·5 Bev/c, and independent of angle of emission or primary energy.

(*d*) The mean transverse momentum of the heavy secondaries is of the order of 1–2 Bev/c.

(*e*) The multiplicity, n_s, varies widely in jets of comparable energy. There is a correlation between n_s and the degree of anisotropy of the angular distribution.

(*f*) The momentum spectrum of the mesons, averaged over all jets, is of the form dp/p^2.

(*g*) The inelasticity, K, of the collisions appears to be of the order of unity in secondary jets, and of the order of 0·2 in primary proton induced jets. K_{av} appears to decrease continuously as the primary energy increases. No variation of K with n_s has been detected, for proton-induced events of $N_h<13$.

A summary of the predictions of the different theories, and comparison with the experimental results, is given in table 4. It must be remembered that our data refer to nucleon–nucleus collisions, whereas the theories apply to nucleon–nucleon collisions. It will be seen that the theories of Fermi (1950) and Landau (1953) do not agree with the experimental findings, which are better represented by the theories of Heisenberg (1953),

Table 4

	Fermi	Landau	Heisenberg	Kraushaar and Marks	This experiment
Transverse momentum p_T	Several BeV, greatest at $\bar{\theta}=90°$	Varies from ~2 BeV at $\bar{\theta}=90°$ to 4 BeV at $\bar{\theta}=0°$	$\sim m_n c$ for all $\bar{\theta}$	—	$p_T=0{\cdot}5$ BeV/c for pions, and 1–2 BeV/c for heavy particles
Inelasticity K	$K\sim 1$, little variation about average for all energies	As for Fermi	$K_{\text{av}}<1$, large variation depending on impact parameter. K_{av} decreases with increasing primary energy	$K_{\text{av}}<1$, depending on impact parameter	$K_{\text{av}}<0{\cdot}2$ at energy 10 000 BeV; decreases with increasing primary energy
Variation of K with n_s	—	—	Strong; n_s increases with K	As for Heisenberg	Independent
Angular anisotropy, m	Small anisotropy, independent of energy	Anisotropy strong, increasing with energy	Anisotropy for distant collisions (small K, small n_s). Isotropy for large K, n_s	Anisotropy depends on degree of nucleon excitation. Isotropic for large K, anisotropic for small K	Strong anisotropy for small n_s: weak anisotropy for large n_s

Kraushaar and Marks (1954), Bhabha (1953) and Lewis *et al.* (1948). These models however predict an increase of K with increasing multiplicity, contrary to our observations.

§ 10. Discussion of Results

The principal features of our observations are that (1) K appears to decrease with increasing γ_c, and (2) that the value of K at a given energy does not depend strongly on n_s.

The observed dependence of K on γ_c is qualitatively in agreement with the predictions of the Heisenberg theory. In his model, the collision takes place only in the region where the pion fields of the two nucleons overlap. Let χ represent the mass equivalent in Bev of the field of the incident nucleon, which overlaps with a mass χ' of the field of the struck nucleon(s). In Heisenberg's theory, $\chi=\chi'$, but it seems possible that the ratio χ/χ' will depend on the exact states of the colliding nucleons at the time of impact. Furthermore, the value of χ' in a nucleon–nucleus collision may be greater than that in a nucleon–nucleon collision. The energy radiated in the C-system will be $\simeq 2\chi'\gamma_c$, and the energy of the incident nucleon in the L-system, $2(\chi'/\chi)\gamma_c^2$. The apparent value of $K=2\chi'\gamma_c/2\gamma_c=\chi'$.

In Heisenberg's theory, the only restriction on χ' is that $2\chi'\gamma_c \geqslant 2m_\pi c^2$; thus χ' and K can decrease indefinitely as γ_c increases, and 'fringing' collisions become progressively more important. It has been suggested to us by Dr. Bohm that in fact χ (and χ') must be quantized: $\chi'=a\cdot m_\pi c^2$, where a is an integer. According to the results of fig. 12, $a\sim 1$ at very high energies. The following model appears capable of explaining this result. In the first nucleon–nucleon encounter inside the nucleus, both nucleons are stripped of their fields, each of which is equivalent to a *single* virtual pion, an assumption which implies weak coupling between pion and nucleon, at least for a pion which is not too close to the nucleon core. In traversing the nucleus, the bare incident nucleon is incapable of further interaction. The interaction between the pions, on the other hand, is extremely strong, and may be treated along the lines suggested by Heisenberg. However, the degree of non-linearity in this interaction will vary from event to event. Thus in some cases (e.g. P20 in fig. 9) a few high energy mesons are produced in a distant collision, whereas in a closer collision, such as P20 nl, the non-linearity is very strong and a larger number of lower energy particles are produced. However, the value of $K=\chi'\simeq m_\pi c^2$ should be the same in the two cases. High multiplicity events, corresponding to close collisions, might also be expected to result in a higher proportion of K-particles, assuming that there is a K-particle field of dimensions $\simeq h/m_K c$ around the nucleon core. The transverse momentum of the K-particles should also be larger by a factor m_K/m_π than that of the pions. As we have seen, these features are borne out by our results.

The non-linearities postulated above arise essentially from the Lorentz contraction of the fields, and the resulting high energy densities in them; at low primary energies their effect will be much smaller. As indicated in fig. 12, the effective value of χ' becomes much greater than $m_\pi c^2$ for $\gamma_c < 10$.

The above assumptions imply that the minimum value of K in high energy collisions will be $\sim 0{\cdot}15$, and it would be of great interest therefore to make investigations at much higher energies, in order to check this point. It is also clear that, according to the present model, the pion nucleon cross section should be greater than the nucleon–nucleon cross section at very high energies—since the latter contains the probability that a virtual meson is available for interaction, a probability less than unity on a weak coupling theory. This would result in a long mean free path for the nucleons—for example, those carrying off the remaining 85% of the primary energy in the above model. It is of interest to note that in our events, a secondary interaction of energy comparable with that of the primary has been observed in only two cases, although the length of jet cores scanned for such interactions is around two metres. Such a result would also be consistent with the very long attenuation mean free path of the nucleonic component of extensive air showers.

Acknowledgments

It is a pleasure for us to thank Professor C. F. Powell for the facilities of this laboratory, and for his interest during the course of the work. We wish to acknowledge the assistance of the scanning team, consisting of Miss P. Curry, Mrs. M. Herman, Mrs. N. Hillier and Mrs. M. Webb. Some of the preliminary analysis of event P20 was carried out by Dr. F. Brisbout and Mr. P. H. Fowler, and we are also grateful to the latter for some suggestions. Many of the comments in § 10 are the result of proposals by Dr. D. Bohm, to whom we are grateful for a number of discussions.

B. E. thanks the D.S.I.R. for a maintenance grant, J. L. the National University of Ireland for a scholarship, K. P. thanks Professor E. Bagge, and the Studienstiftung des deutschen Volkes for financial support, and J. R. the Guggenheim Foundation for a Fellowship.

References

Barkas, W. H., Birge, R. W., Chupp, W. W., Ekspong, A. G., Goldhaber, G., Goldhaber, S., Heckman, H. H., Perkins, D. H., Sandweiss, J., Segrè, E., Smith, F. M., Stork, D. H., van Rossum, L., Amaldi, E., Baroni, G., Castagnoli, C., Franzinetti, C., and Mandfredini, A., 1957, *Phys. Rev.*, **105**, 1037.

Bhabha, H. Y., 1953, *Proc. roy. Soc.* A, **219**, 293.

Brisbout, F. A., Dahanayake, C., Engler, A., Fujimoto, Y., and Perkins, D. H., 1956, *Phil. Mag.*, **1**, 605.

Castagnoli, C., Cortini, G., Franzinetti, C., Manfredini, A., and Moreno, D., 1953, *Nuovo Cim.*, **10**, 1539.

Cocconi, G., *Phys. Rev.*, 1954, **93**, 1107.

Daniel, R. R., Davies, J. H., Mulvey, J. H., and Perkins, D. H., 1952, *Phil. Mag.*, **43**, 753.
Edwards, B. P., Engler, A., Friedlander, M. W., and Kamal, A. A., 1957, *Nuovo Cim.*, **5**, 1188.
Fermi, E., 1950, *Progr. theor. Phys.*, **5**, 570.
Glasser, R. G., Haskin, D. M., Schein, M., and Lord, J. J., 1955, *Phys. Rev.*, **99**, 1555.
Heisenberg, W., 1952, *Z. Phys.*, **133**, 65; 1953, *Kosmische Strahlung* (Berlin : Springer).
Kraushaar, W. L., and Marks, L. J., 1954, *Phys. Rev.*, **93**, 326.
Landau, L. D., 1953, *Dokl. Akad. Nauk, S.S.S.R.*, **12**, 51.
Lewis, H. W., Oppenheimer, J. R., and Wouthuysen, S. A., 1948, *Phys. Rev.*, **73**, 127.
Oda, M., *Cooperative Emulsion Group in Japan*, Report at the Varenna Conference, June 1957.
Pinkau, K., 1957, *Phil. Mag.*, **2**, 1389.
Roesler, F. D., and McCusker, C. B. A., 1953, *Nuovo Cim.*, **10**, 127.

The Process of Magnetization by Chemical Change†

By G. Haigh
Department of Physics, Imperial College, S.W.7

[Received December 3, 1957]

Abstract

In this paper the well-known processes of magnetization of rocks are discussed and compared and contrasted with the magnetization formed when a ferromagnetic mineral undergoes a chemical change within the influence of an external magnetic field. The thermal stability of the ' chemical-magnetization ' so produced is examined and compared with the magnetizations produced isothermally and thermo-remanently in iron oxides under similar field conditions. The theoretical aspects of such a process of magnetization are considered and the nature of the resulting magnetization is accounted for theoretically. Possible applications in rock magnetic studies are also discussed.

§ 1. The Magnetization of Ferromagnetic Minerals

The magnetization of a body, in particular a rock or mineral specimen, may be effected in one or more of several possible ways. The two most common and understood ways are, firstly, magnetization at a constant temperature when, on removal of the field, we observe the isothermal-remanent magnetization (I.R.M.); and, secondly, by allowing a field to act on a cooling body between two temperatures T_1 and T_2 (below the Curie temperature θ), the magnetization of the body at room temperature is then known as the thermal-remanent magnetization (T.R.M.) applicable to the particular temperature and field conditions. For a rock specimen in the T.R.M.-case, we are usually concerned with the effects of the cooling in the earth's field of the ferromagnetic minerals, from above their respective Curie temperatures. The relative intensity of magnetization produced by the same small fields (of the order of 50 oersted or less) in the two cases, and the relative stability of these two magnetizations have been reviewed elsewhere, principally by Thellier (1954) and Néel (1949).

A third and less well-known process of magnetization of great interest and importance in the field of rock magnetism is that created when a ferromagnetic mineral undergoes a chemical change within the influence of a magnetic field—this form of magnetization will be referred to herein as ' chemical magnetization '.

The process of chemical magnetization will be considered firstly in the case of weak fields (less than 1 oersted), and then for higher fields up

† Communicated by Professor P. M. S. Blackett, F.R.S.

to 150 oersted. After a theoretical discussion of the formation and character of chemical magnetization, the general application to rock magnetism will be considered.

§ 2. Chemical Magnetization of Initially Magnetized Specimens

By means of a furnace designed and constructed by Leng (1955) it has been possible to make observations with an astatic magnetometer, on the growth of magnetization induced by a small field of the order of 0·5 oersted, during the hematite-magnetite reduction process. The specimens used were in the form of powders, about 2 g being pressed in a small platinum cup, and heated in an atmosphere of coal gas to a temperature ~300°C, when the reaction proceeds at a convenient rate for observations to be made.

Fig. 1

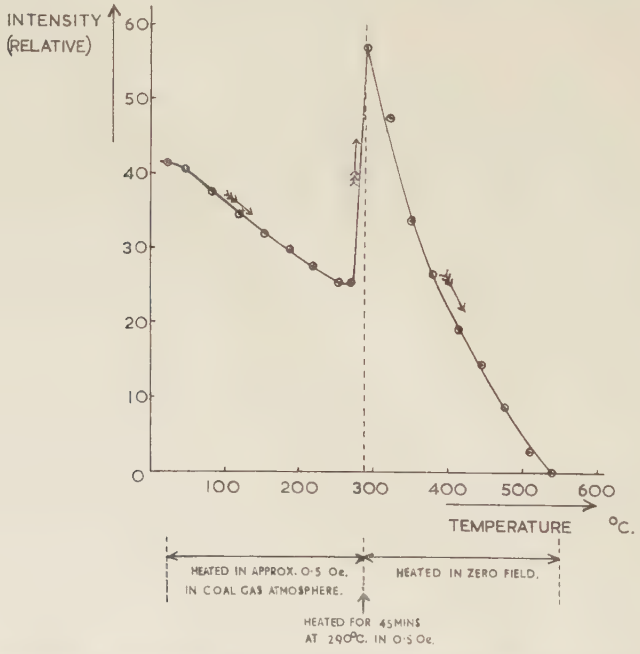

Initially magnetized specimen of αFe_2O_3 heated in a reducing atmosphere of coal gas, with ambient field in same direction as initial remanence.

The effect of such a chemical change on a previously magnetized specimen can be seen from figs. 1 and 2. The direction of the external field, in which the chemical reaction takes place, is in the same direction (fig. 1), and the opposite direction (fig. 2), to that of the initial remanent magnetization of the specimen. In the former case there is an increase

in the magnetization in the same direction as the original remanence, whilst in the latter case the direction of the chemical magnetization is opposite to that of the initial remanence of the hematite specimen. If, then, a chemical change occurs in a ferromagnetic mineral in the presence of even a weak external magnetic field (0·5 oersted), the newly-formed mineral grows in such a way as to reproduce the direction of the external field, and, provided the chemical change proceeds to completion, all traces of the previous magnetization disappear.

Fig. 2

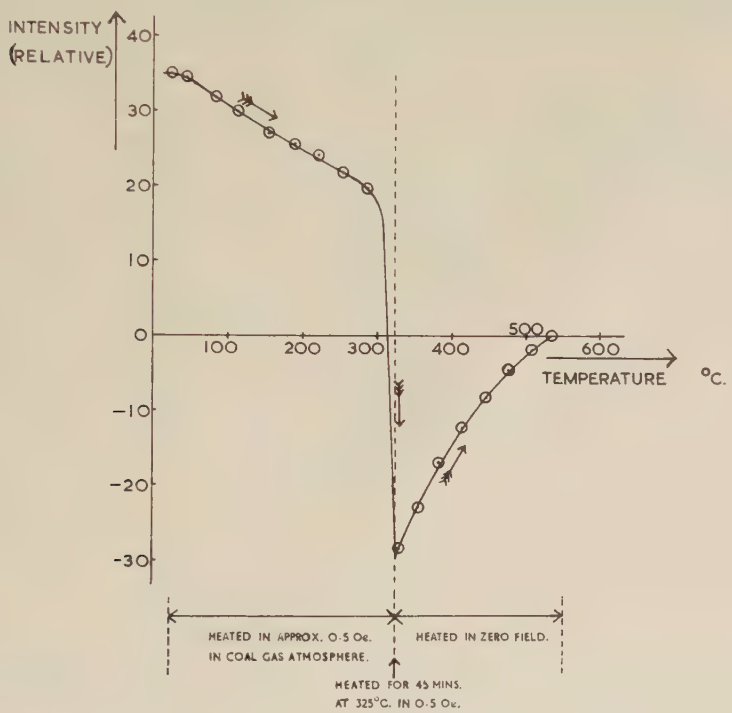

Initially magnetized specimen of αFe_2O_3 heated in a reducing atmosphere of coal gas, with ambient field in opposite direction to initial remanence.

In figs. 1 and 2, the parts of the curves above the reduction temperatures to Curie point are taken in zero field. This was necessary because at these elevated temperatures the relaxation time of the mineral formed (magnetite) was comparable with the times of measurement—the method of measurement involving rotation of the specimen through 180° under an astatic magnetometer and observing maximum and minimum deflections, could only be achieved therefore in zero external field. It may be mentioned briefly here that whilst the Curie point observed, 540°C, for the magnetite formed, is less than the more usual figure of 575°C quoted for this mineral, it is not unusual to find seemingly pure magnetite with

Curie points about 500°C. It has been found that the magnetic properties of magnetite are not as consistent as has been thought in the past, but vary with the method of preparation and treatment of the sample ; this variation is not, however, as pronounced as in the case of hematite (Haigh 1957 a, b).

§ 3. Chemical Magnetization of Unmagnetized Specimens

If an unmagnetized specimen of hematite is heated to 288°C in about 0·5 oersted in a reducing atmosphere, then curve ① of fig. 3 is observed. The chemical change, and resulting growth of the magnetite in the external field, becomes noticeable above about 225°C. With the specimen

Fig. 3

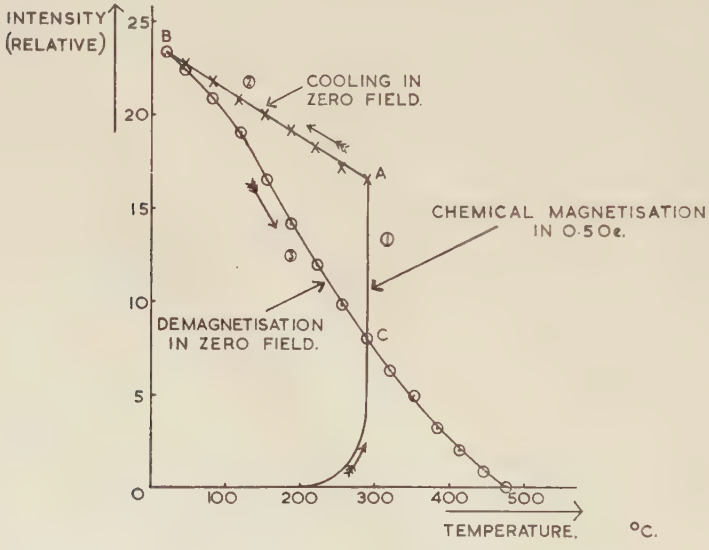

Growth and thermal demagnetization of chemical remanence formed by the reduction process $\alpha Fe_2O_3 \rightarrow Fe_3O_4$ in 0·5 oersted.

used in this experiment the reduction was allowed to continue at 288°C for some 70 min when the reaction was assumed to be completed—the magnetometer deflection having remained unaltered for several minutes.

Curve ② was taken in zero field and shows the increase in magnetization on cooling. Reheating of this specimen in an inert atmosphere (nitrogen) in zero field, gives the thermal demagnetization curve ③. The shape of this curve is interesting in that it does not display the usual initial rapid decrease in intensity which is characteristic of magnetization of an isothermal nature. There is, however, a further interesting feature, viz. the non-coincidence of points A and C. If AB were simply an increase in intrinsic magnetization due to decrease in temperature, then the point C in the reheating curve would be expected to coincide with the point A.

There are, however, two possible reasons for the non-coincidence of these points.

As has already been mentioned, the relaxation time at 288°C is found to be comparable with times of measurement, so that it is likely that there will be a time decay of magnetization at or below 288°C in zero field. The second possibility is that, on account of the size of the particles involved in these experiments, there will be the formation of closure-domains on cooling, this also tending to decrease the magnetization observed at room temperature. Thus AB is the resultant of three effects: the increase in spontaneous magnetization, the time decay of magnetization, and the formation of domains—the latter two acting in such a way as to oppose the effect of the former.

§ 4. Time Effects and Thermal Stability of Chemical Magnetization

The possible time effects mentioned above have been observed at 350°C by switching off the field of 0·5 oersted and making magnetization observations in zero field. Figure 4 shows the isothermal decay in zero field of the chemical magnetization produced in a field of 0·5 oersted

Fig. 4

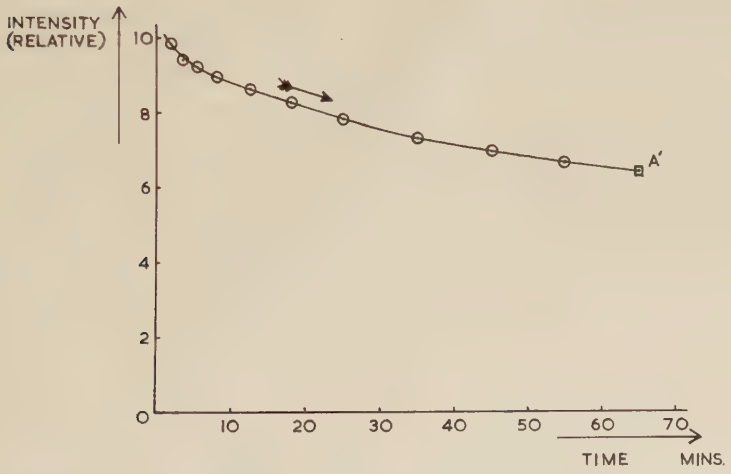

Isothermal decay in zero field of the chemical magnetization produced in a field of 0·5 oersted at 350°C.

at 350°C. The magnetization has decreased by about one-third in 70 min, and from the shape of the curve the decay is by no means complete. If now this specimen is allowed to cool in zero field, a curve similar to curve ② of fig. 3 is again obtained, but, on reheating in an inert atmosphere, the point C is now very much nearer to A (C′ and A′ in fig. 5), and the whole curve is more concave in shape.

Apart from the information it gives about the Curie points of the ferromagnetic minerals present, the shape of the thermal demagnetization curve of a specimen is of great interest in rock magnetism studies, particularly from the point of view of the magnetic stability of the specimen.

Fig. 5

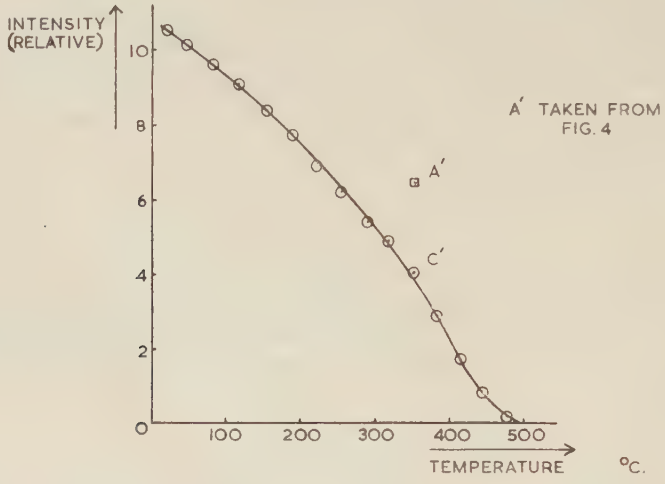

Thermal demagnetization after time decay shown in fig. 4.

Fig. 6

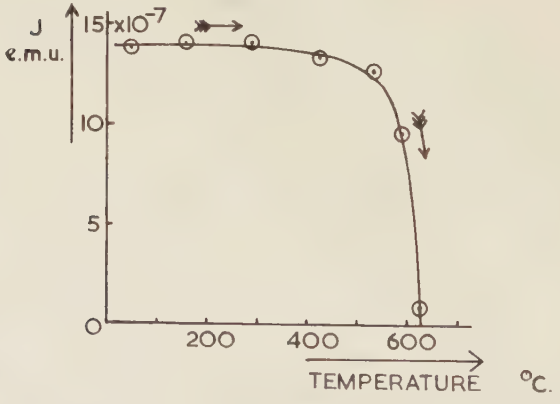

Thermal demagnetization of normal Triassic sandstone from Carlisle area (repeated heating method). (After Leng.)

Leng, and others, have shown by a method of successive heating and cooling cycles in zero field to progressively higher temperatures, that sedimentary rocks, and those rocks magnetized by thermal-remanence, have a ' rectangular ' thermal demagnetization curve (Leng 1955). The magnetization changes little with temperature until near the Curie point

when the intensity falls off rapidly. Using an astatic magnetometer, it has been possible to observe directly the fall-off of magnetization on heating of some strongly-magnetized baked sediments, although with this latter method, the thermal demagnetization curves necessarily lose some of their rectangular appearance. Typical curves obtained by the two methods by Leng are shown in figs. 6 and 7, whilst fig. 8 shows for

Fig. 7

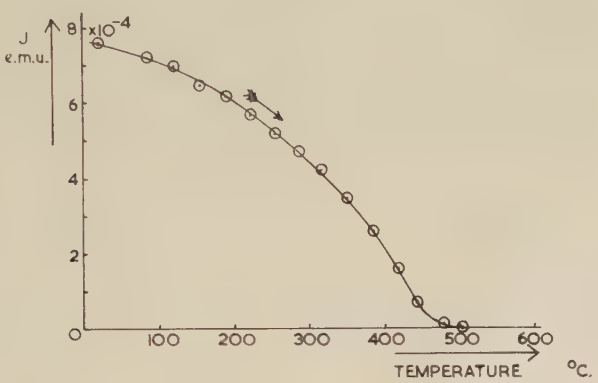

Thermal demagnetization of normal baked Arran sediment (direct observation with magnetometer during heating). (After Leng.)

Fig. 8

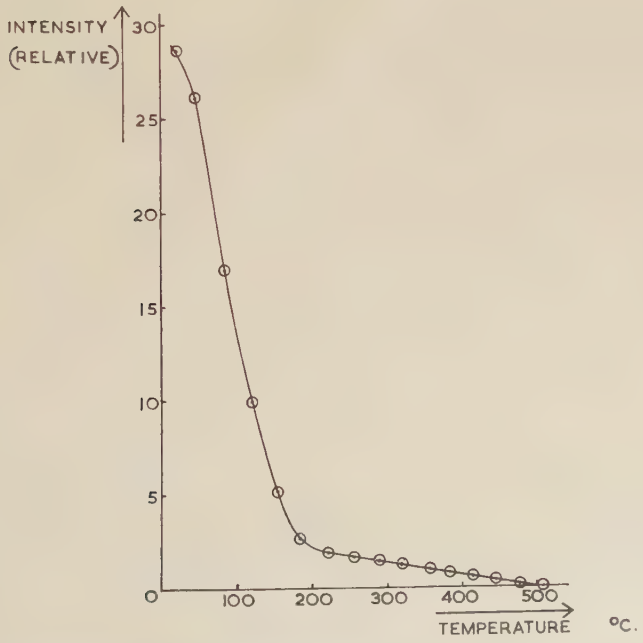

Thermal demagnetization of magnetite specimen after isothermal magnetization at 20°c in 6000 oersted.

comparison a typical thermal demagnetization curve of a specimen of magnetite magnetized isothermally at 20°c in about 6000 oersted. It is useful to compare curve ③ of fig. 3 and the curve of fig. 5 with the curves for the natural rocks. From the similarity of figs. 5 and 7 in particular, it is significant that the thermal demagnetization curves of the two different forms of magnetization are so markedly similar. Clearly, chemical magnetization more resembles thermal-remanent magnetization, at least from the point of view of its thermal stability, than it does isothermal-remanent magnetization. In nature, the process of chemical magnetization at an elevated temperature, is accompanied by a very long period when the magnetization created can decay, and subsequently appear as a seemingly ' harder ' form of magnetization with a correspondingly more rectangular or concave thermal demagnetization curve.

§ 5. Isothermal Chemical Magnetization

In nature, however, the chemical changes can take place at very much lower temperatures than have been used here—in fact, within the range of terrestrial temperatures. Consequently, of great importance is the nature of a magnetization produced during a chemical change at a constant temperature, i.e. produced isothermally, but over the long

Fig. 9

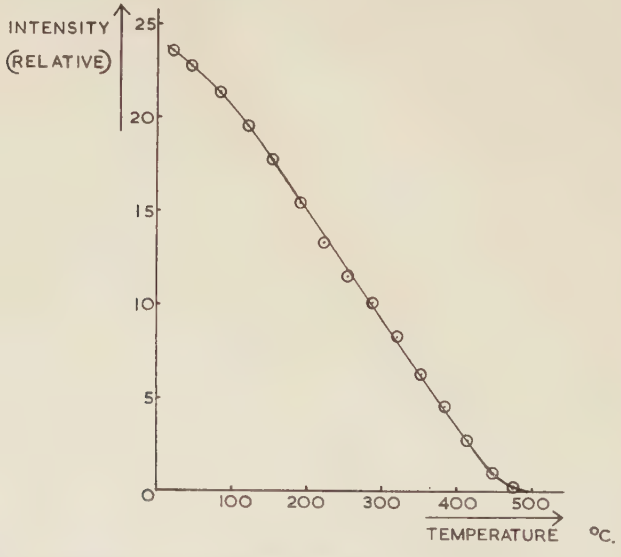

Thermal demagnetization of the magnetization produced isothermally at 350°c.

periods of time necessary for such a reaction to take place at, say, terrestrial temperatures. Quite obviously such an experiment cannot be undertaken under laboratory conditions, however, the following sequence of observations most nearly fills the requirements of such an

experiment: a specimen of hematite is heated in an inert atmosphere to 300°c, when, in the presence of an external field of 0·5 oersted, coal gas is introduced and the reduction process takes place isothermally at 300°c. After completion of the chemical change, the isothermal decay of magnetization in zero field takes place and the specimen is subsequently cooled to 20°c in zero field.

Reheating in an inert atmosphere to Curie point gives the form of thermal demagnetization curve shown in fig. 9, which is very similar to fig. 5 although not showing quite the same degree of concavity. Nevertheless, the two curves are sufficiently alike for us to conclude that, in this case at least, the magnetization produced isothermally at 300°c has very similar thermal stability properties to the magnetization produced during heating through the temperature range 225° to 350°c, as described in § 4.

§ 6. Chemical Magnetization in High Fields up to 150 Oersted

So far observations have only been made of the reduction process $\alpha Fe_2O_3 \rightarrow Fe_3O_4$ in weak fields of the order of the earth's field. It is of interest to know the effect of higher fields up to, say, 150 oersted on the magnetization produced and to compare and contrast it with the measurements made with the weak fields.

An instrument was devised in which it was possible to carry out this chemical change in fields up to 150 oersted, and at the same time make magnetization measurements with a relatively insensitive astatic magnetometer—this apparatus is described more fully elsewhere (Haigh 1957 c). It was essential in this work to follow a strict procedure in the reduction process and field application at a fixed temperature in order to obtain meaningful results. The following procedure was adopted: specimens of α ferric oxide powder in a platinum cup were heated in a coal gas atmosphere to 340°c in known fields; this field was maintained at 340°c for some 12 minutes when the specimen was allowed to magnetically decay isothermally in a low field (actually the earth's field) for an hour, and then cooled to room temperature. The rate of heating to 340°c and cooling to room temperature was kept the same in all experiments. The fields in which the chemical change was observed were 20, 50, 95 and 145 oersted.

The remanent moment of the specimens after cooling, plotted as a function of the ambient field during the chemical change, is shown in fig. 10. In the low field region the moment induced during the chemical change is proportional to the ambient field—this proportionality had also been found for the weak fields and seems to extend up to fields of about 40 oersted. For still higher fields there is a departure from this linearity, the remanent moment beginning to show a saturation effect which, in this case, may become complete for fields of the order of 350 oersted.

In § 5 we compared the magnetization produced isothermally at 350°c in 0·5 oersted, during the chemical change $\alpha Fe_2O_3 \rightarrow Fe_3O_4$, with the magnetization produced in this field when the chemical change was allowed to take place during the whole of the temperature increase to 350°c. We can make a comparison of the magnetizations similarly

Fig. 10

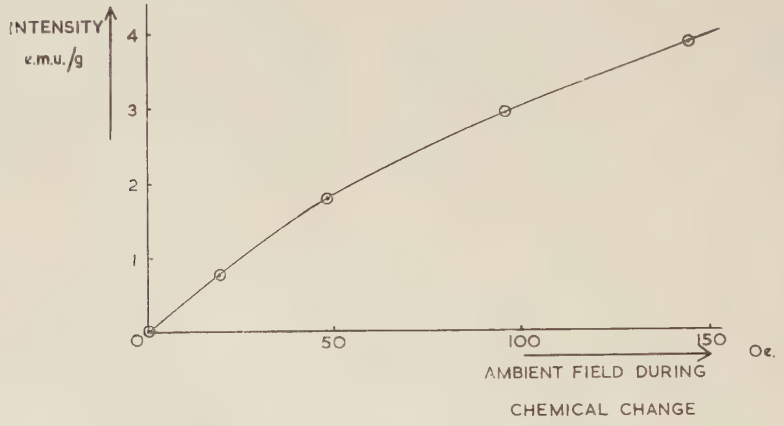

Intensity of magnetization produced during the chemical change as a function of the ambient field.

Fig. 11

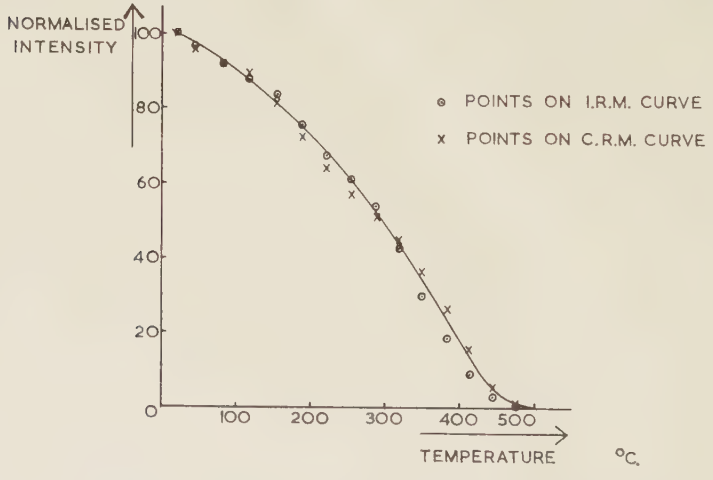

Comparison of thermal stability of chemical magnetization, and magnetization formed isothermally at 350°c in field of 72 oersted.

produced in higher fields. Figure 11 shows the thermal demagnetization of these two types of magnetization produced in a field of about 72 oersted. Here the similarity between the two is even more marked than in figs. 5 and 9.

§ 7. Comparison of Chemical Magnetization with I.R.M., T.R.M., and Anhysteretic Magnetization

In order to compare this chemical magnetization with the magnetizations referred to in § 1, a specimen of the magnetite formed in the chemical change was used to determine the isothermal- and the isothermal-anhysteretic-magnetization curves (Thellier 1954) of the material at room temperature for fields up to about 150 oersted. Anhysteretic magnetizations is effected by superimposing a large alternating magnetic field (of the order of the saturating field) on the steady direct field in which the specimen is situated. The amplitude of the alternating field is slowly reduced to zero and the direct field is then removed. This process, repeated for increasing values of the direct field, then gives the anhysteretic magnetization curve. In the present experiments the maximum amplitude of this alternating field was 980 oersted.

Fig. 12

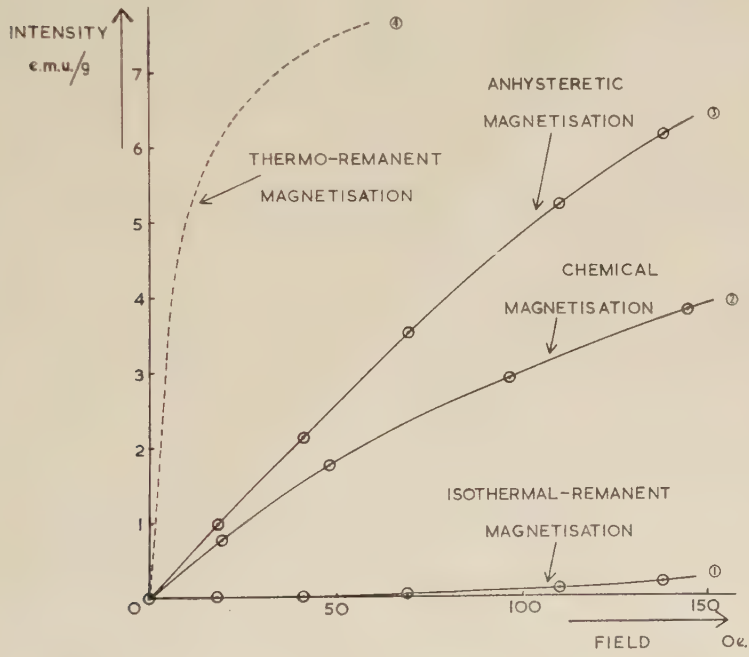

Comparison of different forms of magnetization exhibited by magnetite specimens.

These isothermal-magnetization curves, together with the chemical magnetization curve, are shown in fig. 12. Also in this figure, and shown dotted, is the probable thermal-remanent magnetization curve—this being drawn after reference to the figure given in the paper by Thellier (1954). Clearly from the comparison of these curves, the chemical magnetization formed in this particular investigation is more like anhysteretic and

thermal remanent magnetization than the isothermal magnetization, as has been deduced earlier from the thermal demagnetization curves.

§ 8. Theoretical Aspects of Chemical Magnetization

8.1.

During the chemical change, the newly formed grains of magnetite are aligned by the weak external field in spite of the opposition due to randomizing thermal fluctuations. A simple calculation of the energies involved clearly shows that such an alignment will be prevented by the thermal fluctuations. The formation of a remanent magnetization during the chemical change in such weak fields must then be explained theoretically in some other way.

8.2.

Experimentally it has been found by several workers (Kopelman 1952, Meiklejohn 1953, Becker 1957) that very small particles, of the order of several tens, to a few hundreds, of ångströms in diameter, have very much smaller coercivities than particles of micron sizes. The variation of the coercivity with particle size for particles of iron is plotted in fig. 13 (*a*) and shows that the coercivity at very small particle size can be extremely

Fig. 13 (*a*)

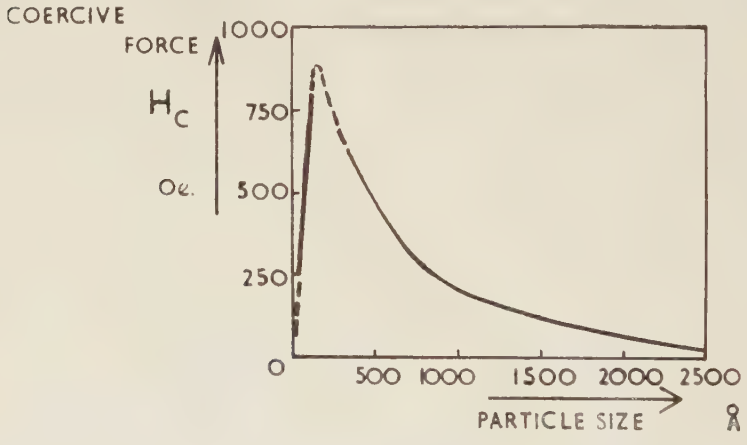

Variation of coercive force with particle size for particles of iron. (After Kopelman.)

small. Figure 13 (*b*) shows a similar curve for particles of cobalt in copper. In this latter case the coercivity is about 1 oersted or less for particles up to about 15 Å in radius. (Heat treatment of 10 min produces particles of 13 Å radius, whilst after 100 min the particle radius is about 65 Å.) Clearly, from these two particular experimental results at least, the coercive force can be extremely small, and probably of the order of 0·5 oersted for very small particles.

We must now consider the general magnetic properties of an assemblage of very small particles.

Following Néel (1949, 1955), we will first consider the simple case of a magnetically uniaxial, single domain grain. The magnetic moment, vJ_s, of such a grain, of volume v and spontaneous magnetization J_s, can, in the absence of an applied field, take up either of the two orientations of

Fig. 13 (*b*)

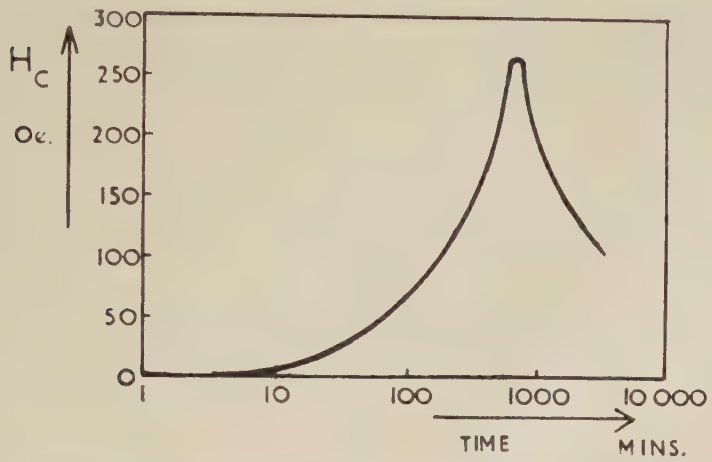

Change in coercive force with annealing time at 700°c for particles of cobalt in copper. (After Becker.)

minimum energy, $\theta=0$, or $\theta=\pi$, where θ is the angle between the magnetic moment and the axis of the grain. Now, if the height of the potential barrier between these two positions is very large compared with kT, then the magnetization of the grain will always remain in the direction to which it was brought by an applied magnetic field. However, the height of this potential barrier is $\frac{1}{2}(vH_cJ_s)$, and since it is directly proportional to v, a value for the grain size can always be found such that the barrier height is of the order of kT, in which case the thermal fluctuations will cause the moment to change spontaneously from one position to the other.

In these particular conditions, if a remanent moment J_0 is given to each grain of an assemblage of identical grains, then it will tend to zero according to

$$J_r=J_0 \exp(-t/\tau_0)$$

where τ_0 is designated the relaxation time of the grain. This relaxation time depends upon the perturbing couples acting on the magnetic moment of the grain. It seems, according to Néel, that the most active of these couples arises from elastic deformations of the grain by thermal agitation. Considerations of these perturbations enables the relaxation time, τ_0, for the grain to be calculated, and gives

$$\frac{1}{\tau_0}=C \exp\left(-\frac{vH_cJ_s}{2kT}\right) \quad . \quad . \quad . \quad . \quad . \quad . \quad . \quad (1)$$

where

$$C=\frac{eH_c}{2m}(3G\lambda+DJ_s^2)\left[\frac{2v}{\pi GkT}\right]^{1/2} \quad . \quad . \quad . \quad . \quad . \quad (2)$$

and where e, m are the charge and mass of the electron, G the shear modulus, λ the longitudinal magnetostriction at saturation, and D a numerical constant depending upon the shape of the grain and equal to about 3. Thus the relaxation time τ_0 is dependent upon the physical constants of the grain, and v/T. The effect of v/T in the expression for C (eqn. (2)) will be negligible compared with v/T appearing in the exponent in eqn. (1), and thus, to all intents and purposes, C can be regarded as a constant. The relaxation time for the grain, then, can be simply expressed as

$$\frac{1}{\tau_0}=C\exp\left(-A\frac{v}{T}\right)$$

where A is a constant equal to $H_cJ_s/2k$, essentially independent of v/T, except at temperatures near the Curie point.

Similar calculations have been applied by Néel to the case where there is an external magnetic field h, parallel to the axis of the grain. There are now two relaxation times, $\tau(0,\pi)$ and $\tau(\pi,0)$, corresponding to movement from the position $\theta=0$ to $\theta=\pi$, and *vice versa*. These are

$$\frac{1}{\tau(0,\pi)}=C\left(1+\frac{h}{H_c}\right)\left(1-\frac{h^2}{H_c^2}\right)^{1/2}\exp\left(-\frac{vJ_s(H_c+h)^2}{2H_ckT}\right) \quad (3)$$

and

$$\frac{1}{\tau(\pi,0)}=C\left(1-\frac{h}{H_c}\right)\left(1-\frac{h^2}{H_c^2}\right)^{1/2}\exp\left(-\frac{vJ_s(H_c-h)^2}{2H_ckT}\right). \quad (4)$$

Thus the stability of a given grain of a ferromagnetic material in a given field is therefore governed solely by the size of the grain and the temperature, provided the temperature does not approach Curie point. If the temperature does approach Curie point, then the variation of J_s and H_c with temperature will have to be taken into account and the values appropriate to the prevailing temperature inserted in eqns. (3) and (4). At a given temperature (away from the Curie point) a grain magnetized in an external field can therefore become magnetically stable by growing sufficiently to make τ large. As this growth takes place, it is clear from eqns. (3) and (4) that the individual grains will tend to become stable with their magnetization vectors along the direction of the ambient field—remembering that in the early stages of the nucleation $H_c\sim h$, but that H_c rapidly increases as the nucleation proceeds. In this particular case of a nucleation process, magnetic stability is achieved not only by an increase in v tending to make τ large, but also by the effective H_c increasing with v at a constant temperature. This is precisely the state of affairs we have in the case of chemical magnetization.

8.3.

Considering the present case of the reduction of αFe_2O_3 to Fe_3O_4 at a constant temperature of 300°C, the magnetization of the compact specimen

will grow by a nucleation process. Very small regions of Fe_3O_4 will form during the reduction and become magnetized by the ambient field of 0·5 oersted on account of the low coercivity of such nuclei. As the chemical reaction proceeds, these nuclei will grow, rapidly become magnetically stable, and, by the above argument, the direction of the final moment will then be along the direction of the ambient field.

Thus, although no theory has so far been developed which satisfactorily predicts the coercivity variation with particle size found experimentally (figs. 13 (*a*) and (*b*)), nevertheless, these experimental curves do show that for very small ferromagnetic particles the coercivity can be of the order of a few oersteds or less. Having established this, the theory originally developed by Néel to account for thermal remanent magnetization (T.R.M.) can then be applied to the present case of chemical magnetization. This theoretical application successfully predicts that a magnetization will form during the chemical change, and that it will become stable as the initial nucleation process proceeds to completion.

§ 9. Comparison of Chemical Magnetization with T.R.M.

The theoretical discussion just presented so closely follows that given by Néel for the case of thermal remanent magnetization that it is interesting to compare the two theories, and further, to compare the types of magnetization to be expected in the two cases.

To understand the thermal-remanent case it must be remembered that the individual coercive forces of the grains are of the order of K/J_s and tend to zero at the Curie point (K being the anisotropy constant). This is an experimental fact explained theoretically by the variation of K as J_s^2, whether K be due to magneto-crystalline or shape anisotropy, although in this latter case the second-power dependence is not completely established; thus H_c varies as J_s and tends to zero at the Curie point. Even a very small magnetic field therefore will suffice, near the Curie point, to magnetize the grains of an assemblage.

As in the case of the chemical magnetization, the grains become magnetized by a weak magnetic field on account of the decrease in coercivity of the grains—the reason for the decrease in the two cases being completely different, however.

In the T.R.M. case we are now concerned with the magnetic stability of the grains. As in the theory of the chemical magnetization, the grains will tend to demagnetize, with a relaxation time given by eqn. (1) if the field is removed; when it remains, however, the relaxation time is modified as before, and there tends to be a net moment in the direction of the ambient field. Again, as before, τ is primarily a function of v/T and in this case, magnetic stability of the given grains is achieved by allowing the temperature to fall below the Curie point and thus increasing the relaxation time. (In this case H_c and J_s also increase rapidly with decreasing temperature just below Curie point, thus helping to increase the effective τ-value.) Previously the stability was achieved by allowing

v to increase at constant T. The resultant effect, however, will be precisely the same in the two cases, and the properties of the magnetization produced should be the same for both chemical magnetization and thermal-remanent magnetization.

This has in fact been found to be the case. The chemical magnetization produced more resembles thermal remanent magnetization than it does isothermal remanence.

Summarizing this theoretical discussion: in both cases (T.R.M. and chemical magnetization), the coercivity of the material is reduced so that the grains become magnetized by weak fields of the order of 0·5 oersted; the reduced coercivity in one case being due to small particle size, and in the other to a decrease in saturation magnetization with temperature. Having become magnetized, magnetic stability is then achieved by increasing the effective grain size at constant temperature in the case of chemical magnetization, and decreasing the temperature at constant grain size in the case of T.R.M. In either instance, the effect is to increase the v/T ratio, which then rapidly increases the relaxation time of a given grain. Essentially, then, the two mechanisms are identical, and should lead to magnetizations of an identical nature. Whilst in the present experiments the two forms of magnetization have been found to be very similar, precise agreement has not been obtained. No doubt, under more carefully controlled conditions the two magnetizations would become even more alike.

The theory outlined here thus satisfactorily accounts for the experimental observations and conclusions embodied in fig. 12. Whether the chemical magnetization occurs over a small temperature range (225 to 300°C) or isothermally (e.g. at 350°C), the magnetization produced is very like thermal remanence from both the theoretical, and practical considerations.

§ 10. Applications in Rock Magnetism

This process of chemical magnetization is clearly one of great importance in rock magnetic studies where it is normally assumed, at least in the case of sediments, that any magnetization exhibited by the rock specimens is that formed at the time of sedimentation or shortly after. With igneous rocks the acquisition of the magnetization is a little different, but nevertheless such a process of chemical magnetization, during metamorphism, for instance, is a real possibility. We will now consider a few general aspects of the magnetization of sedimentary and igneous rocks in the light of this important magnetization process.

10.1.

Sedimentary rocks and their ferrimagnetic minerals have been extensively discussed by Nicholls (1955), particularly from the point of view of conditions of deposition and consolidation. In discussing the iron minerals present in sediments, Nicholls considers that chemically

precipitated ferric hydroxide may suffer dehydration either during compaction of the sediment or later, and give rise to the corresponding form of Fe_2O_3. Such dehydration probably proceeds in natural rocks at quite low temperatures and any remanent magnetization in the resulting ferric oxide mineral "will be essentially an isothermal remanent magnetization and probably unstable" (Nagata 1953, p. 109). Nicholls also concludes that ferruginous cements crystallizing at low temperatures will acquire "a kind of isothermal remanent magnetization in so far as they develop one at all". From the considerations of the formation of a magnetic phase during a chemical change, it would seem very likely that in sediments such a magnetization process would occur during the dehydration process. If this is so, then the form of the magnetization would be expected to be very different from the isothermal magnetization envisaged by Nicholls, and in fact be very like T.R.M. In the case of the New Red Sandstones, the thermal demagnetization curves obtained by Leng (a typical curve is shown in fig. 6) quite definitely resemble a T.R.M.-type magnetization rather than an I.R.M.-type. The present magnetization of these rocks, then, may be the result of chemical magnetization during the dehydration of an original hydrated ferric oxide—the thermal stability curves tending to support this. This dehydration of the original hydrated ferric oxide may be assisted by burial when, in the particular case of the Triassic sandstones, the temperature may be as high as 100°C (Clegg *et al.* 1954).

Thus, by applying the results of the chemical magnetization process to the dehydration of iron hydroxides in the formation of sedimentary rocks, it is possible to account for the T.R.M.-nature of the remanent magnetization of such sediments.

Chemical magnetization has been suggested by Doell (1956) and Martinez and Howell (1956), as a possible origin of the magnetization in some American sediments. An extensive investigation of the thermal stability of these rocks has not, however, been reported by the authors, so that it is impossible at the present time to make any direct comparison with the thermal stability of the British Triassic sandstones.

10.2.

In the case of the igneous rocks, chemical magnetization will only be important when the rock undergoes alteration—either chemical or thermal. Generally chemical alteration, unless complete, will not greatly affect the remanent magnetization of the rock. The principal alteration product of the strongly magnetic titanomagnetites is usually the very weakly magnetic hematite. However, thermal alteration may quite markedly alter the ferromagnetic properties of a titanomagnetite grain (Haigh 1957 c). For the time being, let us assume we have a homogeneous magnetic phase A (perhaps in a metastable state), which on heating to a temperature T_1 causes A to exsolve into two more-stable phases B and C, the Curie points of these being T_B and T_C, both higher

than T_1. Now, the initial process of exsolution will almost certainly be one of nucleation, strongly resembling the process investigated in the earlier sections of this paper, except that the nucleation in this case will take place inside a grain of the original phase A and not as a discrete separated grain. Clearly, then, it will be possible for this exsolved phase to become magnetized during its growth. Its direction of magnetization, however, will be determined not only by the magnetic field external to the grain but also by the local field inside the grain itself, which in all probability will be considerably stronger than the external field. It is therefore possible, and in fact very likely, that the exsolving phase will not only be magnetized, but will be magnetized in the opposite direction to the original magnetization of the grain. We thus have the basis for the formation of an antiparallel magnetization of the Néel type.

A process of this type may well be the origin of the reverse magnetization of such rocks as the well-known Haruna dacite —the reverse magnetization of this rock has been shown to be due to closely interleaved lamellae of minerals of the ilmenite–hematite series (Uyeda 1955). The point of importance here, however, is that exsolving minerals, or indeed any minerals forming by a nucleation process at temperatures well below their Curie point, can become strongly magnetized by weak fields of the order of the earth's field. This result is in marked contrast to the conclusions of Kawai (1956), who deduced, from considerations of the position of the solvus curve of a particular ferromagnetic system, that minerals exsolving at temperatures below their Curie points could not become strongly magnetized by an ambient field. Kawai concluded that the exsolved phases would not have a T.R.M.-type magnetization, but only a very much weaker I.R.M.-type of magnetization directly dependent upon the magnitude of the field in which they were situated.

§ 11. General Conclusions

In this paper it has been shown that it is possible for a ferromagnetic mineral to become strongly magnetized during a chemical change at temperatures well below its Curie point. Both the experimental and theoretical conclusions are that the magnetization resulting from such a change is of a thermal-remanent nature rather than like isothermal remanence. In the application to practical rock magnetism, this process of magnetization can be postulated as occurring in the formation of the magnetization of sediments—the nature of the magnetization of the Triassic sandstones in particular supporting this suggestion. In the case of igneous rocks, reversal properties of some specimens can possibly be explained in terms of a magnetization of this nature.

The possibility of a magnetization process similar to that described here, was first envisaged nearly twenty years ago by Koenigsberger (1938). He discussed the effect in connection with lattice changes in magnetite which result from possible unmixing of Fe_2O_3 at temperatures between 100° and 500°C, and seemed to conclude that this ' crystal-magnetization ',

as he called it, would not greatly influence the natural remanence of a rock specimen because of the random distribution of the ferromagnetic material. Whether such a process of exsolution could occur to any great extent in this particular iron-oxide system will not be discussed in the present paper but it does seem from the experiments described here that any changes in the mineral structure would lead to the production of a strong magnetization which would have a direction dependent upon the net ambient field at the time of the change. In the Addendum to Part II of his paper, however, Koenigsberger seems to subscribe to this view, when, in considering the formation of a sediment containing detrital magnetite from eroded older igneous rock, he suggests that the polarity of the beds may be acquired in the following way: "... after sedimentation under heavy pressures of deep water, or under special chemical conditions, (of say) oxidation or reduction, new iron minerals are formed and strong crystallization-remanence, due to the Earth's magnetic field, can arise in the magnetite during such a process". Certainly from the experiments described in this paper, of the chemical change $\gamma Fe_2O_3 \rightarrow Fe_3O_4$ in a field, provided it is carried to completion, there is no trace of any original magnetization.

Finally, it would seem desirable to differentiate between the magnetization exhibited by a crystal as a result of chemical alteration, and that acquired by a crystal during its growth—another extremely important but little studied process of magnetization. It might be preferable to call the former process 'chemical-magnetization', and the observed remanent magnetism 'chemical-remanence', whilst reserving the terms 'crystal-magnetization' and 'crystal-remanence' for the magnetization acquired by a crystal during its natural growth from either a melt, or more probably out of solution.

Acknowledgments

The author wishes to express his indebtedness to Professor P. M. S. Blackett, F.R.S. for his constant interest and advice throughout the course of this work.

He also wishes to thank Dr. M. Blackman of the Physics Department and Dr. E. P. Wohlfarth of the Mathematics Department of this College for helpful discussions on the theoretical aspects of the work described in this paper.

Finally, the author wishes to thank the Lancashire County Education Authority and the Department of Scientific and Industrial Research for grants enabling this research to be undertaken.

References

Becker, J. J., 1957, *J. Metals*, **9**, 59.
Clegg, J. A., Almond, M., and Stubbs, P. H. S., 1954, *Phil. Mag.*, 45, 583.
Doell, R. R., 1956, *Trans. Amer. geophys. Un.*, **37**, 156.
Haigh, G., 1957 a, *Phil. Mag.*, **2**, 505; 1957 b, *Ibid.*, **2**, 877; 1957 c, *Thesis*, University of London.

Kawai, N., 1956, *Proc. Jap. Acad.*, **42**, 464.
Koenigsberger, J. G., 1938, *Terr. Magn. atmos. Elect.*, **43**, 119, 299.
Kopelman, B., 1952, *Elect. Engr., N.Y.*, **71**, 447.
Leng, J. H., 1955, *Thesis*, University of London.
Martinez, J. D., and Howell, L. G., 1956, *Nature, Lond.*, **178**, 204.
Meiklejohn, W. H., 1953, *Rev. mod. Phys.*, **25**, 302.
Nagata, T., 1953, *Rock Magnetism* (Tokyo : Maruzen).
Néel, L., 1949, *Ann. Géophys.*, **5**, 90 ; 1955, *Advanc. Phys.*, **4**, 191.
Nicholls, G. D., 1955, *Advanc. Phys.*, **4**, 113.
Thellier, E., 1954, *C. R. Acad. Sci., Paris*, **239**, 1399.
Uyeda, S., 1955, *J. Geomagn. Geoelect., Kyoto*, **7**, 9.

Unloading Effects in the Plastic Properties of Copper Single Crystals†

By M. J. Makin
Metallurgy Division, A.E.R.E., Harwell

[Received December 9, 1957]

Abstract

Yield point phenomena occur on retesting copper single crystals during interrupted tensile deformation. The effect is observed only during the linear and parabolic regions of the stress–strain curve and the size of the yield drop is directly proportional to the reduction in stress on unloading. The ratio of the flow stress immediately before complete unloading to that on retesting is 0·986, and appears to be independent of temperature between −195°c and 100°c. The magnitude of the yield phenomenon at −195°c is markedly increased, however, by annealing at above −170°c, and this effect is independent of the amount of unloading.

An explanation of these phenomena is advanced in which Lomer–Cottrell sessile dislocations are formed during unloading, and that it is these dislocations which prevent large scale reverse plasticity. The increased effect at −195°c on annealing is interpreted in terms of the thermally activated reversal of the apices of these sessile dislocations.

§ 1. Introduction

The effect of certain variables, such as temperature or annealing treatment, on the tensile behaviour of metal single crystals has often been studied by straining specimens to a certain point, unloading, and then retesting after treatment, or under new conditions. The implicit assumption in these experiments is that the dislocation pattern within the specimen is the same at the start of the second extension as at the end of the first, i.e. that the process of unloading has an entirely reversible effect upon the dislocation pattern. Recently, however, experiments have indicated that this hypothesis is not correct and that unloading a strained single crystal does produce non-reversible changes in behaviour.

Haasen and Kelly (1957) have observed a yield point on retesting previously strained single crystals of aluminium and nickel at the same or lower temperatures than the initial deformation. The effect occurred only when the crystals were unloaded between tests, and no effect was found at low stresses. The phenomenon was independent of the time between unloading and retesting. The magnitude of the yield phenomenon was increased by annealing at 27°c between tests at −163°c and also by carrying out the second deformation at a lower temperature than the first. Haasen and Kelly attributed the effect to the re-arrangement of dislocations during unloading.

† Communicated by the Author.

The present work was undertaken to investigate the phenomenon further in copper single crystals, and, in particular, to determine the effect on the magnitude of the yield point of (*a*) partial unloading (*b*) annealing between tests and (*c*) the temperature of the second deformation.

§ 2. Experimental Method

Single crystals of copper 2·3 mm in diameter were prepared in a split graphite mould by the Bridgman technique from spectroscopically pure (99·999%) wire. A standard crystal orientation (fig. 1) was obtained

Fig. 1

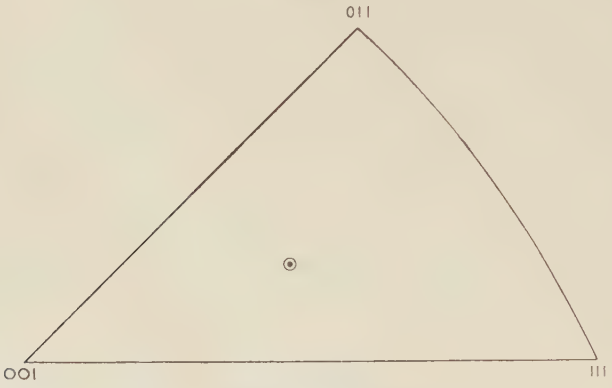

Initial orientation of specimen axis.

by seeding with a short length of suitable crystal. After growth, the crystals were cut into specimens about 5 cm long by warm nitric acid. The orientation of each crystal was checked by the Laue back-reflection method and all crystals with orientations differing by more than $\pm 1^\circ$ from the standard were rejected. Small copper loops were attached to the ends of the specimens by soft solder, water cooling being used to protect the rest of the crystal and the completed specimens were electropolished in a phosphoric acid cell immediately before testing.

Tensile tests were performed in a hard beam machine at a strain rate of 6×10^{-5} per sec. The load was determined to within 0·1% of the maximum value from the flexure of a spring steel beam and the strain was measured directly from the motion of the crosshead of the machine. Tests at the following temperatures were made by immersing the specimen in a liquid bath (table 1).

The temperature change when the specimen was exposed on changing baths was measured by a thermocouple mounted very close to the crystal. Particular care was taken to ensure that the specimen temperature did not change appreciably while the specimen was uncovered. A standard time of 15 min was allowed in each bath before a test was begun to ensure that the specimen and straining bars had taken up the temperature

of the bath. Unloading was accomplished by a reversal of the direction of rotation of the straining motor which allowed a smooth and progressive decrease in load to zero so avoiding effects due to a sudden release of load. In addition, it is also possible to unload partially and keep the specimens under the remainder of the load for an indefinite time.

Table 1. Details of Temperature Baths

Temperature °c	Bath	Fixing point
−195	Liquid N_2	Boiling point
−183	Liquid O_2	Boiling point
−158·5	Iso-pentane	Melting point
−119	Ethyl alcohol	Melting point
−77	Solid CO_2 and acetone	Sublimation point
−50 to −5	Acqueous $CaCl_2$	Freezing point
0	Ice	Melting point
20	Water	Room temperature
50 to 200	Silicone oil	Controlled to ±1°c

§ 3. Unloading Tests at Constant Temperature

Frequent unloading tests were first made at small strain increments during the whole of the stress–strain curve at various temperatures to determine the general nature of the effect, and particularly whether there was any gross alteration in the shape of the curve due to the unloading cycles. The stress–strain curve for one such test at −195°c compared with the curve for a continuously tested crystal is shown in fig. 2. The overall agreement between the two curves indicates that

Fig. 2

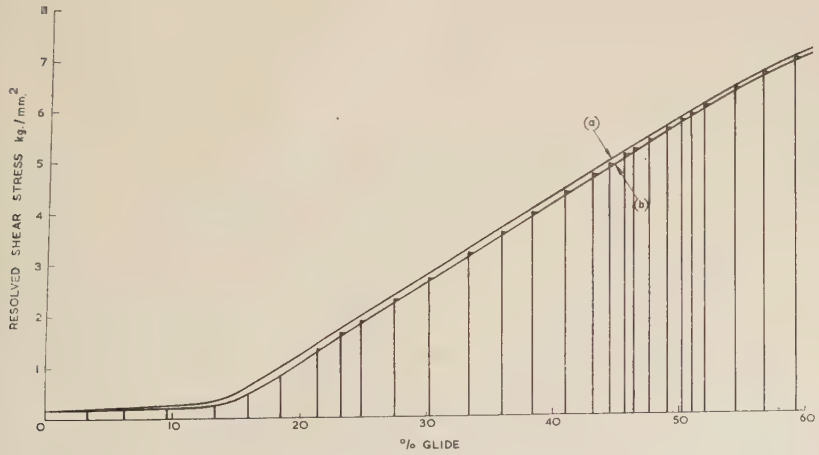

Stress–strain curves of crystals tested at −195°c, (*a*) continuous test, (*b*) interrupted test.

there are no gross effects due to repeated unloading, and this result has been verified at 20°c and at 100°c. Small yield points are observed, however, on retesting after unloading during the linear hardening and parabolic regions of the curve. The stress to resume plastic flow after unloading is initially greater than the flow stress immediately before unloading. On retesting, the initial rate of work hardening is either very low, giving a small region of constant stress, or is negative, giving a reduction in flow stress and a yield point, curve (*b*), fig. 3. One interesting point is that the curve subsequent to the yield point returns to the stress–strain curve expected from a continuation of the curve prior to unloading. These effects were observed at −195°, 20° and 100°c.

Fig. 3

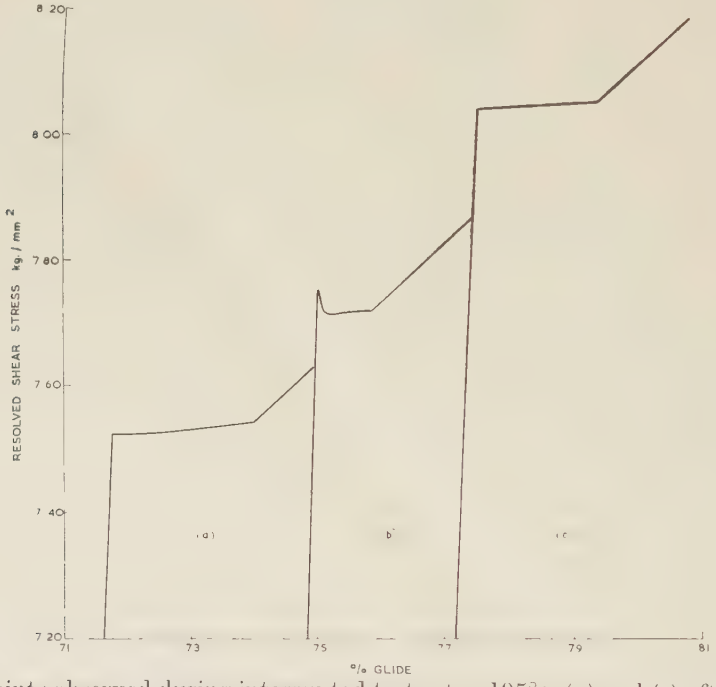

Yield points observed during interrupted tests at −195°c, (*a*) and (*c*) after intermediate annealing at 20°c, (*b*) no annealing.

No yield points were apparent on retesting during the first, easy glide, stage of deformation and experiments with a lighter spring steel beam were made to verify this point more accurately at −195°, 20° and 100°c. The transition region between the easy glide and linear hardening regions also did not show an appreciable effect at any of the testing temperatures.

Except at the beginning of the linear hardening region the magnitude of the yield drop appeared to be directly proportional to the flow stress (fig. 4).

Fig. 4

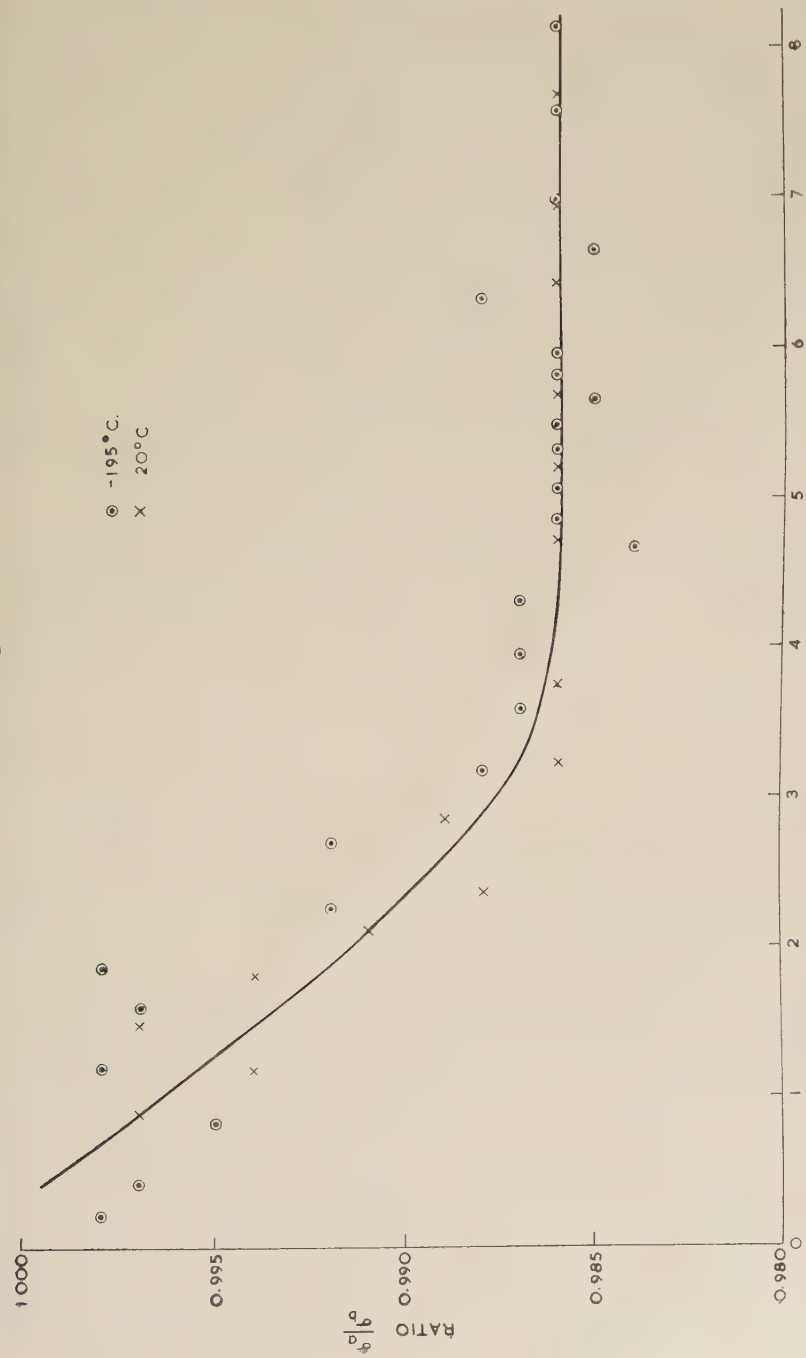

Ratio of flow stresses σ_a/σ_b as a function of σ_a for tests at −195°C and 20°C.

The ratio of the flow stress immediately before unloading σ_a, to that on retesting, σ_b, is also independent of the temperature of testing, a constant value of 0·986 being obtained at −195°, 20° and 100°C. The shape of the yield point is also not markedly different after unloading at various temperatures. No variation in the ratio with the time of ageing while the specimen was unloaded was observed between one minute and ten hours at −195°, 20° or 100°C. A standard time of ten minutes was used in the majority of the subsequent tests.

Fig. 5

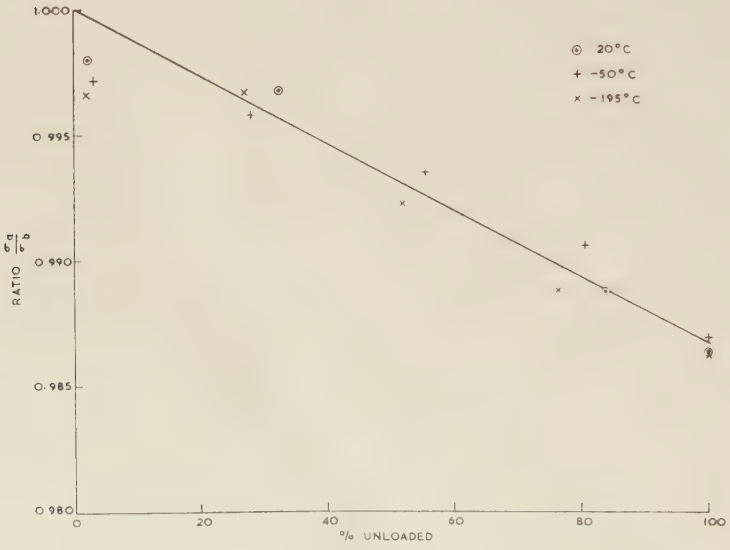

Ratio σ_a/σ_b as a function of the amount of unloading.

The connection between the yield point and unloading is revealed by experiments in which the amount of unloading between tests was varied from 0 to 100% (fig. 5). The ratio obtained is directly proportional to the amount of unloading between 0·996 after about 30% unloading and 0·986 after 100% unloading. There was no evidence of a limit to the effect before complete unloading of the specimen. The results with very small amounts of unloading are complicated by the relaxation in load due to transient creep in the specimen when the straining motor is stopped. This relaxation appears to have a greater effect on the ratio on retesting than the results after greater amounts of unloading would suggest. The linear relationship indicates that the size of the yield point is directly proportional to the reduction in stress during unloading. The flow stress on retesting is given by the relation :

$$\sigma_b = \sigma + \frac{\sigma_a - \sigma}{0{\cdot}986}$$

where σ_a=flow stress immediately before unloading, σ=stress during unloading time, and σ_b=initial flow stress on retesting.

A striking feature of these experiments is that the same linear relationship is obtained at different temperatures between -195° and 20°C.

The existence of a yield point phenomenon in solids is generally accompanied by a 'Luders band', in which a wave of plastic deformation passes along the specimen. To ascertain whether the present yield points were accompanied by a Luders band, the crystal was taken into either the linear or parabolic hardening region, unloaded, removed from the machine and the existing slip traces electropolished off. The specimen was then remounted in the machine and reloaded until just beyond the yield point, when it was again unloaded, removed from the machine, and examined microscopically. Typical slip traces observed on a specimen tested at 20°C are shown in fig. 6, Pl. 7. There was no evidence of a wave of deformation passing along the specimen after the initial yield drop, slip lines appearing in all regions of the specimen.

§ 4. Annealing between Unloading and Retesting

The effect on the size of the yield point of interposing an annealing treatment between unloading and retesting has been examined at a number of temperatures. In these experiments all the testing was

Fig. 7

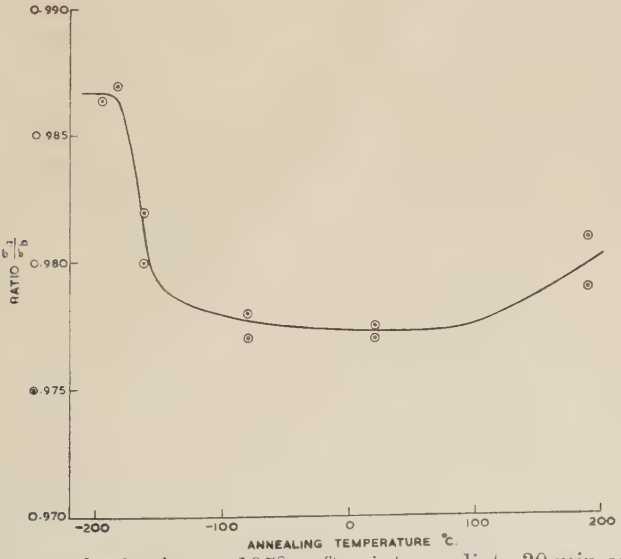

Ratio of σ_a/σ_b obtained at −195°C after intermediate 30 min anneals at higher temperatures.

performed at a constant temperature for each specimen and annealing was carried out by changing temperature baths after the specimen had been unloaded. A standard annealing time of half an hour was used.

One series of experiments was performed at a deformation temperature of −195°C (fig. 7). The ratio showed a large well-defined drop from 0·986

to 0·978 between −180° and −120°C and then it remained constant at 0·978 until temperatures in the region of 100°C were reached.

The shape of the yield point on retesting at −195°C is also markedly altered by annealing at above −120°C, fig. 3. The sharp drop in stress which occurs after no annealing is replaced by a much larger, almost horizontal, region in the stress–strain curve with no appreciable reduction in load at the start of the yield. After the constant stress region the curve returns to the stress–strain curve expected from a continuation of the curve obtained before unloading.

Table 2. Independence of the Ratio of σ_a/σ_b Tested at −195°C to the Time of Anneal at 20°C

Time of annealing at 20°C in hours	Ratio of stresses
$\frac{1}{2}$	0·977 (19 results)
5	0·978 (8 results)
17	0·977 (4 results)
47	0·977 (11 results)

Table 3. Ratio of σ_a/σ_b at −115°C after Annealing for 30 min at Various Temperatures

Temperature of 30 min anneal, °C	Ratio σ_a/σ_b
−78	0·984, 0·986
	0·987, 0·986
0	0·985, 0·989
	0·987, 0·987
50	0·984, 0·987
	0·986, 0·987

Table 4. Effect of Stress on Ratio σ_a/σ_b at −195°C after Annealing for 30 min at −78°C

Stress kg/mm²	Ratio σ_a/σ_b
2·89	0·983
3·33	0·976
3·52	0·979
3·75	0·976
4·30	0·978
5·19	0·978
6·11	0·977

The ratio σ_a/σ_b is not dependent upon the time of annealing, table 2. This behaviour was also observed on annealing in the region of rapid decrease of ratio between −180° and 120°C. Similarly, if the deformation experiments were carried out at above −120°C annealing treatments at higher (or lower) temperatures had no effect on the ratio σ_a/σ_b, table 3.

The reduced ratio at −195°C after annealing at above −120°C was still independent of the actual value of the flow stress, table 4, indicating the greater significance of the ratio σ_a/σ_b than the actual value of $\Delta\sigma$, the increase in flow stress on retesting.

The experimental evidence is therefore most unusual and surprising. The ratio obtained on retesting after complete unloading with no annealing treatment interposed is constant at 0·986 throughout the temperature range in which the decrease in ratio appears in the annealing experiments. Hence the effect of the process which occurs during annealing is apparent only if the second deformation is carried out below −120°C and is not visible at higher temperatures. This behaviour suggests that the important parameter is the temperature at which the second deformation is carried out, in marked contrast to such phenomena as impurity yield points, where the important characteristic is the annealing treatment necessary to deposit the impurity on the dislocations. Once the dislocations are locked, point effects are observed over a wide range of testing temperatures.

Table 5. Effect of % Unloading on the Ratio of σ_a/σ_b Obtained at −195°C after Annealing for 30 min at −78°C

% Unloading			
	10%	50%	100%
	0·977	0·977	0·983
	0·977	0·981	0·976
	—	0·981	0·979
	—	0·982	0·976
	—	0·978	0·978
	—	0·978	0·978
	—	—	0·977
Average values	0·977	0·980	0·978

Since the size of the yield point observed on retesting with no annealing treatment is directly proportional to the amount of unloading it is interesting to examine the unloading dependence of the large effect observed at −195°C after annealing treatments above −180°C. The experiment with no unloading between deformations is not possible as further plastic flow would occur when the temperature was raised for the annealing due to the decrease in flow stress with increasing temperature. The flow stress is proportional to the shear modulus of the material, which decreases with increasing temperature. This change in shear modulus suggests that the minimum safe decrease in load at −195°C to permit an annealing experiment at −78°C is 10%. The ratio obtained on first and second testing at −195°C with intermediate annealing at −78°C was measured after 10, 50 and 100% unloading. The results, table 5, show that the amount of unloading has no significant effect on the ratio σ_a/σ_b, the maximum yield point occurring after only 10% unloading. This behaviour is in marked contrast to the direct proportionality between the ratio σ_a/σ_b and the amount of unloading in tests with no annealing. The procedure adopted

in the annealing tests had no effect upon the results. The two procedures tested were (i) to unload partially and then anneal and (ii) to unload completely, reload partially and then anneal. When the annealing temperature is either −183° or −159°c the amount of unloading does have a significant effect, however, lower ratios being obtained with more unloading. This is shown in table 6, in the case of annealing at −159°c. This temperature is approximately halfway down the steep drop in the σ_a/σ_b versus temperature of annealing curve, fig. 7, and the behaviour of specimens annealed at this temperature between tests at −195°c is midway between the extremes represented by the proportionality with unloading with no annealing and the independence of the ratio σ_a/σ_b after annealing at above −120°c. Although the ratios at −159°c are dependent upon the degree of unloading, they are lower than those obtained with no annealing, as is illustrated in table 6.

Table 6. Effect of % Unloading on the Ratio of σ_a/σ_b at −195°c with Intermediate 30 min Anneals at −159°c

% Unloading			
	10%	50%	100%
	0·994	0·990	0·979
	0·990	0·988	0·983
	0·994	0·991	0·984
	—	0·988	0·981
	—	0·988	0·981
Average values	0·993	0·989	0·981
No annealing	0·999	0·993	0·986

These effects were not observed in specimens tested above −120°c and annealed at higher or lower temperatures. In this case the behaviour was exactly the same as for unannealed specimens tested at the same temperature, see fig. 5. This was checked at −78°, −20° and +20°c.

§ 5. Retesting at a Different Temperature from Unloading

By unloading crystals at one temperature and retesting at a different temperature, the effect of temperature on the nature of the yield point introduced during unloading can be examined. The situation is complicated by the reversible change in flow stress which occurs on changing the testing temperature but if allowance is made for this by extrapolating back the stress-strain curve on retesting to zero extension then the size of the yield point effect can be measured. A crystal was retested at a series of temperatures between 100°c and −78°c after a standard treatment of unloading after deformation at 20°c. The ratio of the stress on

unloading to that on retesting at lower temperatures, table 7, was only slightly less than the ratio obtained on retesting at 20°c, 0·986, and did not show any marked temperature dependence between 20° and −78°c. The proportionality with the flow stress was fully maintained. This result implies that the process responsible for the yield point effect does not, in this temperature range, depend upon thermal activation. If the crystal is retested at −195°c, however, then a much larger yield point and consequently smaller ratio is obtained due to the additional effect described previously which occurs between −180° and −120°c. Similar results have been obtained after unloading at −78°c.

Table 7. Effect of Retesting Temperature on the Ratio σ_a/σ_b after Unloading at 20°c. The Reversible Temperature Dependence in Flow Stress has been allowed for

Temp. °c	Ratio
−78	0·986, 0·983
−60	0·986, 0·982 0·988, 0·982
−51	0·983, 0·984
0	0·985, 0·986

On retesting at temperatures higher than 20°c, however, the yield point rapidly becomes smaller in size and at about 35°c disappears completely, the yield being quite smooth. This behaviour has also been observed after unloading at various temperatures between −195° to +200°c. In heavily deformed crystals retested at higher temperatures a yield point phenomenon reappears due to work softening, as described by Stokes and Cottrell (1954) and Cottrell and Stokes (1955). The effects described here occur at all stages of the linear and parabolic hardening regions of the stress–strain curve.

The experimental evidence is, therefore, that the magnitude of the yield point introduced by unloading at a constant temperature is insensitive to the temperature of retesting if this is a lower temperature. No yield point is observable, however, on retesting at temperatures more than a few degrees higher than the unloading temperature.

§ 6. Discussion

6.1. *Yield Point Effects*

Two main types of explanation of the yield point phenomena produced on retesting after unloading are possible. The first is that the effect is due to strain ageing and locking of dislocations by a defect or impurity released during deformation. This explanation has been advanced by

Blewitt (1953) and also by Noggle (1955) to explain yield points introduced into copper single crystals deformed at −195°c with intermediate annealing at room temperature. On this theory vacancies are produced during deformation which migrate to the dislocations during the annealing so producing the yield point. Cupp and Chalmers (1954) attribute delayed yielding in copper single crystals either to a substitutional solute or to hydrogen present as an impurity. The strain ageing and impurity hypotheses do not agree with the experimental facts very satisfactorily, however. The insensitivity of the effect to the unloading temperature and the dependence upon the degree of unloading rather than upon the time which elapses between tests argues strongly against a diffusion process.

An alternative explanation is based upon dislocation–dislocation interactions, rather than dislocation–point defect interactions. A basic problem facing all theories of work hardening is to explain why the large numbers of dislocations piled up against barriers during the deformation do not completely relax when the applied stress is removed, giving large reverse plastic deformation. Obviously some locking process occurs during unloading which prevents large scale running back of the dislocations and it seems probable that it is this locking process which results in the formation of a yield point on retesting. The absence of the effect during the easy glide stage of the deformation suggests that the process is associated with the motion of dislocations on intersecting slip planes. The formation of yield points during the linear part of the stress–strain curve as well as the parabolic region indicates that the effect is independent of the surmounting of obstacles by cross-slip, the process now thought to be responsible for the change from linear to parabolic hardening (Seeger *et al.* 1957).

In Friedel's (1955) theory of linear work hardening all sources of dislocations capable of forming Lomer–Cottrell sessile dislocations are used to form the edges of the slipped region surrounding each dislocation source in the active system. On this model the size of the slipped region is therefore limited by the number of active slip sources and in a well annealed single crystal may be of the order of 10^{-4} cm in diameter. Experimental evidence suggests, however, that the slipped regions formed during linear hardening are initially of the order of 10^{-2} cm in diameter, decreasing in size with increasing deformation. Not all the possible sessile dislocations have been formed therefore, and hence the formation during unloading of new sessile dislocations between the active slip system and intersecting systems is possible. These new sessile dislocations prevent the dislocations in the active system running back and, because energy is released during their formation (Stroh 1956) a larger stress than the one under which they were formed is required to dissociate them. On this model it is expected that the curve after the yield point should return to a continuation of that before, since when the sessile dislocations formed during unloading have been dissociated, the dislocation arrangement returns essentially to that previous to unloading.

To understand the proportionality between the size of the yield point and the flow stress it is necessary to consider the effect of unloading in more detail. As the load is progressively removed the dislocations piled up against the sessile dislocations forming the perimeter of the slipped region begin to run back towards the centre of the region. As they move back there is a chance that they will attract a dislocation in an intersecting system which will combine with one of the dislocations in the active system to form a short length of new sessile dislocation. On further unloading this new sessile dislocation resists the running back of more dislocations until the pressure on it is so great that it dissociates. When this occurs further running back takes place with the formation of other lengths of new sessile dislocation. This process continues until unloading is stopped, either at zero stress or at some intermediate value. At this stage the specimen contains a distribution of new sessile dislocations which are just able to resist the back pressure of the groups of mobile dislocations caught behind them. The total strength of the new sessiles formed on unloading is therefore of necessity approximately proportional to the back stress, since if they were too weak dissociation would occur with further relaxation of mobile dislocations and the formation of more new sessile dislocations until the balance was redressed. Hence the strength of the array of sessile dislocations formed on unloading is proportional to the amount of unloading. The size of yield point obtained on retesting is therefore proportional to the amount of unloading.

The greatly increased yield effect obtained at $-195°$C after annealing between tests at above $-120°$C may be due to the reversal of the apices of the sessile dislocations formed during unloading. Stroh has discussed the strength of the Lomer–Cottrell sessile dislocation and has shown that in copper the stacking fault separating two partial dislocations is so wide that the possibility of the dislocations forming the sessile group recombining and gliding on the (001) plane is negligible. Break-up can occur only by dissociation into the two dislocations from which the sessile was originally formed. This process occurs more easily if the apex of the sessile points in the opposite direction to the stress. In fig. 8, DB is the active slip plane and during plastic deformation a piled up group of dislocations has formed behind a sessile dislocation at B. During unloading one of the dislocations in the group has combined with a dislocation on the plane AC forming a new sessile in configuration (*a*). Since the activation energy is small sufficient thermal energy is available above $-120°$C to enable the sessile dislocation to reverse in direction under the back stress to configuration (*b*) in fig. 8; below $-180°$C reversal does not occur. On reloading, dissociation can occur only from position (*a*). During interrupted test at $-195°$C no reversal occurs and the ratio of flow stress before unloading to that after is 0·986. If an annealing treatment above $-120°$C is interposed, however, then the new sessile dislocations reverse to position (*b*) and on retesting at $-195°$C sufficient stress must be applied to reverse the sessile to position (*a*) before dissociation can occur, and consequently a high yield point and low

ratio, 0·977 is obtained. If the whole experiment is carried out above −120°c, however, then although the sessile reverses during unloading sufficient thermal energy is available to enable position (*a*) to be regained before dissociation occurs and hence the ratio of flow stress before to after unloading is the same as that observed during tests at −195°c in the absence of annealing, i.e. 0·986, as has been found experimentally.

Fig. 8

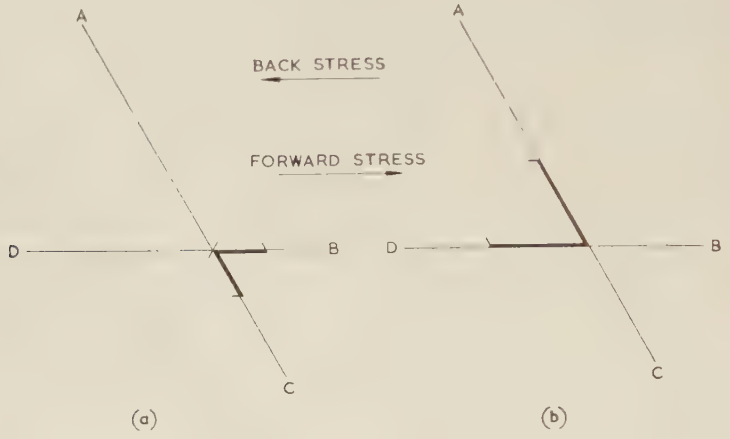

Sessile with apex (*a*) on the direction of the back stress and (*b*) in the direction of the forward stress.

In general it is reasonable to suppose that any arrangement of sessile dislocations formed during unloading which give a yield point on retesting at the same temperature will also give yield phenomena when retested at lower temperatures, and this is observed experimentally. When retested at higher temperatures the probability of thermally activated dissociation of the sessile dislocation increases and the observed effect decreases. The sensitivity of the dissociation to thermal activation is greatly increased by the fact that the sessile is under a high stress tending to dissociate it when the macroscopic stress is close to the yield stress. A comparatively small increase in thermal fluctuations is, therefore, capable of dissociating the sessile dislocation and the yield point disappears. The sessile dislocations appear to be sensitive to temperature only at temperatures above that at which the sessiles were formed, however, as the yield point on retesting at lower temperatures is independent of temperature.

The change in the nature of the yield point at −195°c from a sharp yield drop on immediate retesting to a plateau type yield after intermediate annealing at above −120°c may be associated with the ability of rapidly moving dislocations recently freed by the unlocking of some sessiles to unlock sessiles in another part of the crystal. The plateau

type of yield observed in crystals annealed between tests at −195°c indicates that sessiles in configuration (*b*) fig. 8 are more resistant to this unlocking than those in configuration (*a*) at −195°c. At higher testing temperatures, where reversal of configurations can occur under thermal activation yield drops are again observed. Microscopic examination of specimens immediately after the yield drop at 20°c and on the plateau region after testing at −195°c with intermediate annealing did not reveal any marked Luders band phenomenon, however, slip traces being observed in all parts of the specimen.

One point for which no entirely satisfactory explanation is available is the insensitivity of the yield point to the amount of unloading between tests at −195°c with intermediate annealing at above −120°c. During annealing the sessiles reverse from configuration (*a*) to (*b*) and break, allowing further running back with the formation of more new sessiles even when the load is not completely removed. If this effect is large then the dependence upon the degree of unloading would be markedly reduced.

Acknowledgments

It is a great pleasure to thank both Dr. A. H. Cottrell and Dr. H. M. Finniston for their interest and encouragement.

References

Blewitt, T. H., 1953, *Phys. Rev.*, **91**, 1115.
Cottrell, A. H., and Stokes, R. J., 1955, *Proc. roy. Soc.* A, **233**, 17.
Cupp, C. R., and Chalmers, B., 1954, *Acta Met.*, **2**, 803.
Friedel, J., 1955, *Phil. Mag.*, **46**, 1169.
Haasen, P., and Kelly, A., 1957, *Acta. Met.*, **5**, 192.
Noggle, T. S., 1955, *Ph.D. Thesis*, Illinois.
Seeger, A., Diehl, J., Mader, S., and Rebstock, H., 1957, *Phil. Mag.*, **2**, 323.
Stroh, A. N., 1956, *Phil. Mag.*, **1**, 489.
Stokes, R. J., and Cottrell, A. H., 1954 *Acta. Met.*, **2**, 341.

Correlations in the Charge Density of a Classical Plasma†

By S. F. Edwards
Department of Mathematical Physics, University of Birmingham

[Received November 23, 1957]

Abstract

The charge density of a plasma can be described by the coefficients of its Fourier decomposition. The time correlation of these is calculated in this paper for arbitrary wavelength. The form of the correlation function then varies from that expected from wave motion at long wavelengths, to random perfect gas motion at short wavelengths, and bridges the gap between random short range motion and ordered long range effect.

§ 1. Introduction

A Fully ionized gas has collective and individual particle motions. The charge distribution in such a plasma will be affected by both motions; in particular the correlation between the charge density at some point and the charge density at any subsequent time will involve both effects. Rather than consider the density at a point, it is convenient to consider its Fourier transform $\rho_{\mathbf{k}}$, and this paper is concerned with calculating the correlation function

$$C(t)=\langle \rho_{\mathbf{k}}(0)\rho_{\mathbf{k}}^*(t)\rangle, \quad . \quad . \quad . \quad . \quad . \quad . \quad . \quad (1)$$

without any restriction upon the value of $\mathbf{k}$, i.e. for wavelengths ranging from the distance between particles to the size of the whole plasma. This is done for thermal equilibrium and avoids therefore the many difficulties of truly excited plasma oscillations (see for example, Van Kampen 1957). The knowledge of $C(t)$ is valuable firstly because it is an observable quantity, and secondly because it enables one to calculate the plasma frequency accurately, thermal equilibrium being a well defined state with standard methods of calculation.

To illustrate $C(t)$ consider two extreme cases, an assembly of harmonic oscillators, and a perfect gas. For the assembly of oscillators with energy

$$H=\tfrac{1}{2}\sum_j (m\dot{\rho}_j^2+m\omega^2\rho_j^2), \quad . \quad . \quad . \quad . \quad . \quad . \quad (2)$$

$$\rho_j(t)=\rho_j(0)\cos\omega t+\dot{\rho}_j(0)\sin\omega t. \quad . \quad . \quad . \quad . \quad . \quad (3)$$

Hence

$$\langle \rho_j(0)\rho_j(t)\rangle=\langle \rho_j(0)\rho_j(0)\rangle\cos\omega t+\langle \rho_j(0)\dot{\rho}_j(0)\rangle\sin\omega t \quad . \quad . \quad (4)$$

$$=\langle \rho_j(0)\rho_j(0)\rangle\cos\omega t, \quad . \quad . \quad . \quad . \quad . \quad . \quad . \quad . \quad (5)$$

† Communicated by Professor R. E. Peierls, C.B.E., F.R.S. Work partly done whilst consultant at A.E.R.E., Harwell.

since in thermal equilibrium the mean value $\langle \rho_j(0)\dot{\rho}_j(0)\rangle$ vanishes, being odd in the time. So in this case $C'(t)/C'(0)$ oscillates with the frequency ω of the oscillators. For the perfect gas

$$H=\tfrac{1}{2}\sum m v_k^2 \qquad \ldots\ldots\ldots \quad (6)$$

and the density

$$\rho_{\mathbf{k}}=\sum_l \exp(i\mathbf{k}\cdot\mathbf{r}_l). \qquad \ldots\ldots\ldots \quad (7)$$

The equations of motion of the particles are

$$\dot{\mathbf{r}}_l=\mathbf{v}_l, \quad \dot{\mathbf{v}}_l=0 \qquad \ldots\ldots\ldots \quad (8)$$

so that

$$\rho_{\mathbf{k}}(t)=\sum_l \exp(i\mathbf{k}\,.\,\mathbf{r}_l+i\mathbf{k}\,.\,\mathbf{v}_l t), \qquad \ldots\ldots \quad (9)$$

and

$$\langle \rho_{\mathbf{k}}(0)\rho_{\mathbf{k}}{}^*(t)\rangle=\langle \rho_{\mathbf{k}}(0)\rho_{\mathbf{k}}{}^*(0)\rangle \exp(-\mathbf{k}^2t^2\kappa T/2m), \qquad \ldots \quad (10)$$

the latter factor being

$$\int \exp(i\mathbf{k}\cdot\mathbf{v}_l t)\exp(-\tfrac{1}{2}\textstyle\sum mv^2/\kappa T)\Pi\, dv \Big/ \int \exp(-\tfrac{1}{2}\sum mv^2/\kappa T)\Pi\, dv. \qquad (11)$$

This factor shows that any random increase of density will disappear with lifetime $(2m,\kappa T)^{1/2}(\mathbf{k}^2)^{-1/2}$ due to the random particle motions.

The plasma shows signs of both these behaviours and $C(t)/C(0)$ can be expected to resemble both the above models. If it showed both behaviours independently one could expect

$$C(t)=C(0)\cos\omega t \exp(-\mathbf{k}^2t^2kT/2m), \qquad \ldots \quad (12)$$

with ω the plasma frequency, and it is with this form in mind that the general problem will be tackled.

§ 2. Calculation

The two examples in the introduction could be solved because it was possible to solve the equations of motion, and write $\rho(t)$ in terms of $\rho(0)$. This is not possible in the general case of a system with Hamiltonian

$$\tfrac{1}{2}\sum m v_i^2+e^2\sum_{i>j}(1/r_{ij}). \qquad \ldots\ldots \quad (13)$$

(For simplicity electrons with a uniform neutralizing background will be considered here.) What is possible is to calculate the derivatives of the $\rho_{\mathbf{k}}$ at $t=0$: $\dot{\rho}_{\mathbf{k}}(0)$, $\ddot{\rho}_{\mathbf{k}}(0)$, ... by applying

$$m\dot{\mathbf{v}}_i+e^2\sum(\mathbf{r}_j-\mathbf{r}_i)|\mathbf{r}_i-\mathbf{r}_j|^{-3}=0, \quad \dot{\mathbf{r}}_i=\mathbf{v}_i. \qquad \ldots \quad (14)$$

Thus, it is possible to get

$$\begin{aligned} C(t)&=\langle \rho_{\mathbf{k}}{}^*(0)\rho_{\mathbf{k}}(t)\rangle \\ &=\langle \rho_{\mathbf{k}}{}^*(0)\rho_{\mathbf{k}}(0)\rangle+t\langle \rho_{\mathbf{k}}{}^*(0)\dot{\rho}_{\mathbf{k}}(0)\rangle+t^2/2\langle \rho_{\mathbf{k}}{}^*(0)\ddot{\rho}_{\mathbf{k}}(0)\rangle \\ &\quad +t^3/6\langle \rho_{\mathbf{k}}{}^*(0)\dddot{\rho}_{\mathbf{k}}(0)\rangle+t^4/24\langle \rho_{\mathbf{k}}{}^*(0)\rho_{\mathbf{k}}{}^{\mathrm{IV}}(0)\rangle+\ldots. \end{aligned} \qquad (15)$$

The expectation values of the odd derivatives clearly vanish and so $C(t)$ can be written

$$C(t)=C(0)+\tfrac{1}{2}t^2\ddot{C}(0)+\tfrac{1}{24}t^4C^{IV}(0)+\ldots \quad (16)$$

These quantities will be calculated below and it will appear at once that one is reproducing the product of the two models given earlier. In other words if $C(t)$ is written

$$C(t)=\tfrac{1}{2}C(0)[\exp(i\sqrt{at}-bt^2+ic^{3/2}t^3-\ldots)$$
$$+\exp(-i\sqrt{at}-bt^2-ic^{3/2}t^3-\ldots)] \quad (17)$$

the terms $a, b, c, \ldots$ are a rapidly decreasing sequence for all $\mathbf{k}$ and can be fitted by comparing this form with (16):

$$C(t)=C(0)\left[1-(\tfrac{1}{2}a+b)t^2+\left(\frac{a^2}{24}+\frac{ab}{2}+\frac{b^2}{2}-\sqrt{(ac^3)}\right)t^4\ldots\right]. \quad (18)$$

Consider $\ddot{C}(0)$: (henceforward $\rho_{\mathbf{k}}$ means $\rho_{\mathbf{k}}(0)$)

$$\dot{\rho}_{\mathbf{k}}=\sum_l i(\mathbf{k}\cdot\mathbf{v}_l)\exp i\mathbf{k}\cdot\mathbf{r}_l \quad (19)$$

$$\ddot{\rho}_{\mathbf{k}}=\sum_l -(\mathbf{k}\cdot\mathbf{v}_l)^2\exp i\mathbf{k}\cdot\mathbf{r}_l+\sum i(\mathbf{k}\cdot\dot{\mathbf{v}}_l)\exp i\mathbf{k}\cdot\mathbf{r}_l$$
$$=-\sum(\mathbf{k}\cdot\mathbf{v}_l)^2\exp i\mathbf{k}\cdot\mathbf{r}_l+(e^2/2\pi^2)\sum_{\mathbf{j}\neq 0}(\mathbf{k}\cdot\mathbf{j})/\mathbf{j}^2)\rho_{\mathbf{k}+\mathbf{j}}\rho_{\mathbf{j}}^*. \quad (20)$$

Hence

$$\langle\rho_{\mathbf{k}}^*\ddot{\rho}_{\mathbf{k}}\rangle=-\tfrac{1}{2}\mathbf{k}^2(2\kappa T/m)\langle\rho_{\mathbf{k}}^*\rho_{\mathbf{k}}\rangle+(4\pi e^2)/(mR^3)\sum(\mathbf{k}\cdot\mathbf{j})(\mathbf{j}^2)\langle\rho_{\mathbf{k}}^*\rho_{\mathbf{k}+\mathbf{j}}\rho_{\mathbf{j}}\rangle. \quad (21)$$

(R is the side of the box in which the Fourier analysis takes place, R^3 is the volume.) The latter sum vanishes, being odd in ρ whilst the Hamiltonian is even, except for $\mathbf{k}+\mathbf{j}=0$, ρ_0 being an absolute constant N. So we get

$$\langle\rho_{\mathbf{k}}^*\ddot{\rho}_{\mathbf{k}}\rangle=[-k^2(\kappa T/m)+(4\pi e^2N/mR^3)]\langle\rho_{\mathbf{k}}^*\rho_{\mathbf{k}}\rangle. \quad (22)$$

It is convenient to express this result in terms of the wavelength λ, $\lambda^2=(\mathbf{k}^2)^{-1}$, and by a frequency ω, a length r_0 and a wavelength λ_D, which are defined by

$$\lambda_D^2=(\kappa TR^3)/(4\pi e^2N),$$
$$\omega^2=4\pi e^2N/(mR^3),$$
$$r_0^3N=R^3.$$

Then

$$\langle\rho_{\mathbf{k}}^*\ddot{\rho}_{\mathbf{k}}\rangle=-(\omega^2+\lambda_D^2\lambda^{-2}\omega^2)\langle\rho_{\mathbf{k}}^*\rho_{\mathbf{k}}\rangle. \quad (23)$$

The term $\mathbf{k}^2/\kappa T/2m)$ is just the free particle motion term, whilst the $4\pi e^2N/mR^3$ is well known as the plasma frequency. If e^2 is zero the expansion is just that of the perfect gas; if $\mathbf{k}^2$, or T, is zero, then in the light of subsequent terms in the development, ω can be regarded as the oscillator frequency. It would of course be quite incorrect to regard $\omega(1+\lambda_D^2\lambda^{-2})^{1/2}$ as either an effective frequency or an effective inverse lifetime. That only the term with $\mathbf{k}+\mathbf{j}=0$ need be included in the sum

in (21) is often assumed in problems in which plasma oscillations are excited above the thermal level, and is there known as the random phase approximation.

The next non-vanishing derivative is the fourth, and a knowledge of it and of the second derivative, with the assumption that c is small, is sufficient to determine a, b of (17). The terms obtained contain those corresponding to oscillators and individual motion alone and also cross terms. Writing $\mathbf{k}^2(\kappa T/2m)=\sigma^2$ one obtains

$$\langle \rho_{\mathbf{k}}^* \rho_{\mathbf{k}}^{\mathrm{IV}} \rangle = (12\sigma^4+\omega^4+8\sigma^2\omega^2)\langle \rho_{\mathbf{k}}^* \rho_{\mathbf{k}} \rangle - (\omega^4/3N^2) \sum_{\mathbf{j}} (1+3\mathbf{k}^2/\mathbf{j}^2)\{\langle \rho_{\mathbf{k}} \rho_{\mathbf{k}}^* \rho_{\mathbf{j}} \rho_{\mathbf{j}}^* \rangle - N\langle \rho_{\mathbf{k}} \rho_{\mathbf{k}}^* \rangle\}. \quad (24)$$

If the latter term is called $3N^2\theta$, then a, b are determined from

$$a+2b=\omega^2+2\sigma^2 \quad . \quad . \quad . \quad . \quad . \quad . \quad . \quad (25)$$

$$a^2+12ab+12b^2=\omega^4+12\sigma^2+8\sigma^2\omega^2-\omega^4\theta. \quad . \quad . \quad . \quad (26)$$

It is only at this point, in the evaluation of θ, that one requires the explicit nature of the partition function. If this is now written as $\exp[-(\phi_s+\phi_l)/\kappa T]$ where ϕ_s and ϕ_l are short and long range potentials (see for example Bohm and Pines 1952, Edwards 1958), i.e.

$$\phi_s \sim \sum e^2 \exp(-r_{ij}/h)/r_{ij}, \quad \phi_s+\phi_l=e^2\sum(1/r_{ij})$$

with $h \sim \lambda_D$, then it is found by a straightforward calculation that to high accuracy $\langle \rho_{\mathbf{k}} \rho_{\mathbf{k}}^* \rho_{\mathbf{j}} \rho_{\mathbf{j}}^* \rangle = \langle \rho_{\mathbf{k}} \rho_{\mathbf{k}}^* \rangle \langle \rho_{\mathbf{j}} \rho_{\mathbf{j}}^* \rangle$ and that θ has the form $\gamma r_0^{\,3}\lambda_D^{\,-3}+\mu r_0^{\,3}\lambda_D^{\,-1}\lambda^{-2}$ where γ, μ are numerical constants of order unity. Thus both of these terms are small, the former being of order 10^{-3} for a gas of density 10^{-12}, and the latter less. So a, b are to be determined from

$$a+2b=\omega^2+2\sigma^2 \quad . \quad . \quad . \quad . \quad . \quad . \quad (27)$$

$$a^2+12ab+12b^2=\omega^4+8\sigma^2\omega^2+12\sigma^4. \quad . \quad . \quad . \quad . \quad (28)$$

These equations have the solution

$$a^2=2\sigma^2\omega^2+\omega^4$$

$$b=\sigma^2+(\omega^2-\sqrt{(\omega^4+2\sigma\omega^2)})/2. \quad . \quad . \quad . \quad . \quad . \quad (29)$$

If $\omega \gg \sigma$ then

$$a=\omega^2+\sigma^2, \quad b=\sigma^2/2. \quad . \quad . \quad . \quad . \quad . \quad (30)$$

Thus the effective plasma frequency is

$$\omega_{\mathrm{eff}}^{\,2}=\omega^2+\mathbf{k}^2(\kappa T/m) \quad . \quad . \quad . \quad . \quad . \quad . \quad (31)$$

and the lifetime is

$$\sqrt{2}/\sigma=\sqrt{2}(\mathbf{k}^2\kappa T/2m)^{1/2} \quad . \quad . \quad . \quad . \quad . \quad (32)$$

which is increased by a factor $\sqrt{2}$ from the free particle case. If $C(t)$ corresponding to (17) and (30) is Fourier transformed to give the spectral distribution:

$$\tfrac{1}{2}(\pi b^{-1})^{1/2}\{\exp[-(\nu-\sqrt{a})^2/4b]+\exp[-(\nu+\sqrt{a})^2/4b]\} \quad (33)$$

$$\simeq(\pi/2\sigma)^{1/2}\{\exp[-(\nu-\omega-\sigma^2/2\omega)^2/2\sigma^2] + \exp[-(\nu+\omega+\sigma^2/2)^2/2\sigma^2]\} \quad . \quad . \quad . \quad (34)$$

one finds a distribution about $\pm(\omega+\sigma^2/2\omega)$ of width $\sqrt{2}\sigma$. The displacement in the frequency is therefore not significant compared with the width for the case under consideration $\omega \gg \sigma$. The value of ω_{eff} agrees with that given for plasma waves by Thomson and Thomson (1933). Their derivation can be expected to apply to the present problem since it is for isothermally propagated waves, as has been pointed out by Van Kampen (1957).

The other extreme case is when $\sigma \gg \omega$, corresponding to wavelenths shorter than the Debye–Huckel radius λ_D. Then

$$b=\sigma-\sqrt{2\sigma\omega}, \quad a^2=2\sigma^2\omega^2 \qquad . \; . \; . \; . \; . \; . \; (35)$$

and the spectral distribution is rather broader than the free particle gaussian having its maximum slightly separated into two. One can see that the general solution (34) starts, as ω varies from large to small compared with σ, with two well defined peaks at $\nu=\pm\omega$ and the two peaks move towards the origin $\nu=0$ until they coalesce into the free particle single peak. The final peak has $\sqrt{2}$ time the width of either of the plasma oscillation peaks.

Acknowledgments

Part of this work was done at A.E.R.E., Harwell in the summer of 1957, and the author is pleased to acknowledge the hospitality of the Theoretical Physics Division, and valuable conversations with Drs. J. Hubbard, J. Hamilton and W. B. Thompson. I should also like to thank Professor Peierls for his comments on this work.

References

Bohm, D., and Pines, D., 1952, *Phys. Rev.*, **85,** 338.
Edwards, S. F., 1958, *Phil Mag.*, **3,** 119.
Thomson, J. J., and Thomson, G. P., 1933, *Conduction of Electricity Through Gases* (Cambridge: University Press).
Van Kampen, N., 1957, *Physica*, **23,** 641.

CORRESPONDENCE

Dislocations in Caesium Bromide

By S. Amelinckx
Laboratorium voor Kristalkunde, Rozier, 6, Gent, Belgium

[Received December 9, 1957]

Hitherto decoration methods have been applied successfully to the following ionic crystals : silver halides AgBr (Hedges and Mitchell 1953) and AgCl (Mitchell 1956), alkali halides of the sodium chloride type : NaCl, KCl and KBr (Amelinckx 1956 a, Amelinckx 1956 b, Barber *et al.* 1957, Maenhout-Van der Vorst and Dekeyser 1956, Amelinckx 1957) and calcium fluoride (Bontinck and Dekeyser 1956, Bontinck and Amelinckx 1957, Bontinck 1957, Van Keymeulen 1957). The configuration of Burgers vectors occurring in these crystals is characteristic for a face-centred cubic lattice : $\frac{1}{2}a[110]$ and, occasionally $a[100]$ (Amelinckx 1957). As one would expect on the basis of this similarity, no essential differences in dislocation pattern have been found between these substances.

It was therefore considered of interest to have a decoration technique for a crystal with a different lattice ; CsBr was chosen for this purpose. The Burgers vectors are here of the form $a[100]$, as in the primitive lattice. One of the problems which can be settled readily by direct observations is the question whether dislocations with a Burgers vector $a[110]$ are stable or not. The observation of an hexagonal network, or even of a threefold node would be a sufficient proof to establish the occurrence of the reaction

$$a[100]+a[010]\rightarrow a[110].$$

Dislocations have been decorated in CsBr using a procedure similar to the gold decoration technique used by Barber *et al.* (1957) for KBr and NaCl.

A first method consists in heating the crystal slice together with a small amount of gold bromide ($HAuBr_4$) in a vacuum sealed tube at some 600°C, during three or four hours. The heat treatment is followed by quenching. The crystal has then a deep blue colour as a consequence of the presence of colloidal gold, dispersed in the crystal, preferentially along dislocations. Observation is possible in transmission, but the contrast is poor. The decoration could be improved considerably by annealing the gold containing crystals in air during several hours at some 350°C. After this treatment the crystal is lightly pink. A final anneal of two hours at 550°C in hydrogen, followed by slow cooling makes

the crystal practically colourless, and produces a convenient decoration for ultramicroscopic illumination.

The role of the two anneals is to produce particles of a convenient size for observation.

To introduce the gold one can also deposit, by evaporation in vacuum, a thin gold layer onto the crystal and then anneal it in a sealed tube containing bromine. This last procedure was also followed using silver, instead of gold. In the latter case no quench is necessary to retain the metal in the crystal and a single anneal in hydrogen produces decoration.

Photographs 1 and 2 show some of the resulting patterns. In the particular crystals studied many of the boundaries had relatively large angles of misorientation and they could not be resolved into individual dislocations.

The photographs, however, show examples where this was possible. Photograph 1 shows the junction of three symmetrical pure tilt boundaries lying very approximately in cube planes, perpendicular to the Burgers vectors of the dislocations contained in them.

For such a junction a simple relation exists between the dislocation densities in the three boundaries: $\rho_1+\rho_2+\rho_3=0$. This relation, verified by means of etch pits on germanium by Pfann and Lovell (1955), is a special case of a more general relation verified previously also by means of etchpits (Amelinckx 1954, Dunn and Hibbard 1955). The relation is found to hold in this case also, confirming that we are revealing dislocations. On the same distance (5 cm on an enlarged photograph) one finds in the three boundaries respectively 15, 5 and 19 dislocations.

Photograph 2 shows a tilt boundary parallel to the plane of observation.

In a few rare cases apparently three fold nodes were observed, but we would not like to draw as yet, a definite conclusion concerning the stability of a[110] dislocations, until further evidence, e.g. the existence of hexagonal network is found.

In the course of these experiments a striking phenomenon in relation with the diffusion along dislocations was observed. If the crystals, containing quenched-in gold, are brought for a short time at some 550°c (some 10 minutes) it is found that the surface is covered with gold particles, but preferentially along the grain boundaries: this is, e.g. visible on photograph 3. The gold particles render visible the substructure of the crystal. By choosing proper conditions for this short high temperature treatment one can obtain the result shown in photograph 4, in which the fine substructure is made visible by small gold particles on the surface (ultra microscopic illumination). It is believed that every particle corresponds to the emergence point of a dislocation. This phenomenon is most probably due to gold diffusing out along the dislocation lines, and the nucleation of a small crystal at the emergence point.

A more detailed account will be published later.

Acknowledgments

I wish to thank Professor W. Dekeyser for his continuous interest and useful discussions.

This work is part of a research programme supported by I.R.S.I.A. (Institut pour les Recherches Scientifiques dans l'Industrie et l'Agriculture ; Comité d'Etude de l'Etat Solide).

References

Amelinckx, S., 1954, *Acta Met.*, **2**, 848 ; 1956 a, *Phil. Mag.*, **8**, 269 ; 1956 b, *Proceedings of the Lake Placid Conference on Dislocations* ; 1957, *Acta Met.* (in the press).
Barber, D. J., Harvey, K. B., and Mitchell, J. W., 1957, *Phil. Mag.*, **2**, 704.
Bontinck, W., 1957, *Phil. Mag.*, **2**, 561.
Bontinck, W., and Amelinckx, S., 1957, *Phil. Mag.*, **2**, 94.
Bontinck, W., and Dekeyser, W., 1956, *Physica*, **22**, 595.
Dunn, C. G., and Hibbard, W. R., 1955, *Acta Met.*, **3**, 409.
Hedges, J. M., and Mitchell, J. W., 1953, *Phil. Mag.*, **44**, 223.
Maenhout-Van der Vorst, and Dekeyser, W., 1956, *Phil. Mag.*, **1**, 882.
Mitchell, J. W., 1956, *Proceedings of the Lake Placid Conference on Dislocations*.
Pfann, W. G., and Lovell, L. C., 1955, *Acta Met.*, **3**, 512.
Van Keymeulen, J., 1957, *Naturwissenschaften*, **44**, 489.

The Temperature Dependence of Flow Stress in Copper Single Crystals

By M. J. Makin
Metallurgy Division, A.E.R.E., Harwell

[Received December 16, 1957]

Adams and Cottrell (1955) have measured the change in the flow stress of copper single crystals with temperature over a range of strains by experiments in which the specimen was repeatedly tested at one temperature, unloaded and retested at another temperature. The ratio of the flow stress immediately before unloading to that on retesting was recorded. To avoid the effect of work softening, which occurs on retesting at a higher temperature, measurements were made only on changing from high to low temperature, in this case −183°c, and the results were plotted after correction for the change in elastic constants with temperature as the 'reversible' change in flow stress with temperature (see figure). Recently, however, (Makin 1958), it has become apparent that a marked yield point occurs on retesting after unloading, the size of which is proportional to the amount of unloading ; furthermore the yield point is greatly increased when the second deformation is carried out below −150°c. These results make it clear that Adams and Cottrell did not

measure the true ' reversible ' change in flow stress but that their results also included the yield point produced by unloading, an ' irreversible ' phenomenon.

The experiment has, therefore, been repeated. Tensile tests on each specimen were carried out alternately at the testing temperature and −195°c. Measurements were made only on changing from high to low temperature, the procedure adopted by Adams and Cottrell, and the yield point effect was eliminated by extrapolating the stress–strain curve on retesting back to zero extension. This is possible since on retesting at the same temperature as the previous deformation the curve after the yield point returns to the extrapolated curve before unloading.

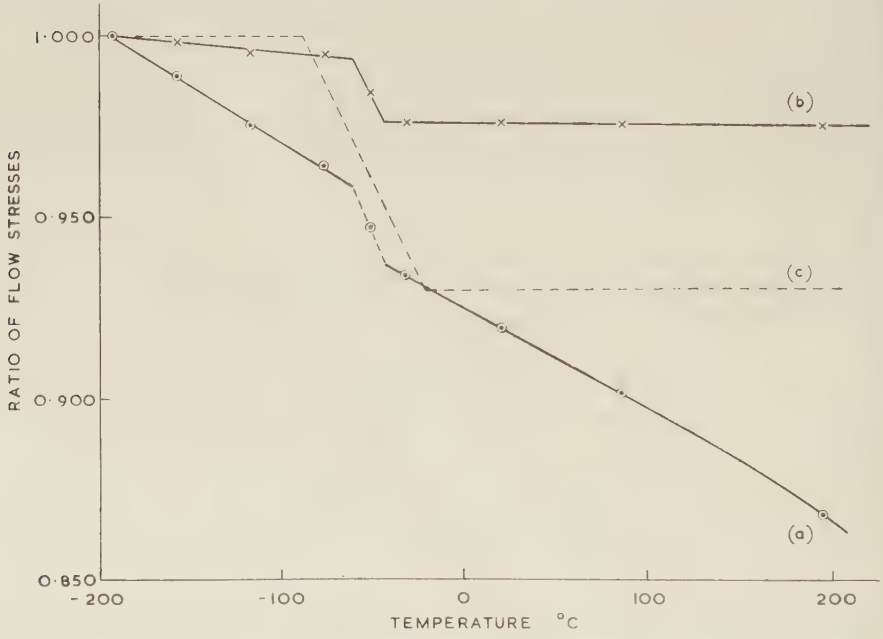

The reversible change in flow stress with temperature, (*a*) before correction for the change in elastic constants with temperature, and (*b*) after correction, compared with Adams and Cottrell's results, curve (*c*).

Copper single crystals of a standard crystal orientation ($\psi_0=\lambda_0=40°$) grown by the Bridgman method were used, and the various temperatures were obtained by immersing the specimen in liquid baths. The crystals were tested in a hard beam tensile machine at a strain rate of 6×10^{-5} per sec. Measurements were made between −195° and −159°, −115°, −78°, −51°, −30°, +84° and +196°c respectively. The results confirm the observation by Adams and Cottrell that the ratio of the flow stresses at two temperatures settles down after about 10% elongation to a constant value. Between ten and fifteen determinations of the ratio were made at each temperature,

The results are shown in the figure both before and after correction for the change in elastic constants with temperature (Köster 1948). The present work confirms the observation by Adams and Cottrell that the corrected flow stress is almost independent of the temperature except for a ' step ' in the curve. A very slight temperature dependence was observed between $-195°$ and $-57°$C and also above $-39°$C. To confirm that the step was a reversible change in flow stress with temperature and not due to another yield point or annealing effect cycling experiments were made between temperatures just above and just below the step. The reduction in the ratio of flow stresses which occurs at the step is, however, very much smaller in the present experiments than in Adams and Cottrell's, the decrease in ratio being 0·017 compared with 0·070.

References

Makin, M. J., 1958, *Phil Mag.*, **3**, 287.
Adams, M. A., and Cottrell, A. H., 1955, *Phil. Mag.*, **46**, 1187.
Köster, W., 1948, *Z. Metallk.*, **39**, 1.

REVIEWS OF BOOKS

Experimental Crystal Physics. By W. A. Wooster. (Clarendon Press: Oxford University Press.) [Pp. viii+115.] 18*s*.

New developments in solid-state physics have emphasized the importance of an understanding of the crystalline state and hence of laying a good foundation of crystal physics in undergraduate courses. Physics courses are, however, already overcrowded and can hardly be extended further, but this book provides what might be an acceptable solution—the provision of a number of experiments in crystal physics in second-year and third-year laboratory courses.

The book describes about two dozen experiments that have been fully tested in the author's laboratories. The subjects cover the main branches of physics—optical, electric, magnetic, thermal and elastic properties of crystals. The experiments seem well designed and enough practical details are given to enable them to be reasonably well reproduced with the ordinary facilities of a departmental workshop. Plastic deformation is also included; although the student may not learn a great deal from the results of the experiments described, at least he will learn to appreciate the limitations of the elementary laws of elasticity.

The book is strongly recommended to those who are in charge of physics laboratories; it may well have an influence quite out of proportion to its modest size. H. L.

[*The Editors do not hold themselves responsible for the views expressed by their correspondents.*]

Fig. 6

Typical slip lines observed during the early linear hardening region, $\epsilon=16\%$. $\Delta\epsilon=1{\cdot}1\%$ glide. ($\times 75$.)

Photograph 1

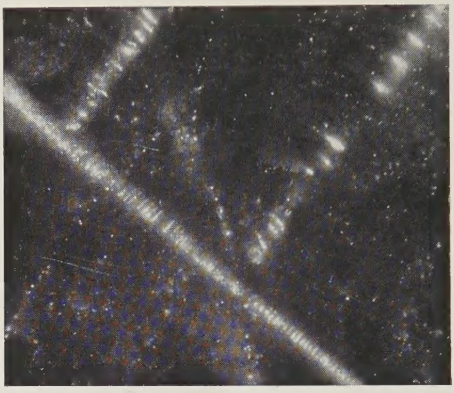

Junction of three tilt boundaries lying in cube plane in CsBr crystal. (×400.)

Photograph 2

Tilt boundary lying in the plane of observation. (×400.)

Photograph 3

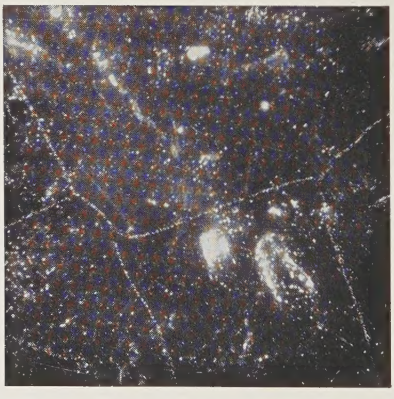

Intersection lines of grain boundaries with the surface of the crystal, as revealed by gold particles. (×100.)

Photograph 4

Emergence points of dislocations in subboundaries as revealed by gold particles. (×400.)